SHOCKS IN GRANULAR FLOWS– ANALYTICAL AND COMPUTATIONAL STUDIES

A Dissertation

Presented to the Faculty of the Graduate School

of Cornell University

in Partial Fulfillment of the Requirements for the Degree of

Doctor of Philosophy

by

Brian Patrick Lawney

January 2011

SHOCKS IN GRANULAR FLOWS– ANALYTICAL AND COMPUTATIONAL STUDIES

Brian Patrick Lawney, Ph.D.

Cornell University 2011

This dissertation concerns the analytical and numerical modeling of compressible shock in granular systems and its applications. Kinetic theory and classical thermodynamic arguments suggest that granular flows with low agitation (granular temperature) may be characterized as supersonic, experiencing almost discontinuous changes in flow properties across shock fronts created by obstructing bodies. Uniform and non-uniform flows are studied analytically and with discrete element numerical simulations in different geometries. We derive a set of algebraic relations to describe property changes local to the shock and expand the analysis with use of a system of coupled shock depth–averaged differential equations. These expressions are applied to uniform flow incident on straight wedge obstructions and comparison with simulations reveals good quantitative agreement. Finally we make use of discrete element simulations and apply kinetic theory analysis to shear flow about circular bodies to explain the production of propeller–shaped density features about embedded moons in the rings of Saturn. These density features are interpreted as being predominantly created by collisional processes, in contrast to prior studies where gravitation is incorporated. We adapt the general depth–averaged differential equations for application to this system and find reasonable qualitative predictions for the shock front.

BIOGRAPHICAL SKETCH

Brian Patrick Lawney was born March 24, 1983 in Port Jefferson, New York to Dennis and Patricia Lawney. Following graduation from Comsewogue High School, he enrolled at Clarkson University (Potsdam, NY) in August 2001. While pursuing a *B.S.* in mechanical engineering, Brian was a member of the Clarkson University Honors Program and conducted research concerning granular segregation of inclined flows under the direction of Professor Hayley H. Shen. He also was an active member and captain of the varsity cross–country running and nordic skiing teams. Brian joined the Department of Theoretical and Applied Mechanics at Cornell University in August 2005.

ACKNOWLEDGEMENTS

While in graduate school I have had the pleasure to work with many remarkable people, both in the academic setting and in other varied contexts. To say Cornell University and the Ithaca community have been integral to my development as a young adult would be a gross understatement. I feel fortunate for the knowledge and experience I gained during my time here. I would like to especially thank my advisor Jim Jenkins for his guidance during my time at Cornell. His patience and assistance were invaluable to my progress and the confirmation of my career ambitions. Prior to the eventual thesis work I was lacking in direction and motivation with several false starts – without Jim's concern and direction I would likely not have seen this work through to its completion. I would also like to thank the professors in the Department of Theoretical and Applied Mechanics with whom I worked for sharing their insight and experience related to teaching. Lastly I would like to thank my family and Molly Sorlien for their uncompromising love and support.

TABLE OF CONTENTS

LIST OF FIGURES

CHAPTER 1

INTRODUCTION

1.1 Granular Matter

Granular or particulate matter systems consist of collections of interacting discrete elements which often exhibit complex behavior on the bulk scale. They are encountered in a variety of contexts ranging from industrial processes concerning mixing and pouring to geophysical applications such as sediment transport and avalanching. Size segregation [35], dilatancy under shear [33], jamming [22], and peculiar signal propagation [23] represent a small subset of interesting phenomena displayed by granular media. Often the goal of studies is to describe the macro–scale behavior of these systems in terms of a few parameters such as material properties, boundary conditions, or other relevant characteristics without regard for the details of the multitude of particle interactions.

The constituent elements of such systems are typically massive enough that they are not subject to Brownian motion which places particle length scales on the order of 10^{-6}m and larger [6]. In this thesis we are interested in *dry* granular systems, but one may also consider multicomponent situations with the introduction of an interstitial fluid. In general one can define several length scales of importance. The micro–scale or contact scale is characterized by lengths on the order of surface imperfections or particle shape. This scale is naturally relevant to the description of contact interaction. Beyond this is the particle–size scale, perhaps variously defined in highly disperse particle size distributions. Further increasing in size, it is sometimes possible to define an intermediate (meso) scale related to the size of agglomerates or the length of particle chains when enduring contacts are prevalent. Such scales do not always exist– dilute, collisional gases may lack

the intermediate–sized structure necessary to sensibly define this scale. Finally the macro–scale is on the order of system size. These scalings are inherently relative and the absolute dimensions may in fact range over many orders of magnitude depending on the application. For example, in this thesis we consider density disturbances in Saturn's rings where particle scales are on the order of a meter and the macro–scale is many thousands of kilometers. One may contrast this with experimental systems where the largest scales may be less than a meter.

Particle interactions may be realized in a variety of different manners which may include (but are certainly not limited to) repulsive, frictional, cohesive, electrostatic, gravitational, and van der Waals forces. Beyond the actual nature of the interaction, the choice of contact model will vary according to the needs or choices of the study. In the simulations of our dry system we consider purely repulsive forces with no interaction potential when the particles are not in contact. Interactions are considered instantaneous, with only binary collisions. Limited examples of other contact force models may include linear elastic, non–linear elastic (such as a Hertz law), and visco–elastic, where particle overlap and relative speeds determine the elastic and viscous response, respectively. Kinematical descriptions also vary. In collisional dilute gases experiencing brief contact duration, one may choose to omit rotational degrees of freedom in the description of particle motion. Conversely, studies indicate [27] that the inclusion of particle rotations and tangential friction is necessary to capture the relevant physics of denser configurations where momentum transfer is accomplished primarily through enduring contacts.

Depending upon the applied boundary conditions, assemblies of solid particles may exhibit the properties of gases, liquids, or solids [3, 9, 16]. The dissipative nature of real granular materials necessitates an adequate input of energy to maintain a particular steady state configuration and the relative energy of fluctuations

(temperature) can be used as a measure to define a particular phase. Transitional flows, jamming, and phase changes are of great interest and have significant practical consequences such as in the liquefaction of soils/debris in geophysical contexts.

1.2 Granular Shocks– Overview

In this thesis we examine the near–discontinuous changes in flow properties associated with supersonic granular shock transitions. As noted in [12], "kinetic grain flow is intrinsically a supersonic phenomenon." When particulate matter encounters physical obstacles, the ability to accurately model this particular class of flow becomes important. External, inclined chute, and gravitationally–driven free surface flows are typical situations where shocks may develop. In particular, the formation of shocks has been shown to be advantageous in mitigating damage caused by avalanching geophysical materials (snow avalanches, debris flows) [10]. Deflecting barriers have the ability to generate shock fronts which may significantly slow the material. In addition, smaller scale circumstances exist where flow is made to turn abruptly or is streamed over an obstruction [10, 12].

Granular shocks have been studied in a variety of methods, often complementing investigations of sound propagation. These more general sound studies are typically concerned with dense configurations (e.g. crystal lattices) and the effects of polydispersity [23], geometry effects [29], and the role of contact laws [13, 23, 29] (e.g. normal force models, inclusion of tangential interaction, and rotations). In a quasi one–dimensional study of disturbance propagation in silos, [37] uses a method of characteristics approach to solve the partial differential equations governing a hypoplastic continuum. Discrete element models have also been used to examine one–dimensional geometries, primarily highlighting the non–linear response of the chain as contacts open and close with purely repulsive interactions [13].

In two–dimensional geometries, shock formation is studied around obstructing bodies, as mentioned above. In [25], gravity driven flow incident on a triangular body is studied by the solution of "Navier–Stokes like" equations, discrete element simulations, and experimentation. Modeling of side wall effects precludes reasonable agreement between experiments and theory, but good quantitative agreement is found between the continuum equations and simulations. It is noted that this study was conducted at a relatively low area fraction ($\nu = 0.018$). In a study of the force of a granular stream on a circular obstruction, [4] note the aggolmeration of particles and the abrupt change in flow properties without specific discussion of shock formation or supersonic flow.

As mentioned above, three–dimensional studies often concern the height of the free surface as a gravity driven granular flow encounters a boundary– sometimes denoted as a hyraulic jump. Straight wedge geometries are studied [10] as well as tetrahedrons [11], and cylinders [14]. These first two studies make use of flow depth–averaged differential equations and found appropriate scaling with the Froude number, similar to the Mach number for ideal gas dynamics. Shock detachment Froude number for oblique shocks is also addressed. Theoretical and experimental findings are in excellent agreement. It is noted that in the modeling equations a polytropic gas equation of state is employed– as density increases, it becomes necessary to incorporate real gas effects, which is our contribution for plane geometries.

CHAPTER 2

GRANULAR SHOCK

In this chapter we establish basic relations that will support analysis presented in later sections. We make use of equilibrium thermodynamic relations to obtain an estimate for the sound speed in a two–dimensional granular gas; this becomes important for our characterization of a flow as supersonic. We follow this with a local analysis of shock properties and evaluate our model with the use of discrete element simulations. We then address the limitations of the local analysis, providing motivation for the model derived in Chapter 3.

2.1 General discussion of shocks in compressible flow

In this work we are concerned with a granular gas that is defined to be supersonic. Simply stated, we are interested in flows where the disturbances in the flow travel faster than the speed of signal propagation (sound speed). Typically we encounter this situation when flow is incident on a physical body and its properties are altered as a result of the interaction. Signals of the disturbance (the presence of the body) are not transmitted upstream fast enough to allow incoming material to react– the upstream material is "unaware" of the obstruction. Based upon the relative speeds of the material and sound propagation, we observe a generally well–defined region denoting the spatial extent of the disturbance. This is the shock front of interest.

Figure 2.1 depicts a point disturbance with speed V moving in a material with sound speed $\mathfrak{a}$. Note that for case (a) where $V < \mathfrak{a}$ (subsonic), sound signals propagate faster than the point and disturbance information is transmitted prior to the arrival of the point source. Contrast this with the case where the point speed exceeds that of the sound speed in the material. There exists an envelope behind the disturbance where sound signals have been transmitted, and an area

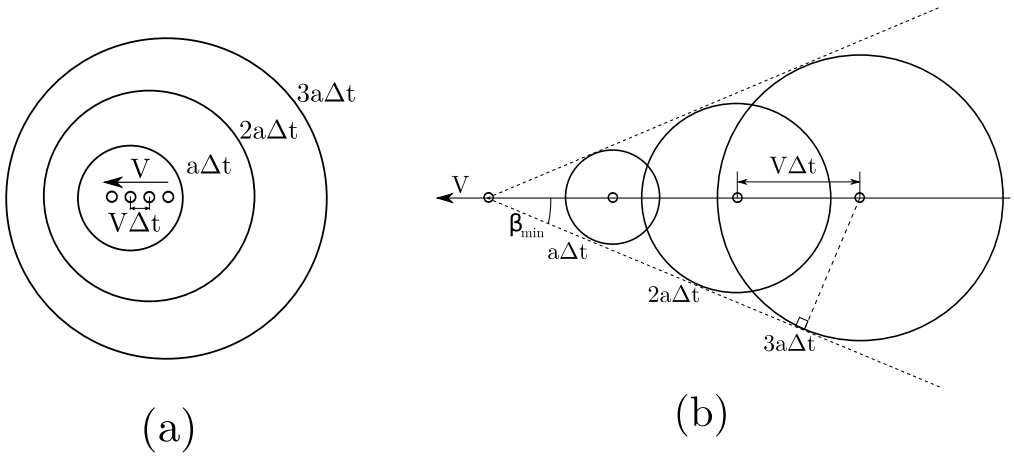

Figure 2.1: Schematic of a point disturbance in (a) subsonic and (b) supersonic flow. Snapshots are taken at regular time intervals Δt and the locus of the sound signal is represented by circles centered at the point of disturbance. A sequence of 3 time steps is depicted in each figure.

ahead where the medium is unaware of the approaching point. The shape of this envelope for more general disturbances is our interest in this work. In Figure 2.1(b) we examine the relative distances traversed by the point disturbance and the sound signal. In n time steps of Δt, the point disturbance has moved $V(n\Delta t)$ while the signal has reached points within a radius of $\mathfrak{a}(n\Delta t)$. The envelope of transmitted signals defining what is termed the Mach angle can be determined from an examination of the geometry of the figure, which will be addressed in Section 2.4.

2.2 Speed of Sound– thermodynamic relations

In this section we obtain an estimate for the sound speed of planar disks, making use of standard thermodynamic equilibrium arguments. We note that this is in-

deed an approximation– it is possible to achieve steady state provided appropriate balances of energy production and dissipation, but we do not obtain equilibrium in the classical sense.

By definition, the equilibrium speed of sound ($\mathfrak{a}$) in a material is,

$$\mathfrak{a}^2 = \left(\frac{\partial p}{\partial \rho}\right)_s = \frac{1}{\rho_m}\left(\frac{\partial p}{\partial \nu}\right)_s \tag{2.1}$$

where p is pressure and the density ρ may be expressed as a product of the area fraction ν and a constituent material density ρ_m. Note that the sound speed is defined with the specific entropy s held constant. Following the model of Anderson [1] we derive an expression for the granular gas.

In general, the first law of thermodynamics states,

$$dq = d\varepsilon + pdv \tag{2.2}$$

where q is the heat flux per unit mass, ε is energy per unit mass, p is pressure, and $\upsilon = 1/\rho$ is specific volume (density ρ). We also have the second law of thermodynamics,

$$dq = Tds \tag{2.3}$$

where T is the granular temperature, defined as the strength of the velocity fluctuations. See Section 2.5.1 for a formal definition. With (2.2) and (2.3) we have the differential thermodynamic relation,

$$Tds = d\varepsilon + pdv \tag{2.4}$$

We now change variables from υ since we wish to express the sound speed as a function of solid fraction $\nu = \rho/\rho_m$, where ρ_m is the density of the constituent

material. Thus, $d\upsilon = -(1/\rho_m \nu^2) d\nu$. Now we may write (2.4) as,

$$Tds = d\varepsilon - \frac{p}{\rho_m \nu^2} d\nu \tag{2.5}$$

Note that $\varepsilon = \varepsilon(s, \nu)$ in the above equation.

The expression for sound speed in (2.1) requires a statement of the pressure change in an isentropic process. By employing a partial Legendre transform, we are able to phrase (2.5) in terms of the change dp. First note,

$$\begin{aligned} d\left(\frac{p}{\rho_m \nu}\right) &= \frac{1}{\rho_m \nu} dp + \frac{p}{\rho_m}\left(\frac{-1}{\nu^2}\right) d\nu \\ \frac{p}{\rho_m \nu^2} d\nu &= -d\left(\frac{p}{\rho_m \nu}\right) + \frac{1}{\rho_m \nu} dp \end{aligned} \tag{2.6}$$

When substituted into (2.5),

$$\begin{aligned} Tds &= d\varepsilon - \left[-d\left(\frac{p}{\rho_m \nu}\right) + \frac{1}{\rho_m \nu} dp\right] \\ Tds &= d\left(\varepsilon + \frac{p}{\rho_m \nu}\right) - \frac{1}{\rho_m \nu} dp \end{aligned} \tag{2.7}$$

Thus we define our enthalpy as

$$\hbar \equiv \varepsilon + \frac{p}{\rho_m \nu} \tag{2.8}$$

and the transformed version of (2.5) is,

$$Tds = d\hbar - \frac{1}{\rho_m \nu} dp \tag{2.9}$$

and $\hbar = \hbar(s, p)$. Note that our definition of enthalpy is equivalent to the conventional $\hbar = \varepsilon + p\upsilon$ [24].

We now solve our first law relations (2.5) and (2.9) for ds,

$$ds = \frac{1}{T} d\varepsilon - \frac{p}{\rho_m T \nu^2} d\nu \tag{2.10}$$

$$ds = \frac{1}{T} d\hbar - \frac{1}{\rho_m T \nu} dp \tag{2.11}$$

We may substitute for the pressure in the top expression, employing the granular equation of state for elastic disks [19],

$$p = \rho_m \nu [1 + 2G(\nu)] T \tag{2.12}$$

where $G(\nu) \equiv \nu g_0(\nu)$ and the radial distribution function for identical disks in contact is [36],

$$g_0(\nu) = \frac{16 - 7\nu}{16(1-\nu)^2} \tag{2.13}$$

In the case of a perfect gas model, the bracketed term in (2.12) is constant. Written in terms of ν, the granular equation of state is,

$$p = \rho_m \nu \left[\frac{8 + \nu^2}{8(1-\nu)^2} \right] T \tag{2.14}$$

which gives us,

$$ds = \frac{1}{T} d\varepsilon - \frac{1 + 2G}{\nu} d\nu \tag{2.15}$$

As above, we consider $\varepsilon = \varepsilon(s, \nu)$. If $s = s(\nu, T)$, we specify the internal energy to be a function of (ν, T). Taking the total differential of ε,

$$d\varepsilon = \left(\frac{\partial \varepsilon}{\partial T} \right)_\nu dT + \left(\frac{\partial \varepsilon}{\partial \nu} \right)_T d\nu \tag{2.16}$$

we apply to (2.15) which yields,

$$ds = \frac{1}{T} \left[\left(\frac{\partial \varepsilon}{\partial T} \right)_\nu dT + \left(\frac{\partial \varepsilon}{\partial \nu} \right)_T d\nu \right] - \frac{1 + 2G}{\nu} d\nu$$

$$ds = \frac{1}{T} \left(\frac{\partial \varepsilon}{\partial T} \right)_\nu dT + \left[\left(\frac{\partial \varepsilon}{\partial \nu} \right)_T - \frac{1 + 2G}{\nu} \right] d\nu \tag{2.17}$$

Now consider (2.11), which states that $s = s(h, p)$. If we choose the enthalpy to be a function of pressure and temperature, we have $s = s(h(p, T), p) = s(p, T)$.

However, we have already specified that $s = s(\nu, T)$, so it is necessary to write the equation of state as $\nu = \nu(p, T)$. We write the total differential of h,

$$dh = \left(\frac{\partial h}{\partial T}\right)_p dT + \left(\frac{\partial h}{\partial p}\right)_T dp \tag{2.18}$$

which we apply to (2.11),

$$ds = \frac{1}{T}\left[\left(\frac{\partial h}{\partial T}\right)_p dT + \left(\frac{\partial h}{\partial p}\right)_T dp\right] - \frac{1}{T\rho_m\nu}dp$$

$$ds = \frac{1}{T}\left(\frac{\partial h}{\partial T}\right)_p dT + \left[\frac{1}{T}\left(\frac{\partial h}{\partial p}\right)_T - \frac{1}{T\rho_m\nu}\right]dp \tag{2.19}$$

At this point we enforce the isentropic condition, $ds = 0$ and write,

$$0 = \left(\frac{\partial \varepsilon}{\partial T}\right)_\nu dT + \left[\left(\frac{\partial \varepsilon}{\partial \nu}\right)_T - \frac{T(1+2G)}{\nu}\right]d\nu \tag{2.20}$$

$$0 = \left(\frac{\partial h}{\partial T}\right)_p dT + \left[\left(\frac{\partial h}{\partial p}\right)_T - \frac{1}{\rho_m\nu}\right]dp \tag{2.21}$$

Solve for $d\nu$ and dp respectively,

$$d\nu = \frac{\nu\left(\frac{\partial \varepsilon}{\partial T}\right)_\nu dT}{T(1+2G) - \nu\left(\frac{\partial \varepsilon}{\partial \nu}\right)_T} \tag{2.22}$$

$$dp = \frac{\rho_m\nu\left(\frac{\partial h}{\partial T}\right)_p dT}{1 - \rho_m\nu\left(\frac{\partial h}{\partial p}\right)_T} \tag{2.23}$$

Divide (2.23) by (2.22) to form the desired quantity,

$$\left(\frac{dp}{d\nu}\right)_s = \frac{\rho_m\left(\frac{\partial h}{\partial T}\right)_p\left[T(1+2G) - \nu\left(\frac{\partial \varepsilon}{\partial \nu}\right)_T\right]}{\left(\frac{\partial \varepsilon}{\partial T}\right)_\nu\left[1 - \rho_m\nu\left(\frac{\partial h}{\partial p}\right)_T\right]} \tag{2.24}$$

Replacing the partial derivatives of enthalpy in favor of ν we have,

$$\left(\frac{dp}{d\nu}\right)_s = \frac{\rho_m\nu^2 - p\left(\frac{\partial \nu}{\partial T}\right)_p}{\rho_m\nu^2\left(\frac{\partial \nu}{\partial p}\right)_T} \tag{2.25}$$

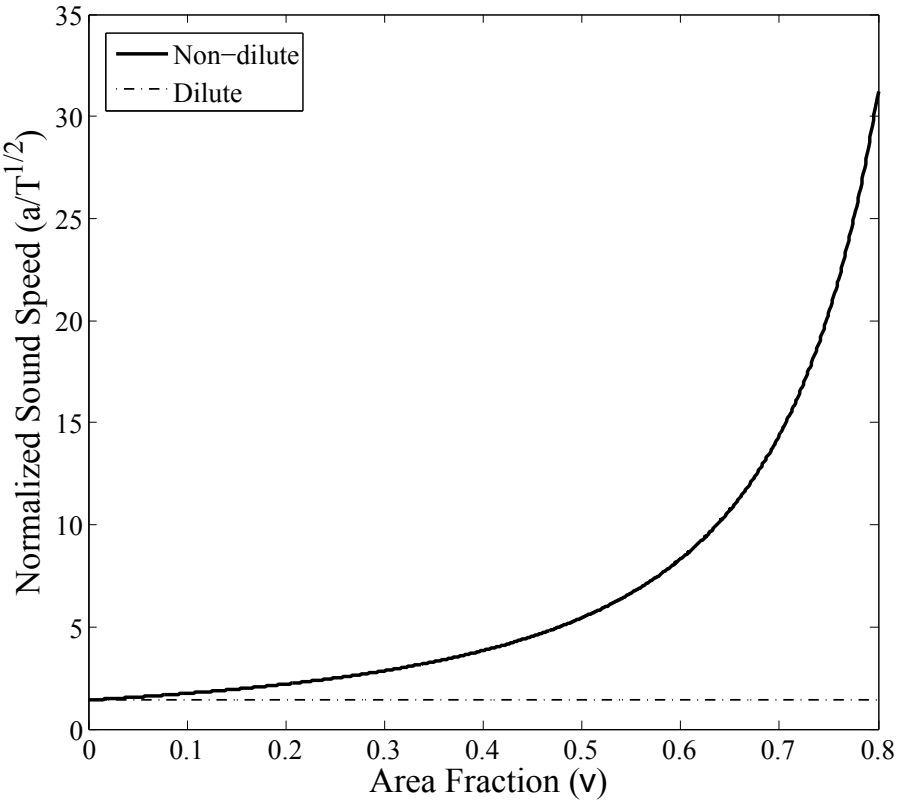

Figure 2.2: Temperature–normalized sound speed (2.27), plotted against area fraction (solid line). Dilute limit (2.30) plotted with dotted line.

where we explicitly denote an isentropic process. For a discrete system of disks in two–dimensions, the internal energy per unit volume is exactly the temperature ($\varepsilon = T$) [17]. Evaluating the appropriate partial derivatives we are left with

$$\left(\frac{dp}{d\nu}\right)_s = \frac{\rho_m T(9\nu^4 - 32\nu^3 - 24\nu^2 + 128)}{64(1-\nu)^4} \tag{2.26}$$

and the temperature–normalized sound speed is,

$$\frac{\mathfrak{a}^2}{T} = \frac{9\nu^4 - 32\nu^3 - 24\nu^2 + 128}{64(1-\nu)^4} \tag{2.27}$$

This is plotted in Figure 2.2 for area fraction $0 \leq \nu \leq 0.8$. We note that [26] presents a derivation for the sound speed in a three–dimensional granular gas in a similar manner.

2.2.1 Dilute Limit

In the dilute limit of $\nu \ll 1$, the density function $1 + 2G(\nu) \approx 1$, and the equation of state reduces to

$$p = \rho_m \nu T \tag{2.28}$$

As a result, $\hbar = 2T$ and,

$$\left(\frac{dp}{d\nu}\right)_s = 2\rho_m T \tag{2.29}$$

so the sound speed in the dilute limit ($\mathfrak{a}_d$) is,

$$\mathfrak{a}_d = \sqrt{2T} \tag{2.30}$$

where we see that the sound speed is independent of density, and the temperature–normalized sound speed is simply $\mathfrak{a}_d^2/T = 2$. Note that the sound speed for a perfect gas ($p = \rho \mathfrak{R} T$) is $\mathfrak{a}_{pg} = \sqrt{\gamma_g \mathfrak{R} T}$ where $\gamma_g = c_p/c_v$ is the ratio of specific heats (a constant for a perfect gas) and $\mathfrak{R}$ the ideal gas constant.

2.3 Oblique Shock

In this section we establish basic transport relations and apply them to local balances of mass, momentum, and energy flux. We then integrate the resulting expressions over an idealized shock discontinuity, which results in a system of four algebraic equations in four unknowns. For completeness we present the full derivation of these jump conditions, but note that their forms do not differ from those shown in [1, 5]. Our analysis differs by the inclusion of real gas effects. We examine the nature of solutions of this system at both intermediate and dilute packing fractions.

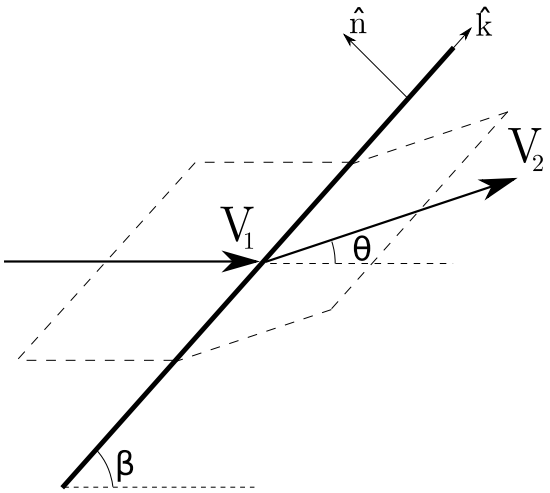

Figure 2.3: Plane oblique shock geometry

Here we consider a two-dimensional oblique shock at inclination β with respect to the incoming flow of speed V_1 with accompanying area fraction ν_1 and temperature T_1. In general, we permit a change in the flow velocity through the shock, as shown in Figure 2.3. Flow passing through the shock surface is turned by an angle θ and experiences changes in its other properties as well. This change in flow direction is often caused by the presence of an obstructing body in the flow, but the shock conditions and geometry may be analyzed without consideration for such a body.

The shock surface is idealized as a discontinuity line – changes in flow properties occur over a negligible distance, on the order of a mean free path for a molecular gas [5]. We choose a locally oriented orthogonal coordinate system (unit vectors $(\hat{\mathbf{n}}, \hat{\mathbf{k}})$ in Figure 2.3) at the point of interest and consider one–dimensional flow in the direction normal to the shock. We seek to derive jump relations for post–shock (also referred to as downstream) flow conditions in terms of the known upstream quantities. Before proceeding with the derivation for the jump conditions across

the shock, we state the Reynold's Transport Theorem,

$$\frac{d}{dt}\int\limits_{\mathbb{V}(t)} F(\mathbf{x},t)\ dV = \int\limits_{\mathbb{V}(t)} \frac{\partial F}{\partial t}\ dV + \int\limits_{\mathbb{A}(t)} F\mathbf{u}_{\mathbb{A}}\cdot\mathbf{dA} \tag{2.31}$$

where $F(\mathbf{x},t)$ is a tensor quantity of any order, $\mathbb{V}(t)$ is the volume of interest, and $\mathbb{A}(t)$ is the bounding surface of $\mathbb{V}(t)$. The velocity $\mathbf{u}_A$ is taken to be the velocity of the bounding surface. This relation applies to both fixed (Eulerian) and material (Lagrangian) volumes. In the derivation of the jump conditions we consider a material volume containing the discontinuous shock. Thus, $\mathbf{u}_{\mathbb{A}}$ of (2.31) is the fluid velocity $\mathbf{u}$ and we have,

$$\frac{D}{Dt}\int\limits_{\mathbb{V}(t)} F(\mathbf{x},t)\ dV = \int\limits_{\mathbb{V}(t)} \frac{\partial F}{\partial t}\ dV + \int\limits_{\mathbb{A}(t)} F\mathbf{u}\cdot\mathbf{dA} \tag{2.32}$$

The notation for the material derivative (D/Dt) is used to explicitly denote that we are in consideration of a material volume. Using the Divergence Theorem to express the surface integral of (2.32) as a volume integration,

$$\frac{D}{Dt}\int\limits_{\mathbb{V}(t)} F(\mathbf{x},t)\ dV = \int\limits_{\mathbb{V}(t)} \left[\frac{\partial F}{\partial t} + \frac{\partial}{\partial x_\alpha}(Fu_\alpha)\right]\ dV \tag{2.33}$$

Greek subscripts denote vector components with respect to a set of orthogonal coordinate axes, and we adopt the convention of summation over repeated indices.

We now consider a generic quantity of interest $f(\mathbf{x},t)$ such that $F(\mathbf{x},t) = \rho(\mathbf{x},t)f(\mathbf{x},t)$. Our transport equation becomes,

$$\frac{D}{Dt}\int\limits_{\mathbb{V}(t)} \rho f\ dV = \int\limits_{\mathbb{V}(t)} \left[\frac{\partial(\rho f)}{\partial t} + \frac{\partial}{\partial x_\alpha}(\rho f u_\alpha)\right]\ dV$$

$$\frac{D}{Dt}\int\limits_{\mathbb{V}(t)} \rho f\ dV = \int\limits_{\mathbb{V}(t)} \left[f\frac{\partial\rho}{\partial t} + \rho\frac{\partial f}{\partial t} + f\frac{\partial}{\partial x_\alpha}(\rho u_\alpha) + \rho u_\alpha\frac{\partial f}{\partial x_\alpha}\right]\ dV$$

$$\frac{D}{Dt}\int\limits_{\mathbb{V}(t)} \rho f\ dV = \int\limits_{\mathbb{V}(t)} \left[f\left(\frac{\partial\rho}{\partial t} + \frac{\partial}{\partial x_\alpha}(\rho u_\alpha)\right) + \rho\left(\frac{\partial f}{\partial t} + \rho u_\alpha\frac{\partial f}{\partial x_\alpha}\right)\right]\ dV \tag{2.34}$$

where we recognize the mass continuity equation,

$$\frac{\partial \rho}{\partial t} + \frac{\partial}{\partial x_\alpha}(\rho u_\alpha) = 0 \tag{2.35}$$

and subsequently (2.34) reduces to leave us with,

$$\frac{D}{Dt} \int\limits_{\mathbb{V}(t)} \rho f \; dV = \int\limits_{\mathbb{V}(t)} \left[\rho \left(\frac{\partial f}{\partial t} + \rho u_\alpha \frac{\partial f}{\partial x_\alpha} \right) \right] \; dV \tag{2.36}$$

which we may shorten with use of the definition of the convective or material derivative ($D/Dt \equiv \partial/\partial t + u_\alpha(\partial/\partial x_\alpha)$),

$$\frac{D}{Dt} \int\limits_{\mathbb{V}(t)} \rho f \; dV = \int\limits_{\mathbb{V}(t)} \rho \frac{Df}{Dt} \; dV \tag{2.37}$$

Thus, in taking the time derivative of a material volume integration, we may bring the material derivative inside the integral sign in accordance with (2.37). This will be useful in the manipulation of the transport equations contained in the following sections.

2.3.1 Mass Conservation

For $f = 1$, we have $F = \rho$ and (2.37) is,

$$\frac{D}{Dt} \int\limits_{\mathbb{V}(t)} \rho \; dV = 0 \tag{2.38}$$

We are in consideration of one–dimensional flow normal to the shock line depicted in Figure 2.3, so the integral reduces to a line integral in the $\hat{\mathbf{n}}$ direction. We take the limits of integration $a_1(t)$ and $a_2(t)$ to be functions of time,

$$\frac{D}{Dt} \int\limits_{a_1(t)}^{a_2(t)} \rho \; dn = 0 \tag{2.39}$$

We take the shock location to be at $n = \zeta(t)$,

$$\frac{D}{Dt}\int_{a_1(t)}^{\zeta^-(t)} \rho \; dn + \frac{D}{Dt}\int_{\zeta^+(t)}^{a_2(t)} \rho \; dn = 0 \tag{2.40}$$

where the $+/-$ signs denote post and pre–shock, respectively. We now use the Leibniz integral rule in one–dimension,

$$\frac{\partial}{\partial z}\int_{a(z)}^{b(z)} g(x,z) \; dx = \int_{a(z)}^{b(z)} \frac{\partial g}{\partial z} \; dx + g(b(z),z)\frac{db}{dz} - g(a(z),z)\frac{da}{dz} \tag{2.41}$$

Which we apply to (2.40),

$$\frac{D}{Dt}\int_{a_1(t)}^{a_2(t)} \rho \; dn = \int_{a_1(t)}^{\zeta^-(t)} \frac{\partial \rho}{\partial t} \; dn + \rho(\zeta^-(t),t)\frac{d\zeta^-}{dt} - \rho(a_1(t),t)\frac{da_1}{dt} +$$
$$+ \int_{\zeta^+(t)}^{a_2(t)} \frac{\partial \rho}{\partial t} \; dn + \rho(a_2(t),t)\frac{da_2}{dt} - \rho(\zeta^+(t),t)\frac{d\zeta^+}{dt} = 0$$

Combining the integrals on the right hand side,

$$\frac{D}{Dt}\int_{a_1(t)}^{a_2(t)} \rho dn = \int_{a_1(t)}^{a_2(t)} \frac{\partial \rho}{\partial t} \; dn + \rho(\zeta^-(t),t)\frac{d\zeta^-}{dt} - \rho(a_1(t),t)\frac{da_1}{dt} +$$
$$+\rho(a_2(t),t)\frac{da_2}{dt} - \rho(\zeta^+(t),t)\frac{d\zeta^+}{dt} = 0 \tag{2.42}$$

We denote the shock velocity as,

$$U \equiv \frac{d\zeta^+}{dt} = \frac{d\zeta^-}{dt} \tag{2.43}$$

If we take $a_1(t) = \zeta - \Delta$, $a_2(t) = \zeta + \Delta$, and take the limit as $\Delta \to 0$, the integral on the right hand side of (2.42) tends to zero. Additionally, in the limit of $\Delta \to 0$, $\rho(\zeta^-(t),t) = \rho(a_1(t),t) = \rho_1$ and $\rho(\zeta^+(t),t) = \rho(a_2(t),t) = \rho_2$. Since we are in consideration of a material volume, the time derivatives of the limits a_1 and a_2 are simply the flowfield velocities on either side of the shock,

$$\frac{da_1}{dt} = u_1$$

$$\frac{da_2}{dt} = u_2$$

which leaves us with,

$$\frac{D}{Dt}\int_{a_1(t)}^{a_2(t)} \rho \, dn = \rho_1(U - u_1) + \rho_2(u_2 - U) = 0$$

We note that this relationship is dependent on the relative velocity of the flow with respect to the shock. In particular we are interested in the stationary shock ($U = 0$), so our mass conservation jump condition becomes,

$$\rho_1 u_1 = \rho_2 u_2 \tag{2.44}$$

2.3.2 Normal Momentum

Here we consider the balance of momentum normal to the shock. We start with a statement of the balance of linear momentum,

$$\frac{D}{Dt}(mu_\alpha) = \mathfrak{F}_\alpha \tag{2.45}$$

where m denotes mass and $\mathfrak{F}$ the resultant applied force on the material of interest. Note that we may write,

$$m = \int_{\mathbb{V}(t)} \rho \, dV \tag{2.46}$$

so (2.45) may be written as,

$$\frac{D}{Dt}\left[u_\alpha \int_{\mathbb{V}(t)} \rho \, dV\right] = \mathfrak{F}_\alpha$$

$$\frac{Du_\alpha}{Dt}\int_{\mathbb{V}(t)} \rho \, dV + u_\alpha \frac{D}{Dt}\int_{\mathbb{V}(t)} \rho \, dV = \mathfrak{F}_\alpha \tag{2.47}$$

The conservation of mass states,

$$\frac{D}{Dt}\int\limits_{\mathbb{V}(t)} \rho \; dV = 0 \tag{2.48}$$

and our linear momentum balance is,

$$\frac{Du_\alpha}{Dt}\int\limits_{\mathbb{V}(t)} \rho \; dV = \mathfrak{F}_\alpha$$

$$m\frac{Du_\alpha}{Dt} = \mathfrak{F}_\alpha$$

$$\rho\frac{Du_\alpha}{Dt} = \mathfrak{f}_\alpha \tag{2.49}$$

where $\mathfrak{f}$ is the force per unit volume. Integrating over the volume,

$$\int\limits_{\mathbb{V}(t)} \rho\frac{Du_\alpha}{Dt} \; dV = \int\limits_{\mathbb{V}(t)} \mathfrak{f}_\alpha \; dV = \mathfrak{F}_\alpha \tag{2.50}$$

By (2.37),

$$\frac{D}{Dt}\int\limits_{\mathbb{V}(t)} \rho u_\alpha \; dV = \mathfrak{F}_\alpha \tag{2.51}$$

The total force on the material volume ($\mathfrak{F}$) can be expressed as the sum of a body force per unit mass $\mathbf{b}$ and surface tractions τ,

$$\frac{D}{Dt}\int\limits_{\mathbb{V}(t)} \rho u_\alpha \; dV = \int\limits_{\mathbb{V}(t)} \rho b_\alpha \; dV + \int\limits_{\mathbb{A}(t)} \tau_{\alpha\beta} \; dA_\beta \tag{2.52}$$

In this analysis we ignore the body force term and assume inviscid flow so the traction tensor is $\tau_{\alpha\beta} = -p\delta_{\alpha\beta}$ where $\delta_{\alpha\beta}$ is the identity tensor. We also make use of the Divergence Theorem to write,

$$\frac{D}{Dt}\int\limits_{\mathbb{V}(t)} \rho u_\alpha \; dV = -\int\limits_{\mathbb{A}(t)} p\delta_{\alpha\beta} \; dA_\beta$$

$$\frac{D}{Dt}\int\limits_{\mathbb{V}(t)} \rho u_\alpha \; dV = -\int\limits_{\mathbb{V}(t)} \frac{\partial(p\delta_{\alpha\beta})}{\partial x_\beta} \; dV$$

$$\frac{D}{Dt}\int\limits_{\mathbb{V}(t)} \rho u_\alpha \; dV = -\int\limits_{\mathbb{V}(t)} \frac{\partial p}{\partial x_\alpha} \; dV \tag{2.53}$$

As before, we consider flow in the direction normal to the shock, integrating over the discontinuity,

$$\frac{D}{Dt}\int\limits_{a_1(t)}^{a_2(t)} \rho u \; dn = -\int\limits_{a_1(t)}^{a_2(t)} \frac{\partial p}{\partial n} \; dn$$

$$\frac{D}{Dt}\int\limits_{a_1(t)}^{a_2(t)} \rho u \; dn = -\left[p(a_2(t),t) - p(a_1(t),t)\right]$$

$$\frac{D}{Dt}\int\limits_{a_1(t)}^{a_2(t)} \rho u \; dn = p_1 - p_2$$

As in expression (2.42), the left hand side may be written as,

$$\frac{D}{Dt}\int\limits_{a_1(t)}^{a_2(t)} \rho u \; dn = \int\limits_{a_1(t)}^{a_2(t)} \frac{\partial(\rho u)}{\partial t} \; dn + (\rho u)\Big|_{(\zeta^-(t),t)} \frac{d\zeta^-}{dt} -$$

$$-(\rho u)\Big|_{(a_1(t),t)} \frac{da_1}{dt} + (\rho u)\Big|_{(a_2(t),t)} \frac{da_2}{dt} - (\rho u)\Big|_{(\zeta^+(t),t)} \frac{d\zeta^+}{dt} = p_1 - p_2 \tag{2.54}$$

As we take the limit of the integrating volume approaching the shock, we have

$$\frac{D}{Dt}\int\limits_{a_1(t)}^{a_2(t)} \rho u \; dn = +\rho_1 u_1 U - \rho_1 u_1^2 + \rho_2 u_2^2 - \rho_2 u_2 U = p_1 - p_2 \tag{2.55}$$

Once again, we consider a stationary shock (or equivalently treat u_1 or u_2 as the flow velocity relative to the shock), and we have our normal momentum jump condition,

$$p_1 + \rho_1 u_1^2 = p_2 + \rho_2 u_2^2 \tag{2.56}$$

2.3.3 Tangential Momentum

Consider the material volume spanning the shock discontinuity. If the material volume is to remain continuous, the tangential velocity must be the same on both sides of the shock. Denoting this tangential velocity as w,

$$w_1 = w_2 \tag{2.57}$$

Alternatively, one can obtain this relation by balancing the momentum flux through the dotted surface depicted in Figure 2.3,

$$\int_{\mathbb{A}(t)} \rho w \mathbf{V} \cdot \mathbf{dA} = 0 \tag{2.58}$$

Based on the choice of surface, there is no momentum flux through the top and bottom faces on either side of the shock. Thus,

$$-\rho_1 w_1 u_1 A_1 + \rho_2 w_2 u_2 A_2 = 0 \tag{2.59}$$

where again, u_1 and u_2 are the speeds normal to the shock. Note that the areas are equal, $A_1 = A_2$, and use of the continuity jump condition (2.44) yields (2.57).

2.3.4 Energy

We start with a general expression for the balance of energy,

$$\begin{aligned}\frac{D}{Dt}\int_{\mathbb{V}(t)} \rho\left(\frac{1}{2}u_\alpha u_\alpha + \varepsilon\right)\, dV = &\int_{\mathbb{V}(t)} \rho(b_\alpha u_\alpha + c_1)\, dV + \\ &+ \int_{\mathbb{A}(t)} (\tau_{\alpha\beta} u_\alpha - q_\beta + c_2)\, dA_\beta\end{aligned} \tag{2.60}$$

where again, $\mathbf{b}$ is the body force per unit mass, τ is the traction, and ε the internal energy per unit mass. The vector $\mathbf{q}$ is the heat flux, and c_1 and c_2 represent other possible sources of energy. For our analysis, we consider an adiabatic process where

$\mathbf{q} = 0$ and only preserve terms related to production by the stress–work. Thus we have,

$$\frac{D}{Dt}\int\limits_{\mathbb{V}(t)} \rho\left(\frac{1}{2}u_\alpha u_\alpha + \varepsilon\right)\, dV = \int\limits_{\mathbb{A}(t)} \tau_{\alpha\beta}u_\alpha\, dA_\beta \tag{2.61}$$

where we use the Divergence Theorem to write,

$$\frac{D}{Dt}\int\limits_{\mathbb{V}(t)} \rho\left(\frac{1}{2}u_\alpha u_\alpha + \varepsilon\right)\, dV = \int\limits_{\mathbb{V}(t)} \frac{\partial(\tau_{\alpha\beta}u_\alpha)}{\partial x_\beta}\, dV \tag{2.62}$$

For our inviscid analysis, $\tau_{\alpha\beta} = -p\delta_{\alpha\beta}$,

$$\frac{D}{Dt}\int\limits_{\mathbb{V}(t)} \rho\left(\frac{1}{2}u_\alpha u_\alpha + \varepsilon\right)\, dV = -\int\limits_{\mathbb{V}(t)} \frac{\partial(p\delta_{\alpha\beta}u_\alpha)}{\partial x_\beta}\, dV$$

$$\frac{D}{Dt}\int\limits_{\mathbb{V}(t)} \rho\left(\frac{1}{2}u_\alpha u_\alpha + \varepsilon\right)\, dV = -\int\limits_{\mathbb{V}(t)} \frac{\partial(pu_\alpha)}{\partial x_\alpha}\, dV \tag{2.63}$$

Terms may be eliminated by use of the equation for the normal momentum flux. First note, by use of (2.37),

$$\begin{aligned}\frac{D}{Dt}\int\limits_{\mathbb{V}(t)} \rho\left(\frac{1}{2}u_\alpha u_\alpha + \varepsilon\right)\, dV &= \int\limits_{\mathbb{V}(t)} \rho\frac{D}{Dt}\left(\frac{1}{2}u_\alpha u_\alpha + \varepsilon\right)\, dV \\ &= \int\limits_{\mathbb{V}(t)} \rho\left(u_\alpha\frac{Du_\alpha}{Dt} + \frac{D\varepsilon}{Dt}\right)\, dV \end{aligned}\tag{2.64}$$

We now rewrite (2.63), expanding the right hand side,

$$\int\limits_{\mathbb{V}(t)} \rho\left(u_\alpha\frac{Du_\alpha}{Dt} + \frac{D\varepsilon}{Dt}\right)\, dV = -\int\limits_{\mathbb{V}(t)} \left(u_\alpha\frac{\partial p}{\partial x_\alpha} + p\frac{\partial u_\alpha}{\partial x_\alpha}\right)\, dV \tag{2.65}$$

Write out each term explicitly,

$$\begin{aligned}&\int\limits_{\mathbb{V}(t)} \rho\left(u\frac{Du}{Dt} + w\frac{Dw}{Dt} + \frac{D\varepsilon}{Dt}\right)\, dV = \\ &-\int\limits_{\mathbb{V}(t)} \left(u\frac{\partial p}{\partial n} + w\frac{\partial p}{\partial k} + p\frac{\partial u}{\partial n} + p\frac{\partial w}{\partial k}\right)\, dV\end{aligned}$$

Combine,

$$\int_{\mathbb{V}(t)} \left(\rho u \frac{Du}{Dt} + \rho w \frac{Dw}{Dt} + \rho \frac{D\varepsilon}{Dt} + u \frac{\partial p}{\partial n} + w \frac{\partial p}{\partial k} + p \frac{\partial u}{\partial n} + p \frac{\partial w}{\partial k} \right) dV = 0 \tag{2.66}$$

Note (2.53) may be written as,

$$\int_{\mathbb{V}(t)} \rho \frac{Du_\alpha}{Dt} dV = - \int_{\mathbb{V}(t)} \frac{\partial p}{\partial x_\alpha} \, dV$$

$$\int_{\mathbb{V}(t)} \left(\rho \frac{Dw}{Dt} + \frac{\partial p}{\partial k} \right) \, dV = 0 \tag{2.67}$$

which cancels terms in (2.66), leaving

$$\int_{\mathbb{V}(t)} \left(\rho u \frac{Du}{Dt} + \rho \frac{D\varepsilon}{Dt} + u \frac{\partial p}{\partial n} + p \frac{\partial u}{\partial n} + p \frac{\partial w}{\partial k} \right) \, dV = 0 \tag{2.68}$$

By the preservation of tangential flow velocity w, the final term also vanishes, so our simplified energy balance becomes,

$$\int_{\mathbb{V}(t)} \left(\rho u \frac{Du}{Dt} + \rho \frac{D\varepsilon}{Dt} + u \frac{\partial p}{\partial n} + p \frac{\partial u}{\partial n} \right) \, dV = 0 \tag{2.69}$$

Again we integrate this over the direction normal to the shock,

$$\int_{a_1(t)}^{a_2(t)} \left(\rho u \frac{Du}{Dt} + \rho \frac{D\varepsilon}{Dt} + u \frac{\partial p}{\partial n} + p \frac{\partial u}{\partial n} \right) \, dn = 0$$

Rewrite the first two terms using the convective derivative and employ (2.37),

$$\frac{D}{Dt} \int_{a_1(t)}^{a_2(t)} \rho \left(\frac{1}{2} u^2 + \varepsilon \right) \, dn + (pu) \Big|_{(a_2(t),t)} - (pu) \Big|_{(a_1(t),t)} = 0$$

$$\frac{D}{Dt} \int_{a_1(t)}^{a_2(t)} \rho \left(\frac{1}{2} u^2 + \varepsilon \right) \, dn = p_1 u_1 - p_2 u_2 \tag{2.70}$$

To evaluate the left hand side, we treat the integral as before, separating the upstream and downstream sides and employing Leibniz's integral rule to obtain,

$$\int_{a_1(t)}^{a_2(t)} \frac{\partial}{\partial t}\left[\rho\left(\frac{1}{2}u^2+\varepsilon\right)\right] dn + \left[\rho_1\left(\frac{1}{2}u_1^2+\varepsilon_1\right)\right](U-u_1) + \\ + \left[\rho_2\left(\frac{1}{2}u_2^2+\varepsilon_2\right)\right](u_2-U) = p_1u_1 - p_2u_2 \tag{2.71}$$

Recall the internal energy for planar disks is the granular temperature T, and take the shock speed to be zero (or, equivalently, treat u_1, u_2 as the normal flow speeds *relative* to the shock). Again, the remaining integral tends to zero in the infinitesimal limit of the control volume,

$$-\left[\rho_1\left(\frac{1}{2}u_1^2+T_1\right)\right]u_1 + \left[\rho_2\left(\frac{1}{2}u_2^2+T_2\right)\right]u_2 = p_1u_1 - p_2u_2 \tag{2.72}$$

Rearrange,

$$\rho_1u_1\left[\frac{p_1}{\rho_1}+\frac{1}{2}u_1^2+T_1\right] = \rho_2u_2\left[\frac{p_2}{\rho_2}+\frac{1}{2}u_2^2+T_2\right] \tag{2.73}$$

By (2.44), we are left with the final energy balance,

$$\frac{p_1}{\rho_1}+\frac{1}{2}u_1^2+T_1 = \frac{p_2}{\rho_2}+\frac{1}{2}u_2^2+T_2 \tag{2.74}$$

2.3.5 Jump Conditions

We summarize the four jump conditions derived from mass, momentum, and energy considerations, phrasing in terms of the shock–oriented velocity components u_1, w_1, u_2, and w_2. Additionally we change variables from density ρ to area fraction ν,

$$\nu_1u_1 = \nu_2u_2 \tag{2.75}$$

$$p_1 + \rho_m\nu_1u_1^2 = p_2 + \rho_m\nu_2u_2^2 \tag{2.76}$$

$$w_1 = w_2 \tag{2.77}$$

$$\frac{p_1}{\rho_m \nu_1} + \frac{1}{2}u_1^2 + T_1 = \frac{p_2}{\rho_m \nu_2} + \frac{1}{2}u_2^2 + T_2 \tag{2.78}$$

With the exception of the energy equation (2.78) where $\varepsilon = T$ was employed, these equations are completely general for any changes across a surface of discontinuity. If (2.78) were left in terms of the internal energy, they are indeed applicable for any continuum. Similar expressions for a perfect gas may be found in [2]. It should be noted that finite mass flow across the shock was necessary for relation (2.77). In the absence of mass flux, a degenerate solution is obtained where $u_1 = u_2 = U = 0$ and $p_1 = p_2$, and the shock is termed a *contact surface* [5]. Such a situation permits a discontinuity in the tangential velocity component and (2.77) is no longer valid.

2.3.6 Alternative Phrasing

For the purposes of the derivation of jump conditions, the shock–oriented equations were a convenient phrasing. However, specification of the velocity components u_1, u_2, w_1, w_2 implicitly involved the unknown shock orientation β. If we wish to write these equations explicitly in terms of upstream quantities and β, we make the following substitutions based on the geometry of the shock,

$$u_1 = V_1 \sin\beta \tag{2.79}$$

$$w_1 = V_1 \cos\beta \tag{2.80}$$

$$u_2 = V_2 \sin(\beta - \theta) \tag{2.81}$$

$$w_2 = V_2 \cos(\beta - \theta) \tag{2.82}$$

which leads to,

$$\nu_1 V_1 \sin\beta = \nu_2 V_2 \sin(\beta - \theta) \tag{2.83}$$

$$p_1 + \rho_m \nu_1 V_1^2 \sin^2\beta = p_2 + \rho_m \nu_2 V_2^2 \sin^2(\beta - \theta) \tag{2.84}$$

$$V_1 \cos\beta = V_2 \cos(\beta - \theta) \tag{2.85}$$

$$T_1 + \frac{p_1}{\rho_m \nu_1} + \frac{V_1^2 \sin^2\beta}{2} = T_2 + \frac{p_2}{\rho_m \nu_2} + \frac{V_2^2 \sin^2(\beta - \theta)}{2} \tag{2.86}$$

In this form, the jump equations explicitly display their dependence upon the variables of interest V_2, p_2, ν_2, and either θ or β.

2.3.7 Manipulation of the Jump Conditions

In this section we solve the system of four algebraic equations in the four unknowns ν_2, V_2, β, and p_2 (or equivalently T_2). Since we wish to determine β explicitly, we employ the phrasing of section 2.3.6. The local flow turning angle θ is treated as known, as are the upstream flow conditions. Note that the choice of V_2 and β as variables is not a unique approach to the solution; one could just as well choose to solve in terms of u_2 and w_2, the post–shock flow speeds normal and tangential to the shock, respectively.

As stated in Section 2.3.5, these continuity and momentum relations are in fact the same for any discontinuous transport process. The energy expression has already made use of the equivalence of temperature and internal energy. We differ from the perfect gas model by a granular equation of state relating the pressure and temperature, equation (2.12). With the equation of state, we have the option to solve in terms of either temperature or pressure. In what follows, the temperature is chosen, and the normal momentum and energy jump conditions become,

$$p_1 + \rho_m \nu_1 V_1^2 \sin^2\beta - \rho_m \nu_2 \left(1 + 2G_2\right) T_2 - \rho_m \nu_2 V_2^2 \sin^2(\beta - \theta) = 0 \tag{2.87}$$

$$T_1 + \frac{p_1}{\rho_m \nu_1} + \frac{V_1^2 \sin^2\beta}{2} - T_2 - (1 + 2G_2)\, T_2 - \frac{V_2^2 \sin^2(\beta - \theta)}{2} = 0 \tag{2.88}$$

where $G_2 = G_2(\nu_2)$ denotes the function of area fraction in terms of ν_2.

To begin, we first solve equation (2.83) for $\sin(\beta - \theta)$,

$$\sin(\beta - \theta) = \frac{\nu_1 V_1 \sin\beta}{\nu_2 V_2} \tag{2.89}$$

Next, we substitute this into equation (2.87) and solve for T_2,

$$T_2 = \frac{p_1/\rho_m + \nu_1 V_1^2 \sin^2\beta \left(1 - \frac{\nu_1}{\nu_2}\right)}{\nu_2 \left(1 + 2G_2\right)} \tag{2.90}$$

Now we may use this expression and (2.89) with equation (2.88)

$$\begin{aligned} T_1 + \frac{p_1}{\rho_m \nu_1} + \frac{V_1^2 \sin^2\beta}{2} - \frac{p_1/\rho_m + \nu_1 V_1^2 \sin^2\beta \left(1 - \frac{\nu_1}{\nu_2}\right)}{\nu_2 \left(1 + 2G_2\right)} - \\ - \frac{p_1/\rho_m + \nu_1 V_1^2 \sin^2\beta \left(1 - \frac{\nu_1}{\nu_2}\right)}{\nu_2} - \frac{\nu_1^2 V_1^2 \sin^2\beta}{2\nu_2^2} = 0 \end{aligned} \tag{2.91}$$

Use the expression for $(1 + 2G_2)$ from the equation of state,

$$\begin{aligned} T_1 + \frac{p_1}{\rho_m \nu_1} + \frac{V_1^2 \sin^2\beta}{2} - \frac{8(1-\nu_2)^2 \left[p_1/\rho_m + \nu_1 V_1^2 \sin^2\beta \left(1 - \frac{\nu_1}{\nu_2}\right)\right]}{\nu_2 \left(8 + \nu_2^2\right)} - \\ - \frac{p_1/\rho_m + \nu_1 V_1^2 \sin^2\beta \left(1 - \frac{\nu_1}{\nu_2}\right)}{\nu_2} - \frac{\nu_1^2 V_1^2 \sin^2\beta}{2\nu_2^2} = 0 \end{aligned}$$

which may be simplified to,

$$\begin{aligned} 2\nu_2^2(8 + \nu_2^2) \left[T_1 + \frac{p_1}{\rho_m \nu_1}\right] + \\ + \left[\nu_2^4 - 18\nu_1\nu_2^3 + (17\nu_1^2 + 32\nu_1 + 8)\nu_2^2 - \right. \\ \left. - 32(\nu_1 + \nu_1^2)\nu_2 + 24\nu_1^2\right] V_1^2 \sin^2\beta - \\ - \frac{p_1}{\rho_m} \left[18\nu_2^3 - 32\nu_2^2 + 32\nu_2\right] = 0 \end{aligned} \tag{2.92}$$

Note that we may combine quantities in (2.92) to express in dimensionless form. With the equation of state we write $p_1/(\rho_m \nu_1) = (1 + 2G_1)T_1$. Following this, we divide by V_1^2 to obtain,

$$\begin{aligned} 2\nu_2^2(8+\nu_2^2)\left[\frac{(2+2G_1)T_1}{V_1^2}\right] + \\ + \left[\nu_2^4 - 18\nu_1\nu_2^3 + (17\nu_1^2 + 32\nu_1 + 8)\nu_2^2 - \right. \\ \left. -32(\nu_1+\nu_1^2)\nu_2 + 24\nu_1^2\right]\sin^2\beta - \\ -\frac{\nu_1 T_1(1+2G_1)}{V_1^2}\left[18\nu_2^3 - 32\nu_2^2 + 32\nu_2\right] = 0 \end{aligned} \tag{2.93}$$

Define $\Sigma \equiv T_1/V_1^2$ and simplify to obtain a quartic function in ν_2,

$$\begin{aligned} \left[16(1-\nu_1)^2\sin^2\beta + 4\Sigma(9\nu_1^2 - 16\nu_1 + 16)\right]\nu_2^4 - \\ - \left[288\nu_1(1-\nu_1)^2\sin^2\beta + 36\Sigma(8\nu_1 + \nu_1^3)\right]\nu_2^3 + \\ + \left[16(1-\nu_1)^2(17\nu_1^2 + 32\nu_1 + 8)\sin^2\beta + 32\Sigma(2\nu_1^3 + 9\nu_1^2 + 16)\right]\nu_2^2 - \\ - \left[512(1-\nu_1)^2(\nu_1+\nu_1^2)\sin^2\beta + 64\Sigma(8\nu_1 + \nu_1^3)\right]\nu_2 + \\ +384\nu_1^2(1-\nu_1)^2\sin^2\beta = 0 \end{aligned} \tag{2.94}$$

We plot this quartic in Figure 2.4 for trial values of ν_1, Σ, and β.

By inspection of the function we see $\nu_2 = \nu_1$ is a solution of this system of algebraic equations corresponding to either a contact surface (if the mass flux is zero), or the preservation of upstream flow conditions in the minimally weak shock. Note that for the specific shock angle $\beta = \beta_{min}$ (the Mach Angle– see Section 2.4) we have a repeated real root at $\nu_2 = \nu_1$. We factor out this solution, which leaves

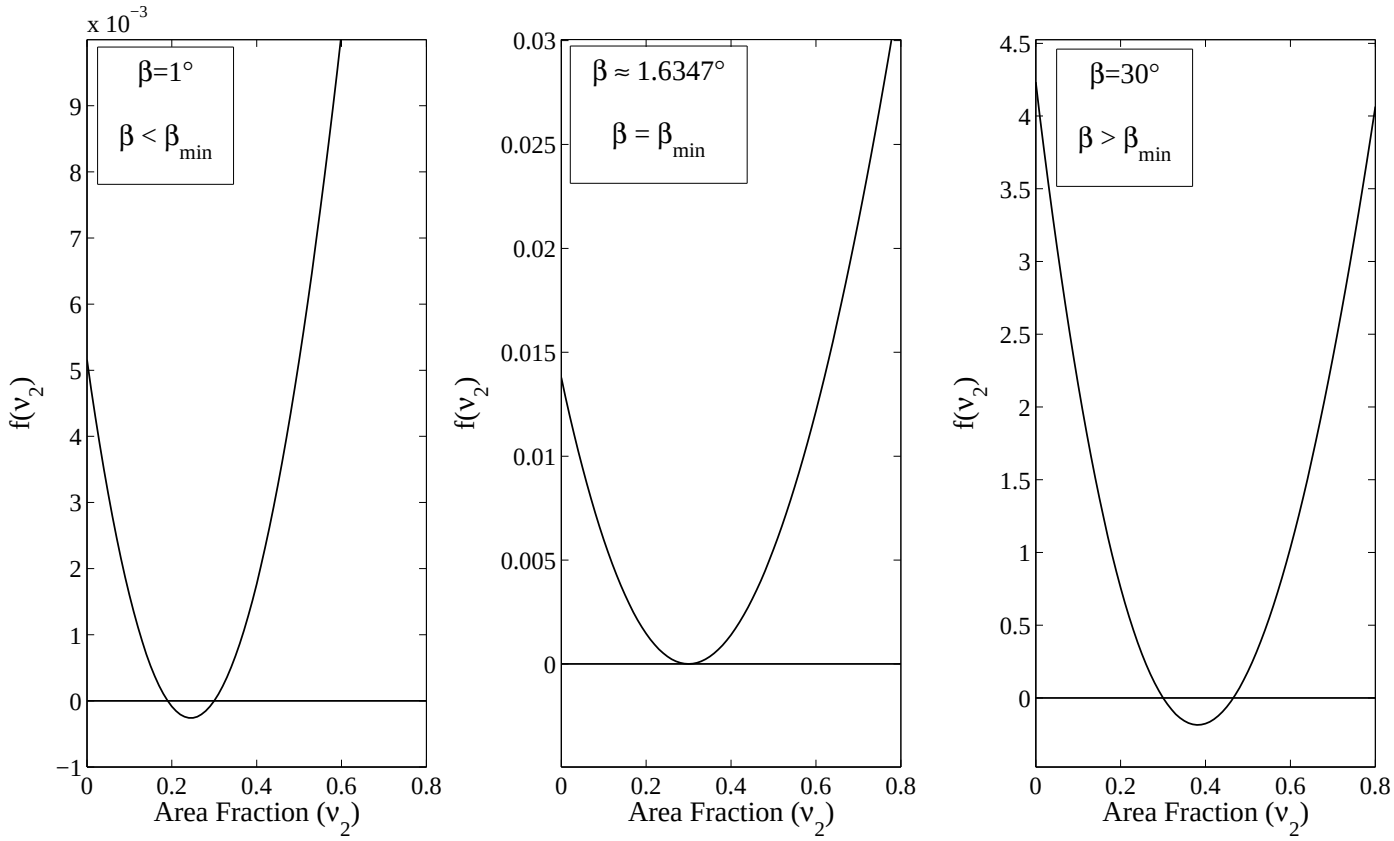

Figure 2.4: Equation (2.94) plotted for $\nu_1 = 0.3$ and $\Sigma = 10^{-4}$ for three values of β. Discussion of the minimum shock angle β_{min} is left to Section 2.4.

the post–shock density as a solution to the cubic,

$$\begin{aligned}\left[16(1-\nu_1)^2\sin^2\beta + 4\Sigma(9\nu_1^2 - 16\nu_1 + 16)\right]\nu_2^3 - \\ - \left[272\nu_1(1-\nu_1)^2\sin^2\beta + 32\Sigma(7\nu_1 + 2\nu_1^2)\right]\nu_2^2 + \\ + \left[128(1-\nu_1)^2(1+4\nu_1)\sin^2\beta + 64\Sigma(\nu_1^2+8)\right]\nu_2 - \\ - \left[384\nu_1(1-\nu_1)^2\sin^2\beta\right] = 0 \end{aligned} \tag{2.95}$$

Note that there remain two unknowns β, ν_2 in the cubic relation above. We seek to replace β using our remaining jump conditions. We use (2.83) and (2.85) to write,

$$\frac{\nu_1}{\nu_2} \equiv r = \frac{\tan(\beta-\theta)}{\tan\beta} \tag{2.96}$$

With the identity,

$$\tan(\beta-\theta) = \frac{\tan\beta - \tan\theta}{1+\tan\beta\tan\theta} \tag{2.97}$$

we solve (2.96) for $\tan\beta$,

$$\tan\beta = \frac{(1-r) \pm \sqrt{(r-1)^2 - 4r\tan^2\theta}}{2r\tan\theta} \equiv \Phi \tag{2.98}$$

so $\beta = \tan^{-1}\Phi$ and

$$\sin^2\beta = \sin^2(\tan^{-1}\Phi) = \frac{\Phi^2}{\Phi^2+1} \tag{2.99}$$

Note that (2.98) admits the possibility of real and imaginary solutions for β. As a physical quantity, we only consider real values where the discriminant $(r-1)^2 - 4r\tan^2\theta \geq 0$. Consideration of issues related to the existence of real solutions is deferred to a later discussion (see Section 3.2.1). At the moment we assume area fractions and θ such that we obtain 1 or 2 real solutions for β. Of the two possible solutions, we consider only the *weak* solution arising from the difference of terms in the numerator of (2.98). The weak solution corresponds to the lesser of the two

possible shock angles, and is often the experimentally observed configuration [2,25]. However, strong shocks have been created experimentally in free–surface flows over obstructing wedges [10].

With this and (2.95) we numerically solve to find the post–shock area fraction ν_2. The remaining post–shock flow properties and β follow from (2.83), (2.90), and (2.98). We plot the cubic (2.95) in Figure 2.5 for several β values. As we expect, we obtain shocks ($\nu_2 \geq \nu_1$) for $\beta \geq \beta_{min}$.

2.3.8 Dilute Limit

In the dilute limit we have $p = \rho_m \nu T$ and $G(\nu) \ll 1$, and (2.90) becomes,

$$T_2 = \frac{p_1/\rho_m + \nu_1 V_1^2 \sin^2\beta \left(1 - \frac{\nu_1}{\nu_2}\right)}{\nu_2} \tag{2.100}$$

The energy equation (2.88) reduces to,

$$2T_1 + \frac{V_1^2 \sin^2\beta}{2} - 2T_2 - \frac{V_2^2 \sin^2(\beta - \theta)}{2} = 0 \tag{2.101}$$

We use (2.100) and (2.89) to write

$$2T_1 + \frac{V_1^2 \sin^2\beta}{2} - 2\left[\frac{p_1/\rho_m + \nu_1 V_1^2 \sin^2\beta \left(1 - \frac{\nu_1}{\nu_2}\right)}{\nu_2}\right] - \frac{V_2^2}{2}\left[\frac{\nu_1 V_1 \sin\beta}{\nu_2 V_2}\right]^2 = 0$$

which simplifies to a quadratic in the density ratio r,

$$\left(3V_1^2 \sin^2\beta\right) r^2 - \left(4V_1^2 \sin^2\beta + 4T_1\right) r + V_1^2 \sin^2\beta + 4T_1 = 0 \tag{2.102}$$

solving to,

$$r = \frac{2(V_1^2 \sin^2\beta + T_1) \pm (V_1^2 \sin^2\beta - 2T_1)}{3V_1^2 \sin^2\beta}$$

and the solutions are the trivial solution of $r = 1$ ($\nu_2 = \nu_1$) and

$$r = \frac{V_1^2 \sin^2\beta + 4T_1}{3V_1^2 \sin^2\beta} \tag{2.103}$$

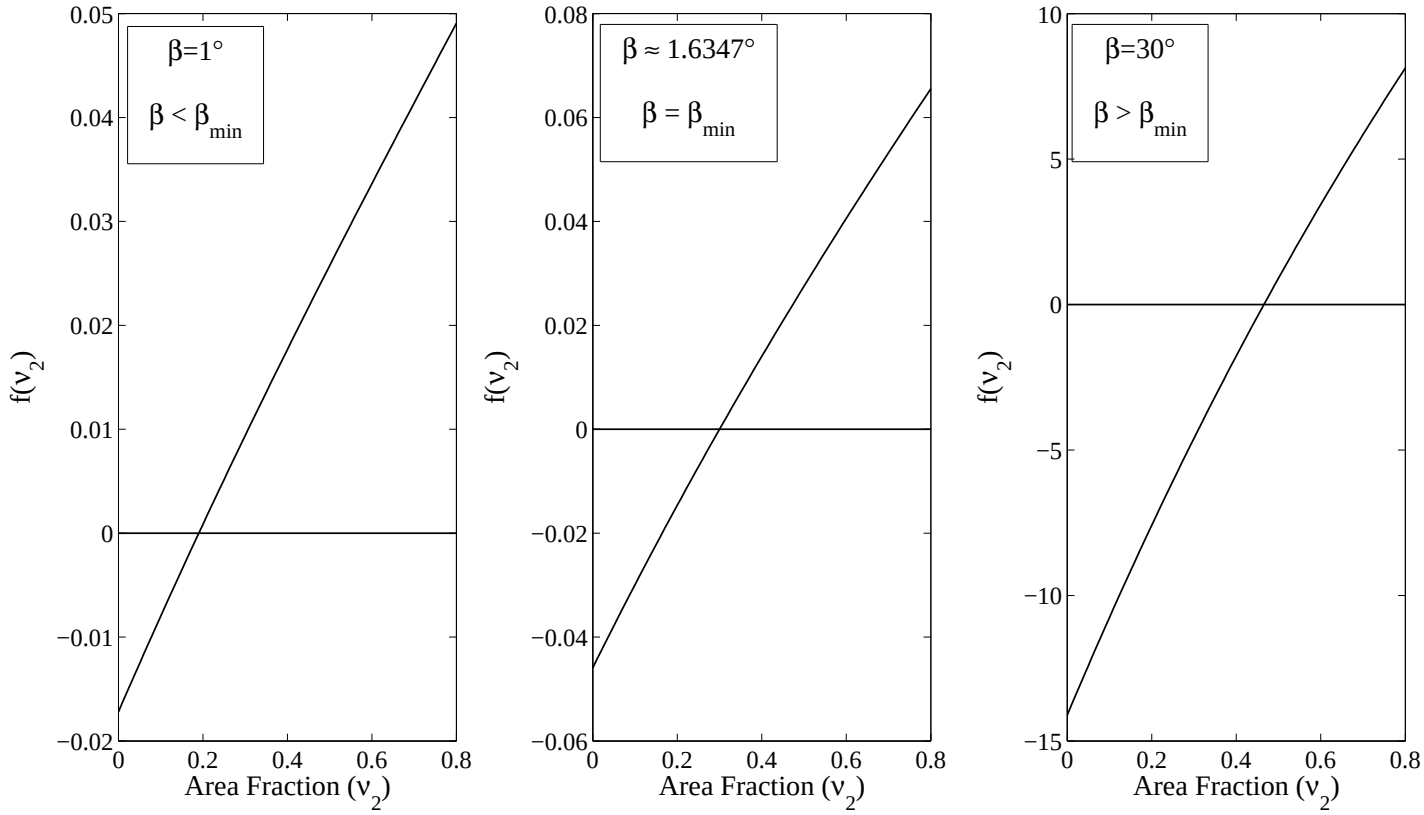

Figure 2.5: Equation (2.95) plotted for $\nu_1 = 0.3$ and $\Sigma = 10^{-4}$ for three values of β. Discussion of the minimum shock angle β_{min} is left to Section 2.4.

or,

$$\nu_2 = \frac{3\nu_1 V_1^2 \sin^2\beta}{V_1^2 \sin^2\beta + 4T_1} \tag{2.104}$$

and the remaining post–shock properties follow accordingly.

2.4 $\beta-\theta$ Relations

In the study of compressible gas dynamics, it is common to plot the shock angle β as the flow turning angle θ varies. In the case of the perfect gas ($p = \rho\Re T$), there is a maximum flow turning angle, θ_c, such that $0 \leq \theta \leq \theta_c$ while $\beta_{min} \leq \beta \leq \pi/2$. β_{min} is the minimum shock angle, discussed below. See, for example, reference [1]. We look to construct plots of this nature for the granular shock transition. Gray [10] also constructs β–θ relations for the case of free-surface flows in gravitational fields.

In a perfect gas, it is possible to obtain a closed–form function relating θ and β given the upstream Mach Number M– the "θ–β–M" relation. Upstream conditions are incorporated in the Mach Number, defined as the ratio of the incoming flow speed and the sound speed,

$$M = \frac{V_1}{\mathfrak{a}} \tag{2.105}$$

In the case of the perfect gas, recall $\mathfrak{a}_{pg} = \sqrt{\gamma_g \Re T}$ and the Mach Number may be defined only by the ratio $\Sigma = T_1/V_1^2$, with no density dependence. The resulting family of curves differ only be specification of the Mach number. However, the non–linear density dependence of the granular equation of state does not facilitate writing a closed form θ–β–M expression, except in the dilute limit when $G(\nu) \to 0$ and $p = \rho_m \nu T$. Note from (2.27) that our expression for the equilibrium sound speed is a function of both temperature and area fraction. As shown in (2.95), the

relationship between turning angle θ and shock angle β is also a function of Σ and the initial area fraction ν_1. Anderson [1] confirms that the inclusion of real gas effects in the modeling precludes the ability to characterize the $\beta-\theta$ relations in terms of only the Mach number.

To construct the desired plot, we regard β as a known value and consider the turning angle θ as unknown. Without the ability to explicitly determine the maximum flow turning angle θ_c as a function of upstream quantities, we are unable to specify a range of θ on which to solve for β. [Note that it is possible to determine $\theta_c = \theta_c(\nu_1, \Sigma)$, but our equations do not permit a simple expression. See Section 3.2.1 for a discussion of θ_c.] Solving with β as the independent variable makes knowledge of θ_c unnecessary. With (2.95) solved for ν_2, we employ (2.96), solved for θ,

$$\tan\theta = \frac{(1-r)\tan\beta}{1 + r\tan^2\beta} \tag{2.106}$$

With this, we are able to determine θ as β is varied through angles $\beta_{min} \leq \beta \leq \pi/2$, provided β_{min} is known. Unlike θ_c, we are able to readily obtain an expression for β_{min} in terms of upstream quantities V_1, T_1, and ν_1.

As shown in Figure 2.4, the two real roots of the quartic include the trivial solution as well as a second root corresponding to a density increase (shock) or decrease (rarefaction). There remains the transition between these situations where (2.94) features a repeated real root or a single root of the cubic (2.95) at $\nu_2 = \nu_1$. This defines the Mach Angle– the limit of the weak shock where $\beta = \beta_{min}$ and $\theta = 0$. Recall Figure 2.1 from our general discussion of supersonic flow and signal transmission. The envelope of transmitted signals defining the Mach Angle can be

determined by examination of the geometry,

$$\sin(\beta_{min}) = \frac{\mathfrak{a}(n\Delta t)}{V(n\Delta t)} = \frac{\mathfrak{a}}{V}$$

$$\beta_{min} = \sin^{-1}\left(\frac{1}{M}\right) \tag{2.107}$$

Implementing this repeated root at $\nu_2 = \nu_1$ in the cubic equation (2.95), we have

$$\begin{aligned}
&\left[16(1-\nu_1)^2\sin^2\beta + 4\Sigma(9\nu_1^2 - 16\nu_1 + 16)\right]\nu_1^3 - \\
&- \left[272\nu_1(1-\nu_1)^2\sin^2\beta + 32\Sigma(7\nu_1 + 2\nu_1^2)\right]\nu_1^2 + \\
&+ \left[128(1-\nu_1)^2(1+4\nu_1)\sin^2\beta + 64\Sigma(\nu_1^2+8)\right]\nu_1 - \\
&-384\nu_1(1-\nu_1)^2\sin^2\beta = 0
\end{aligned}$$

which solves for $\sin\beta$,

$$\sin^2\beta = \frac{\Sigma\left[9\nu_1^4 - 32\nu_1^3 - 24\nu_1^2 + 128\right]}{64(1-\nu_1)^4} \tag{2.108}$$

Since this case defines the minimally weak shock β_{min}, we compare to (2.107),

$$\frac{\mathfrak{a}^2}{V^2} = \frac{T_1\left[9\nu_1^4 - 32\nu_1^3 - 24\nu_1^2 + 128\right]}{64V_1^2(1-\nu_1)^4} \tag{2.109}$$

We identify the speed V here as exactly the speed (V_1) of the incident flow. As viewed from a reference frame on the wedge, the disturbing body propagates into the upstream flow at speed V_1. Thus we are left with,

$$\frac{\mathfrak{a}^2}{T_1} = \frac{9\nu_1^4 - 32\nu_1^3 - 24\nu_1^2 + 128}{64(1-\nu_1)^4} \tag{2.110}$$

Note that this result is equivalent to our sound speed derived from the equilibrium thermodynamic analysis of Section 2.2. However, these relations are not independent – the isentropic thermodynamic laws used to derive (2.27) are employed in the transport equations used to determine the jump relations.

With the value of β_{min} determined for given upstream conditions, we are able to construct the $\beta - \theta$ plots of interest. To begin, we specify upstream conditions ν_1 and Σ. Upon calculating the sound speed, the Mach Number and β_{min} are determined. We iterate for $\beta_{min} \leq \beta \leq \pi/2$ and use MATLAB's root finding algorithm `fzero()` to determine a numerical solution of (2.95). Figures 2.6 and 2.7 plot the $\beta - \theta$ relations for varying area fraction ν_1 and Σ.

We note that Gray [10] derives $\beta - \theta$ relations for dense free–surface flows in gravitational fields. With the inclusion of scaling related to the gravitational acceleration g, they define a characteristic wave speed related to system dimensions and flow deflection angle. Subsequently their relations are not given in terms of a Mach number, but rather a Froude (Fr) number defined as the ratio of flow speed to this wave speed. They are able to obtain a closed form $\beta - \theta$ relation in terms of this measure which agrees well with experiment and computations at moderate to high Fr. At fixed Fr, observed θ_c values far exceed those obtained for our two–dimensional granular gas.

2.4.1 Dilute Limit

Recall that in the dilute limit the post–shock area fraction is given by the solution of a quadratic, with a solution given by (2.104). With (2.106) we have,

$$\tan\theta = \frac{(2\sin^2\beta - 4\Sigma)\tan\beta}{3\sin^2\beta + \tan^2\beta(\sin^2\beta + 4\Sigma)} \tag{2.111}$$

Note that for the dilute granular gas the upstream Mach Number (M_1) is given by (2.105) and (2.30),

$$M_1 = \frac{V_1}{\mathfrak{a}_d} = \frac{V_1}{\sqrt{2T_1}}$$

so we can express the Mach Number in terms of $\Sigma = T_1/V_1^2$

$$M_1^2 = \frac{1}{2\Sigma} \tag{2.112}$$

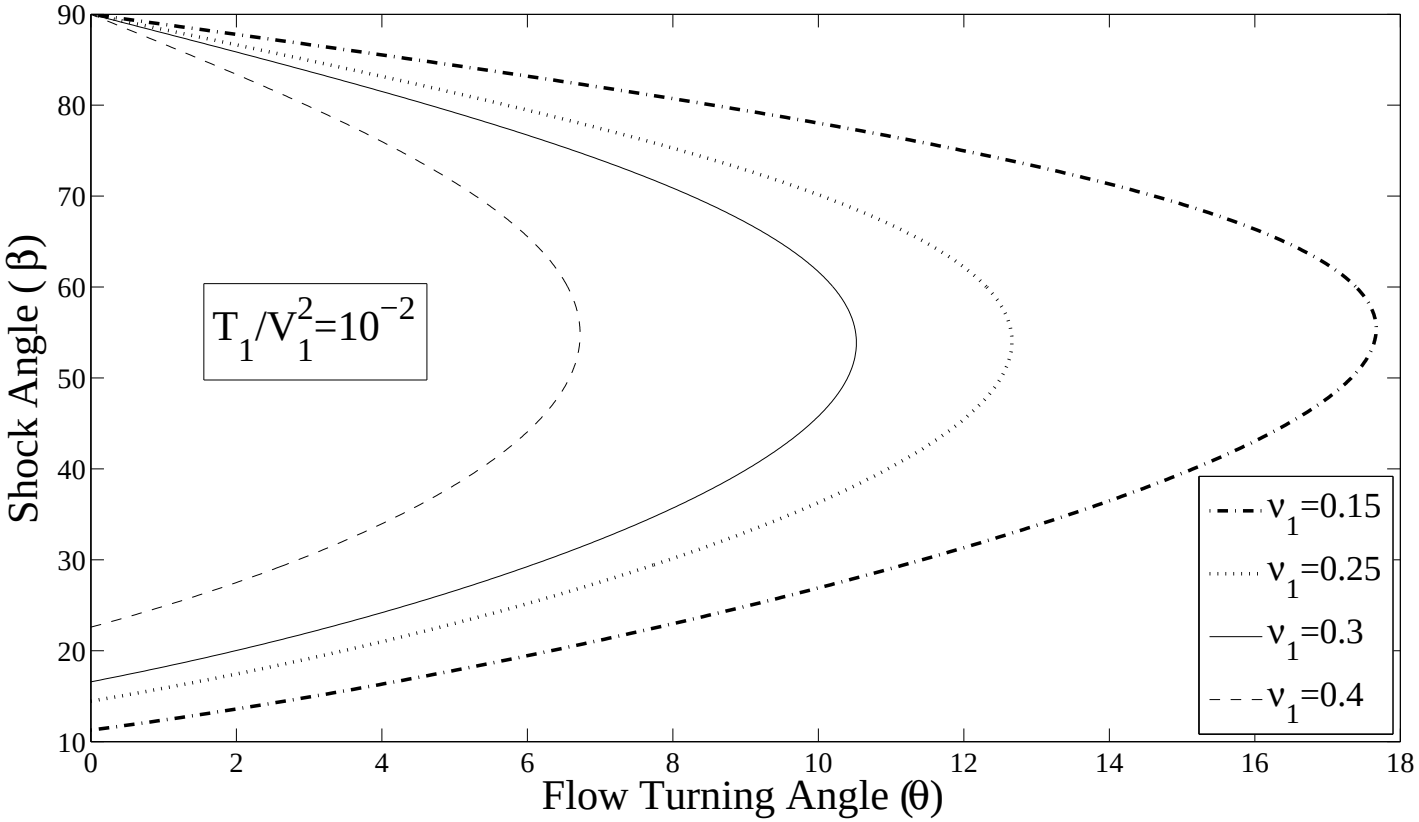

Figure 2.6: Equations (2.106) plotted for varied ν_1 and $\Sigma = 10^{-2}$.

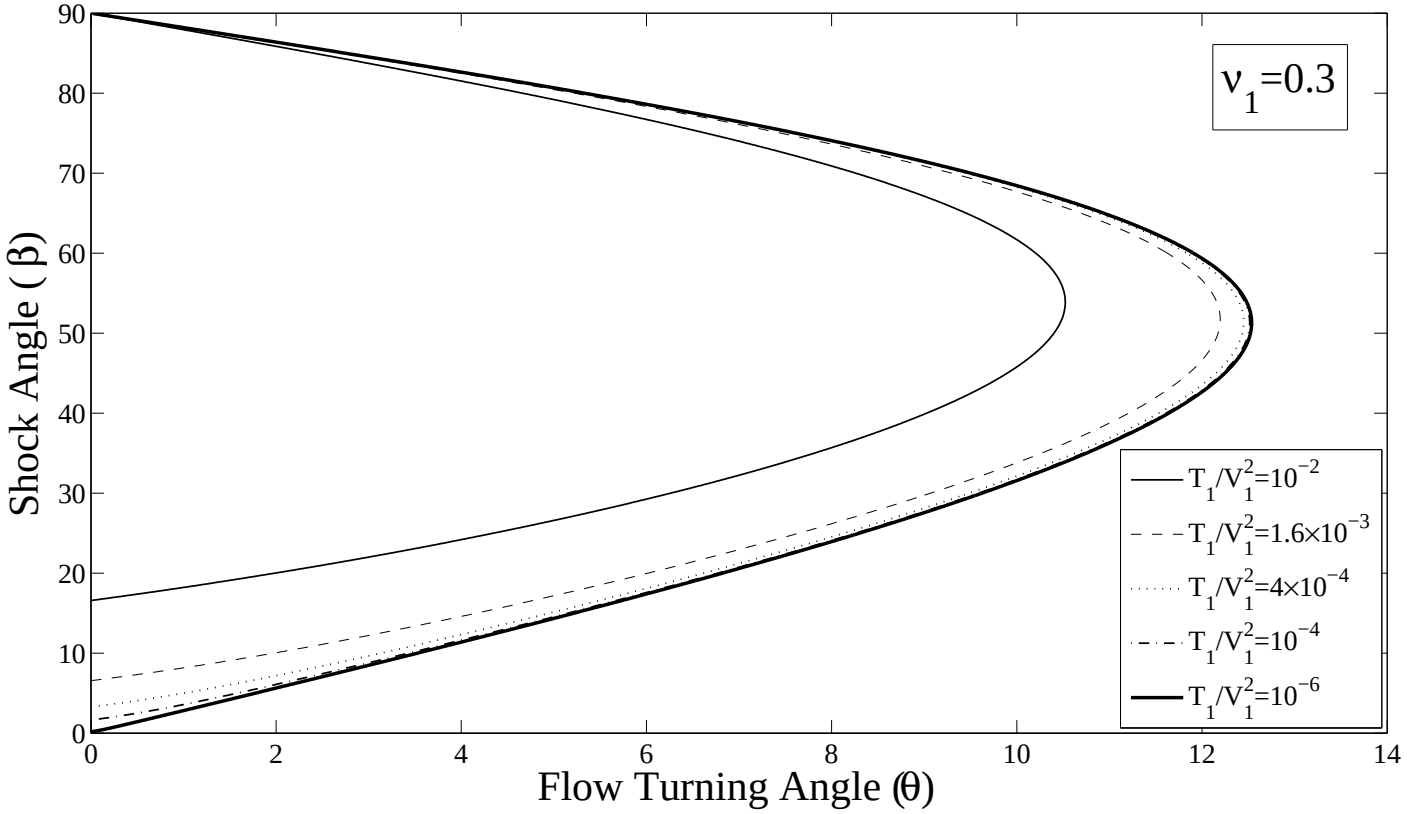

Figure 2.7: Equations (2.106) plotted for $\nu_1 = 0.3$ and varied Σ values.

and we can express (2.111) in terms of the Mach Number,

$$\tan\theta = \frac{2(M_1^2 \sin^2\beta - 1)\tan\beta}{3M_1^2 \sin^2\beta + \tan^2\beta(M_1^2 \sin^2\beta + 2)} \tag{2.113}$$

As in the case of the perfect gas, the $\beta - \theta$ relations are characterized in terms of a single parameter– the upstream Mach Number. For values of $\nu_1 = 0.3$, $\Sigma = 4\times10^{-4}$ we plot (2.106) and (2.113) in Figure 2.8.

2.5 The Straight Wedge– Comparison of Analytical and Numerical Results

The shock relations developed thus far have been entirely general for application to planar flows of identical disks with no body force. We have assumed the presence of a shock locally inclined at angle β to the incoming flow and examined the change in flow properties, namely the turning angle θ. The choice of β or θ as the independent variable was arbitary, often determined by convenience as in the plotting of the $\beta - \theta$ curves. Note that there has been no mention of the global shock shape– only a local analysis has been performed. In general, β may vary and the shock is curved.

A more practical view of the problem aims to analyze the shock front caused by a physical body of prescribed shape. In this context, the natural independent variable is θ, the local turning angle of the flow induced by the body. Note that in general, the flow turning angle and the body inclination are not equivalent. However, in the case of the straight wedge of $\theta \leq \theta_c$ (See Figure 2.10) we are able to assume that the flow and body angles are indeed the same, suggested by inspection of streamlines in Figure 2.9. This assumption of wedge alignment is confirmed by experimentation and numerics [10, 25]. We exploit this canonical

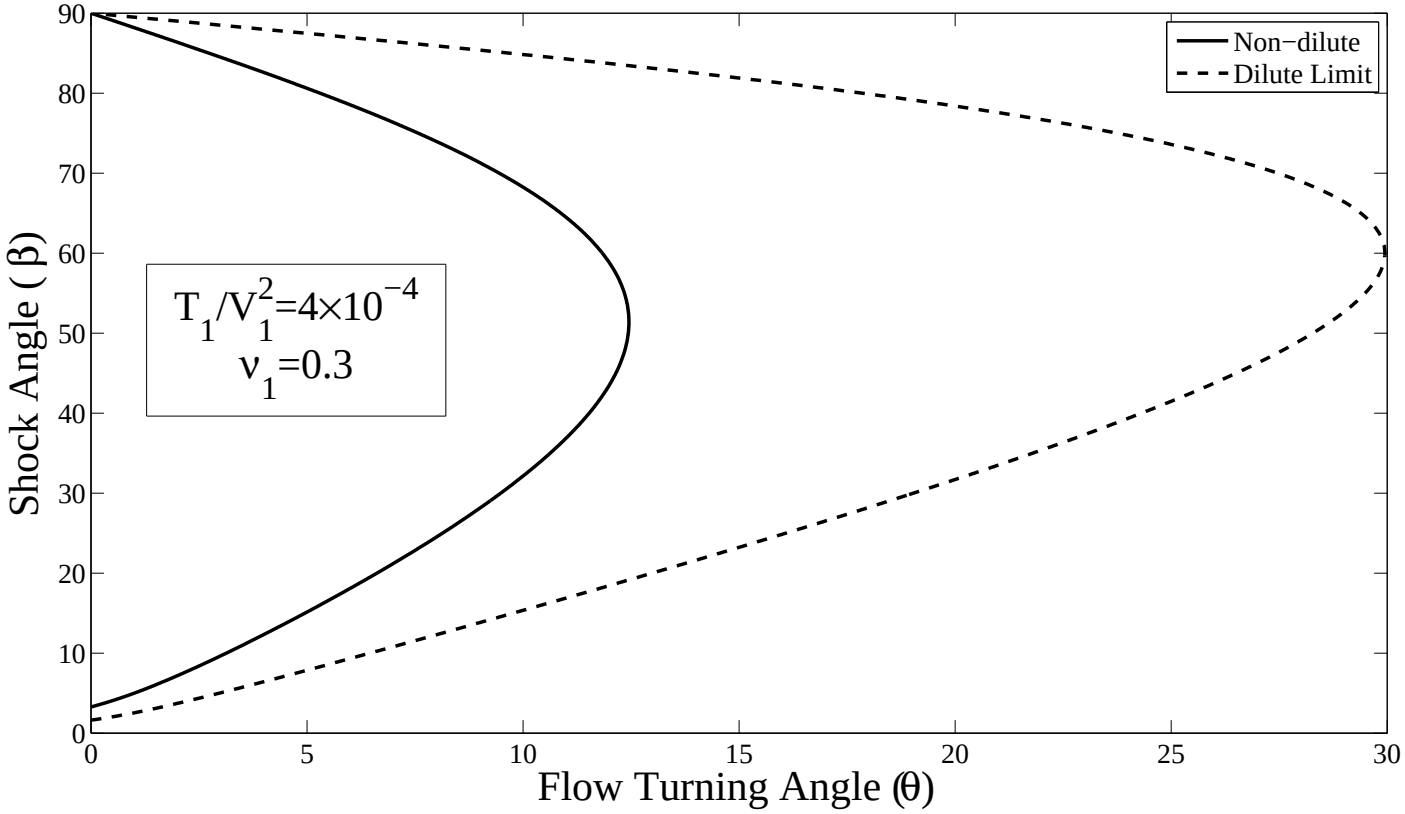

Figure 2.8: Equations (2.106) and (2.113) plotted for $\nu_1 = 0.3$ and $\Sigma = 4 \times 10^{-4}$.

geometry to compare discrete element simulations and the theory developed above.

2.5.1 Numerical Simulations

To examine the predictions of the analytical model, we employ a discrete event–driven *n–body* simulation of identical disks in the plane. We specify an upstream uniform flow of known properties incident on a wedge of inclination θ and examine the resulting shock and post–shock properties. Here we discuss the principles of the simulation.

To begin the simulation, we specify its spatial extent and establish a computational grid to track particle locations. The size of the simulation ($W \times H$ in Figure 2.10) and the height of the incident flow (h) must be large enough to completely envelop the shocked region, denoted by a dotted line at inclination β in the figure. That is, we do not wish to introduce effects due to an absence of mass flux to the shock. Wedge inclination θ, wedge length L, and particle diameter d are also controlled by the user. A constant flux of incoming particles is supplied and particles leave the domain upon reaching the end the wedge.

We employ a computational grid to aid in the tracking of contacts. Each simulation particle occupies a unique grid position and we specify a range of adjacent cells in which to search for potential collisions (Figure 2.11). This search range is dependent on the time step duration and the speed of the particles. By this construction, we assemble a list of every particle's neighbors, avoiding an extensive global search. Contacts are verified by computation of the distance between the centers of these neighboring particles.

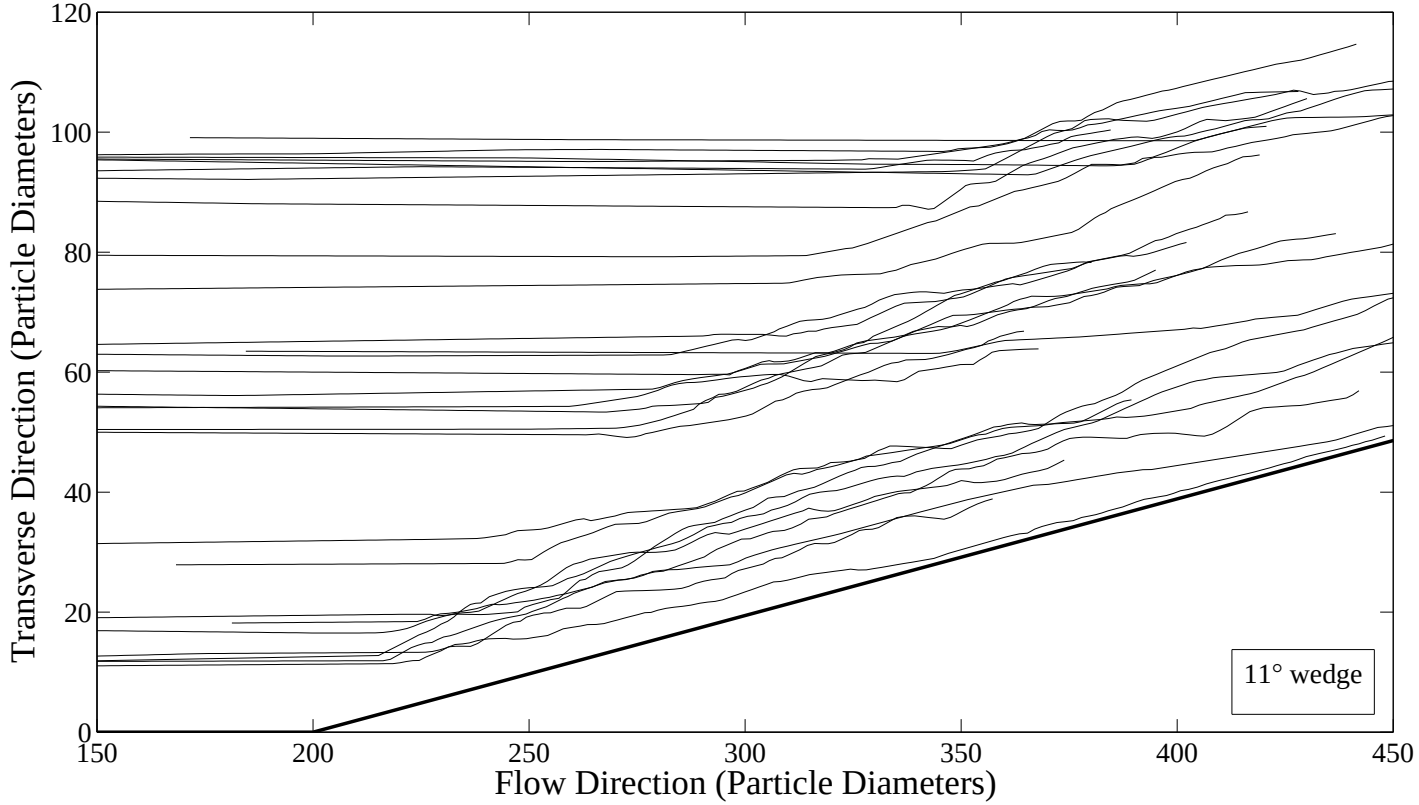

Figure 2.9: Particle streamlines for sample particles incident on 11° wedge. $T_1/V_1^2 = 225^{-1}$ and $\nu_1 = 0.3$

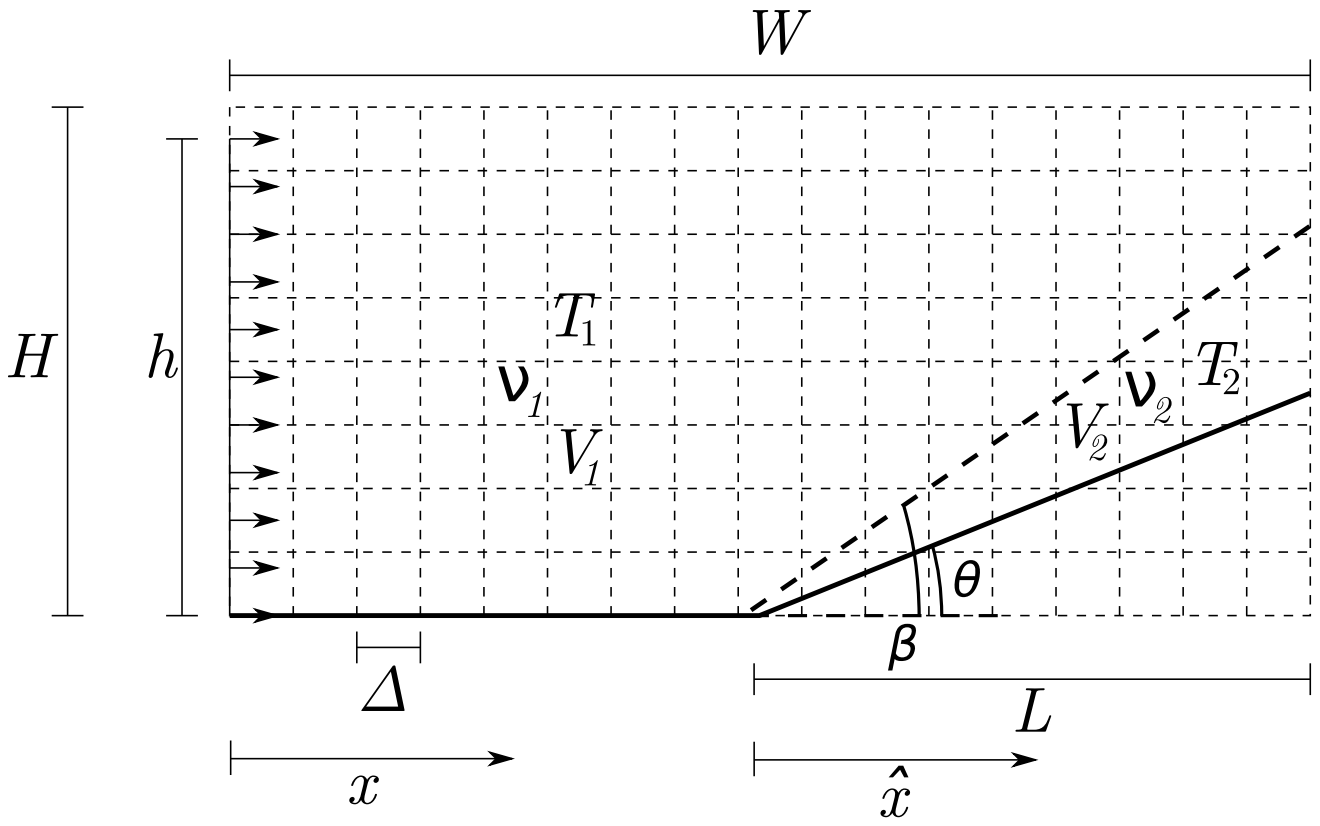

Figure 2.10: A flow of known conditions encounters the wedge of angle $\theta \leq \theta_c$, creating a straight shock inclined at β.

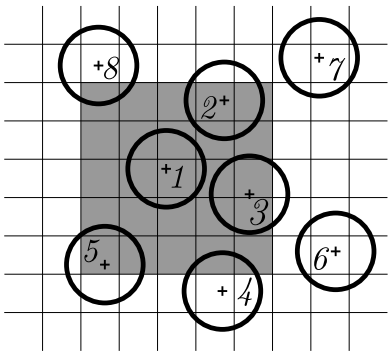

Figure 2.11: The computational grid. Consider searching for neighbors of particle 1 in a prescribed range of cells, highlighted in grey. Particles 2, 3, and 5 are neighbors of particle 1.

The spacing of the computational grid is determined by particle diameter and has an upper bound of $\Delta = d/\sqrt{2}$ to ensure that two particles do not occupy the same grid location. In practice, however, particle displacements in the finite time step may result in multiple particles occupying the same grid position, which is cause for a program error to be identified. For this reason we typically choose a spatially finer grid at computational expense. An alternative approach is to decrease the time step duration, which incurs similar costs through increased simulation time.

The neighbor searching algorithm requires a similar balance between program efficiency and the ability to effectively resolve contacts. We seek to capture all potential collisions with the particle of interest, yet we want to minimize the search region. We also note that it is not necessary to perform a grid search at every time step– neighboring particles are likely to remain the same within an adequately short time duration. Estimates for the searching region and search time interval

are determined by the highest speed particles in the system. In our study, conservative parameters are specified to minimize the possibility of run–time errors.

In our simulations we treat interactions as perfectly elastic, instantaneous binary collisions. It is possible to model collisional energy loss (perhaps through a coefficient of restitution as in Chapter 4), but we do not consider this here. We also neglect frictional interaction– particle rotations are not considered. Although tangential interaction may be important in particular situations, we consider dilute to moderate area fractions where collisions dominate the momentum transfer with few enduring contacts. If we define $\mathbf{g} \equiv \mathbf{c}_1 - \mathbf{c}_2$ as the relative velocity of a pair of particles and $\mathbf{k}$ as a unit vector from the center of particle 1 to the center of particle 2, the pre and post–collision relative velocities are simply reversed so that,

$$g'_\alpha k_\alpha = -g_\alpha k_\alpha \tag{2.114}$$

where the prime denotes a post–collision quantity. Again, greek indices denote vector components with respect to a set of orthogonal coordinate axes. In addition to (2.114) we conserve linear momentum,

$$\mathbf{c}_1 + \mathbf{c}_2 = \mathbf{c}'_1 + \mathbf{c}'_2 \tag{2.115}$$

So we may write the post–collisional velocities as,

$$c'_{1\alpha} = c_{1\alpha} - g_\beta k_\beta k_\alpha \tag{2.116}$$

$$c'_{2\alpha} = c_{2\alpha} + g_\beta k_\beta k_\alpha \tag{2.117}$$

With a list of potential contacts generated by the searching algorithm, we calculate the distances between neighboring particle centers, d_c. If such a distance is less than the sum of the particle radii ($d_c < d$ for identical particles) we note this as a contact and calculate the relative velocity of the pair. Applying (2.116) and

(2.117) we resolve the post–collision velocities and place the particles tangent to each other by displacing each particle by half the initial particle overlap $d - d_c$, typically a small quantity with an appropriate time step. This placement is important for preventing a "rattling" contact. If the relative velocities of an overlapping pair are such that they would otherwise remain in contact at the next time step, they will oscillate repeatedly. The pair's relative velocity will reverse its sign in every subsequent time step and the particles will likely not separate. This has especially significant consequences for non–elastic interactions where energy loss through repeated collisions will cause rattling particles to converge to a single computational cell and generate an error in the simulation.

Since the collisions are instantaneous and we do not incorporate additional forces between interactions (such as gravity), we do not consider accelerations. Hence a particle with position $\mathbf{x}$ and velocity $\mathbf{v}$ at a particular time translates to $\mathbf{x}^+$ in time step Δt by,

$$\mathbf{x}^+ = \mathbf{x} + \mathbf{v}\Delta t \tag{2.118}$$

To calculate the granular temperature of particles in the simulation we recall its definition as the energy (per unit mass) of fluctuations about the mean speed. We denote the speed of the ith particle as c_i. In general, we may express this quantity as the sum of the mean speed $\overline{c}$ and a fluctuating contribution C_i,

$$c_i = \overline{c} + C_i \tag{2.119}$$

where $\overline{c} = (1/N) \sum_{i=1}^{N} c_i$.

Lacking other sources (such as through chemical reaction), the energy (E) of the flow is simply the sum of the particle's individual kinetic energies $\frac{1}{2} m_i c_i^2$ (no

summation). Thus we have,

$$E = \sum_{i=1}^{N} \frac{1}{2} m_i c_i^2 = \sum_{i=1}^{N} \frac{1}{2} m_i \left(\overline{c} + C_i\right)^2 \tag{2.120}$$

For identical particles $m_i = m$,

$$E = \frac{m}{2} \sum_{i=1}^{N} \left(\overline{c} + C_i\right)^2$$

which simplifies to,

$$E = \frac{mN\overline{c}^2}{2} + \frac{m}{2} \sum_{i=1}^{N} C_i^2$$

Note the final term may be expressed in terms of the variance of the speed distribution σ^2

$$E = \frac{mN\overline{c}^2}{2} + \frac{mN\sigma^2}{2}$$

and the specific energy of the ensemble is

$$\frac{E}{Nm} = \frac{\overline{c}^2 + \sigma^2}{2} \tag{2.121}$$

Recall from the first term of the energy transport equation (2.60) that the specific energy is the sum of the mean kinetic energy and ε, which is equivalent to the temperature (T). Thus,

$$T = \frac{\sigma^2}{2} \tag{2.122}$$

This specification of the temperature is consistent with that of the literature [8].

2.5.2 The subcritical wedge ($\theta \leq \theta_c$)

By examination of the streamlines in Figure 2.9 we confirm it is reasonable to assume that, on average, the flow turns to align with the body, yielding a flow turning angle equal to that of the wedge. In general, with known θ and upstream

conditions we obtain two solutions for β. As mentioned prior, we expect to observe the lesser of the two solutions corresponding to the weak shock. Since θ and the upstream quantities are fixed, the shock angle is also constant and hence we obtain a straight shock front. Additionally, the shock front is *attached* to the tip of the wedge, although this is not enforced by any analysis thus far. Figure 2.12 displays a snapshot of a discrete element simulation for a subcritical wedge.

In our simulations we fix upstream conditions and vary the wedge angle to approach θ_c, where we no longer obtain straight shocks. The transition for $\theta > \theta_c$ is addressed in Section 2.5.3. Simulations are performed for a duration such that the visible shock feature is steady in time. With a visual estimate for the location of the shocked region from snapshots like Figure 2.12, we are able to perform spatially–averaged calculations for the relevant pre and post–shock parameters V, T, and ν. These quantities are subsequently time–averaged to obtain our results. Plots of the time histories and their variance also provide crude confirmation of the steady state beyond visual inspection of simulation animations. In Figure 2.13 we plot the time history of the post–shock area fraction for a sampling duration of 2×10^4 time steps. For the pre–shock quantities, we average over the region of the simulation prior to the wedge ($x \leq W - L$ in Figure 2.11). By using animations and snapshots of the simulations we are able to estimate the inclination of the shock ($\tilde{\beta}$) by the fitting of straight lines to the images. Particles considered in the post–shock averaging must then satisfy the condition that $\hat{x} > 0$ and $y < \hat{x} \tan \tilde{\beta}$. Specification of a shock angle less than the estimate $\tilde{\beta}$ did not change the results of these average calculations. This is important since we wish to omit the transitional region, however small. Thus, knowledge of the shock's precise orientation is not necessary for our spatially averaging computations– we may choose conservative $\tilde{\beta}$

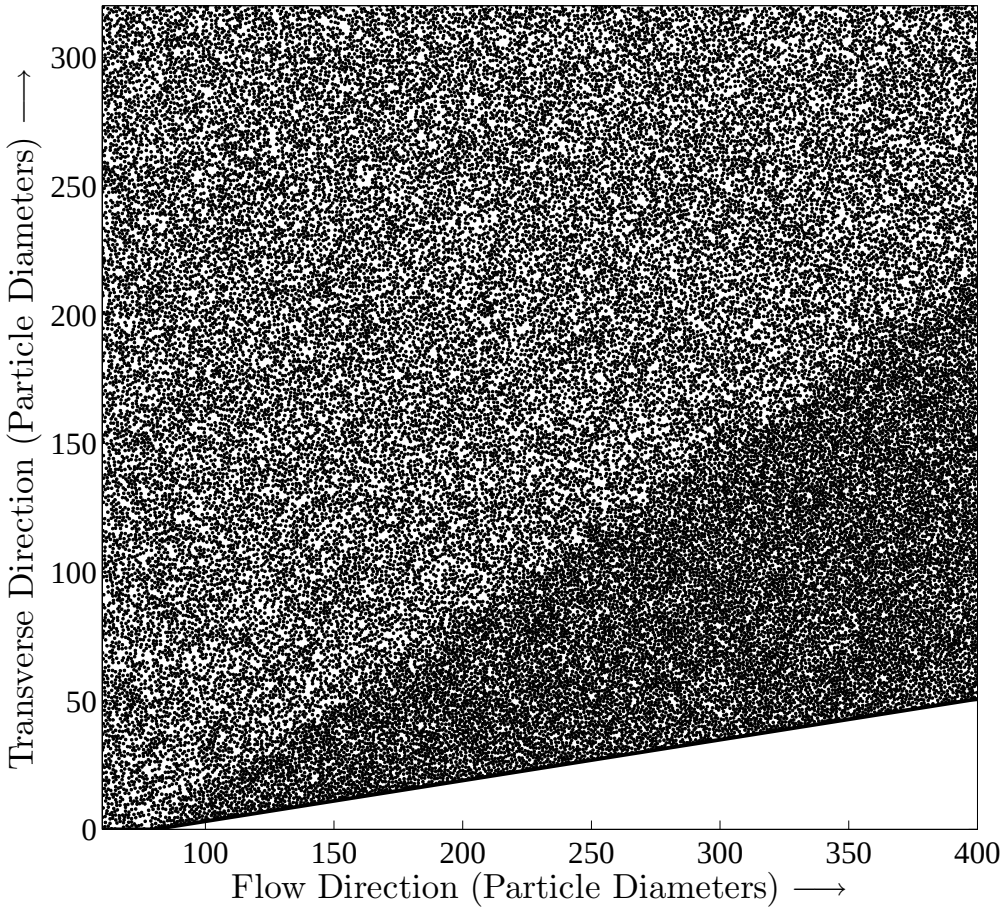

Figure 2.12: Simulation image for 9° wedge and upstream conditions $\Sigma = 2.26 \times 10^{-3}$ and $\nu_1 = 0.3$. Shock front is straight and attached at the wedge tip since $\theta \leq \theta_c$.

values with no effect on results.

Construction of β–θ curves such as in Figures 2.6 and 2.7 is a natural means of comparison based on the work in Section 2.4, but it is difficult to accurately and consistently quantify the shock angle. The shock transition is apparent in the images but the comparison to a line of known inclination is not well defined. Instead, we use the data obtained from our spatially and temporally averaged quantities to compare theory and simulation. Upstream values of the simulation closely correspond to those specified in the user–controlled input file, but we perform the calculations for confirmation. These values are subsequently used for initial conditions (subscripted "1") in the solution of the jump conditions. Roots of equation (2.95) are found with MATLAB's `fzero()` algorithm and the post–shock area fraction, temperature, and flow speed are determined.

In Figure 2.14 we plot the comparison of post–shock area fractions for both simulation and theory. In the simulations we specify upstream conditions of $T_1/V_1^2 \approx 4.44 \times 10^{-3}$, $\nu_1 = 0.3$, and vary the wedge inclination θ from 5° to 11° in half degree increments. Spatially and temporally averaged upstream quantities from the simulation are used as seed values to Equation (2.95). Post–shock mean area fractions from the simulations are plotted with error bars displaying one standard deviation in the data over the averaging time. Note that the average upstream quantities do not exactly correspond to those of the program input, but deviate about this mean. Hence the solutions to the discrete cases with varying upstream conditions lie about the solid curve corresonding to constant $T_1/V_1^2 = 4.44 \times 10^{-3}$ and $\nu_1 = 0.3$. We omit plots of the temperature (or equivalently pressure) and speed, but the agreement between the local analysis and simulation is similar to

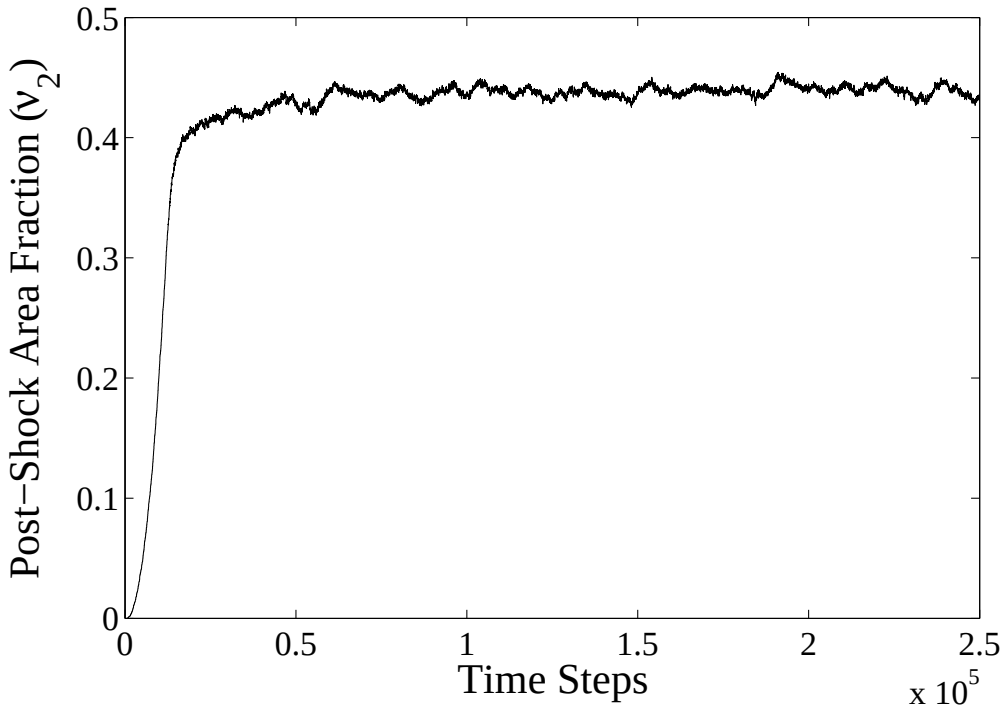

Figure 2.13: Time history of spatially averaged post–shock area fraction, ν_2.

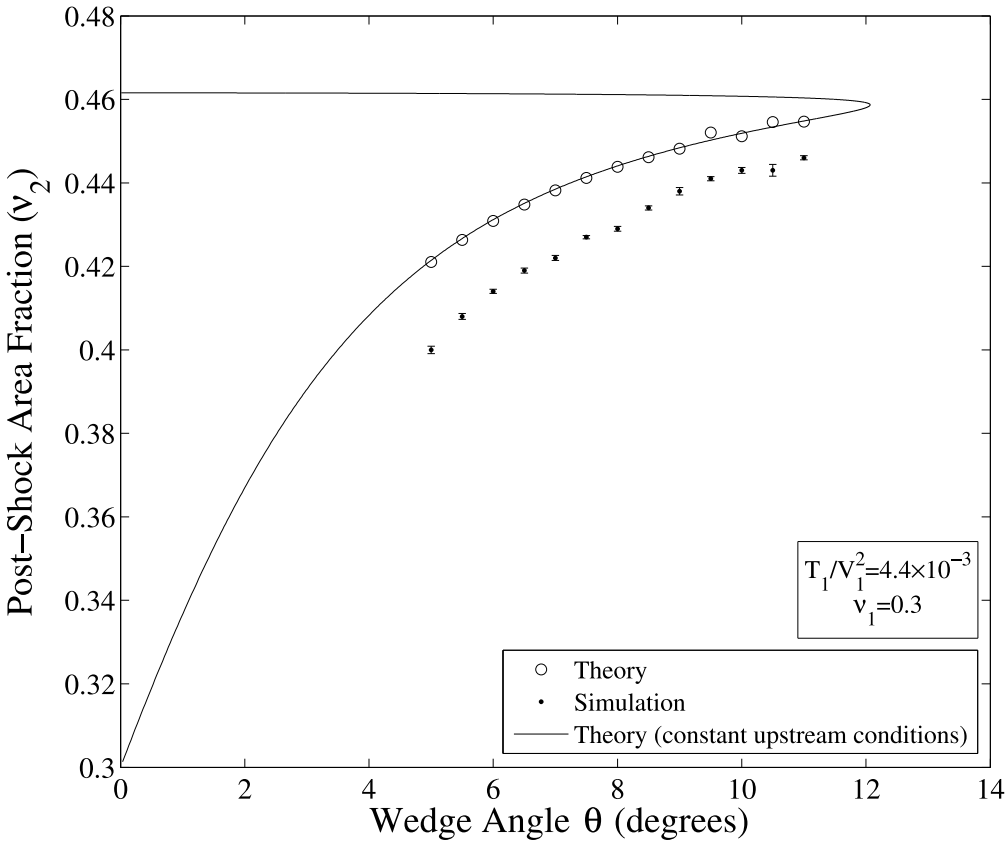

Figure 2.14: Comparison of post–shock area fraction between simulation and solution to (2.95) for average upstream conditions of $T_1/V_1^2 = 4.44\times10^{-3}$ and $\nu_1 = 0.3$. Error bars denote one standard deviation of the simulation data.

that of Figure 2.14. Relative error for all points is less than 5%.

It is of note that if we treat the granular temperature T as equivalent to the variance of the velocity distribution (not one–half its value as in (2.122)), we obtain better quantitative agreement between simulation and theory. Relative differences are less than 1% in this instance. This is confirmed in several comparisons between simulation and theory, but we are unsure of the reason for this.

2.5.3 The supercritical wedge ($\theta > \theta_c$)

By examination of Figures 2.6 and 2.7 we note that for given upstream conditions there exists a maximum flow turning angle θ_c, termed the critical angle. Flow passing through the shock discontinuity is limited to deflections in a range of $0 \leq \theta \leq \theta_c$. Physically, this imposes an upper limit on wedge inclinations where we expect to observe a straight shock. If a wedge of $\theta > \theta_c$ is prescribed, the flow cannot deflect further than θ_c and thus cannot align with the wedge. The important assumption of Section 2.5.2 connecting the jump conditions and wedge geometry was that the flow (on average) was turned by a constant angle θ everywhere over the wedge surface. Without knowledge of this constant θ value we no longer have the same solution to the jump conditions corresponding to the straight shock. The presence of a supercritical wedge does not, however, imply that flow passing through the shock surface will by default turn with deflection θ_c in an attempt to exceed this value. By inspection of (2.98) we see that it is possible to obtain imaginary solutions for β if the discriminant $(r-1)^2 - 4r\tan^2\theta < 0$, where r is the ratio of pre to post–shock densities. However, the existence of a shock surface inclined at a real value of β physically precludes the case of a negative discriminant. The local analysis remains valid, but is insufficient to determine the global position of the shock front. A condition of impermeability ($\mathbf{V} \cdot \hat{\mathbf{n}} = 0$) and the inability of the post–shock flow to immediately align with the wedge suggests a velocity gradient in the shock region that was not present for the subcritical wedge.

In simulations that approach the critical wedge angle, we begin to see curving of the shock front, as in Figure 2.15. The shock still appears attached to the tip of the wedge, or is minimally detached (on the order of several particle diameters). However, the supercritical wedge simulations display a significant qualitative change

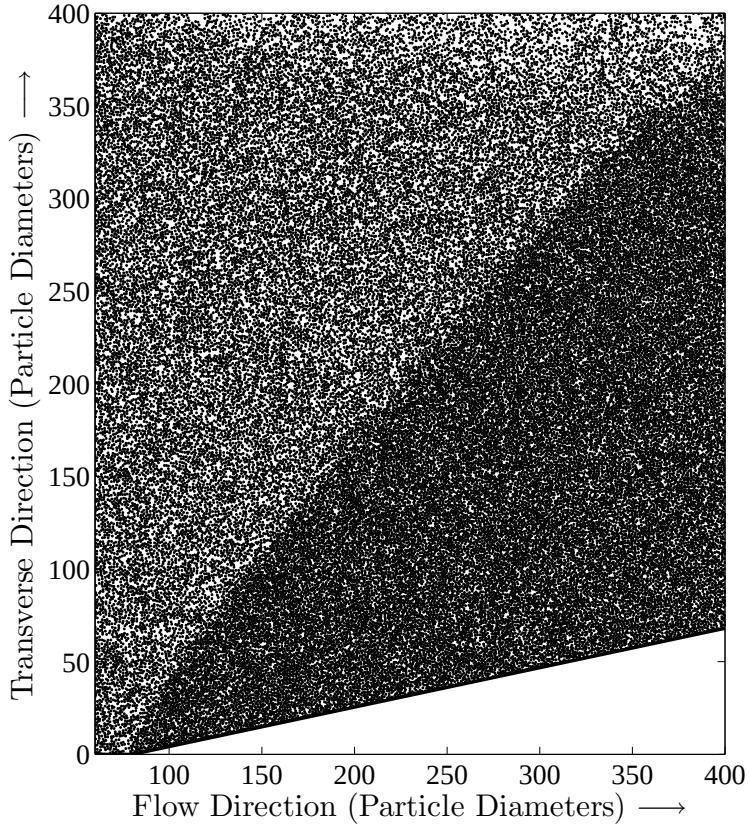

Figure 2.15: Shock about 12° wedge, displaying a curved shape as θ approaches θ_c. The shock front remains close to the wedge tip. Upstream conditions are $T_1/V_1^2 = 2.23 \times 10^{-3}$ and $\nu_1 = 0.3$

in the shock shape– we observe a detached "bow" shock. The upstream edge of the shock is noticeably displaced from the wedge tip and is oriented perpendicular to the incoming flow (a locally normal shock). Shock β values vary and our local analysis suggests that the flow turning angle accordingly differs since upstream conditions remain uniform. Figure 2.16 displays a simulation image for a wedge of 20° where $\theta_c \approx 12^\circ$ for the upstream flow conditions.

It is worth noting that we observe *strong* solution β values in the simulation images of the bow shock resulting from the supercritical wedge. From inspection of the $\beta-\theta$ curves and by the nature of roots to the quadratic shown in Equation (2.98), we see that for a given $\theta \neq \theta_c$, two real β values are possible. At the critical angle we only have one solution, β_c. For the subcritical wedge, we observed only the *weak* solutions where $\beta \leq \beta_c$. Over the entire bow shock (as in Figure 2.16) we see a range of β values that span both strong and weak shock solutions.

Bow shock displacement

Note that in the case of the subcritical wedge we were not supplied with a natural length scale in the continuum calculations. Without a body force we have only scales of speed, provided by the upstream flow and granular temperature. Accordingly, resulting shock features were not altered by the length of the wedge obstruction– shock fronts were straight and inclined at angle β regardless of wedge length L. However, for the detached bow shock we observe that detachment distance and the resulting shock vary depending upon L. The geometry of the wedge imposes a length scale on the size and shape of the resulting shock feature.

For supercritical wedges of angles 15° and 20° we vary L while maintaining upstream flow conditions of $\Sigma = 4.4 \times 10^{-3}$ and $\nu_1 = 0.3$. We plot the simulation images at steady state and obtain a visual estimate for the displacement of the

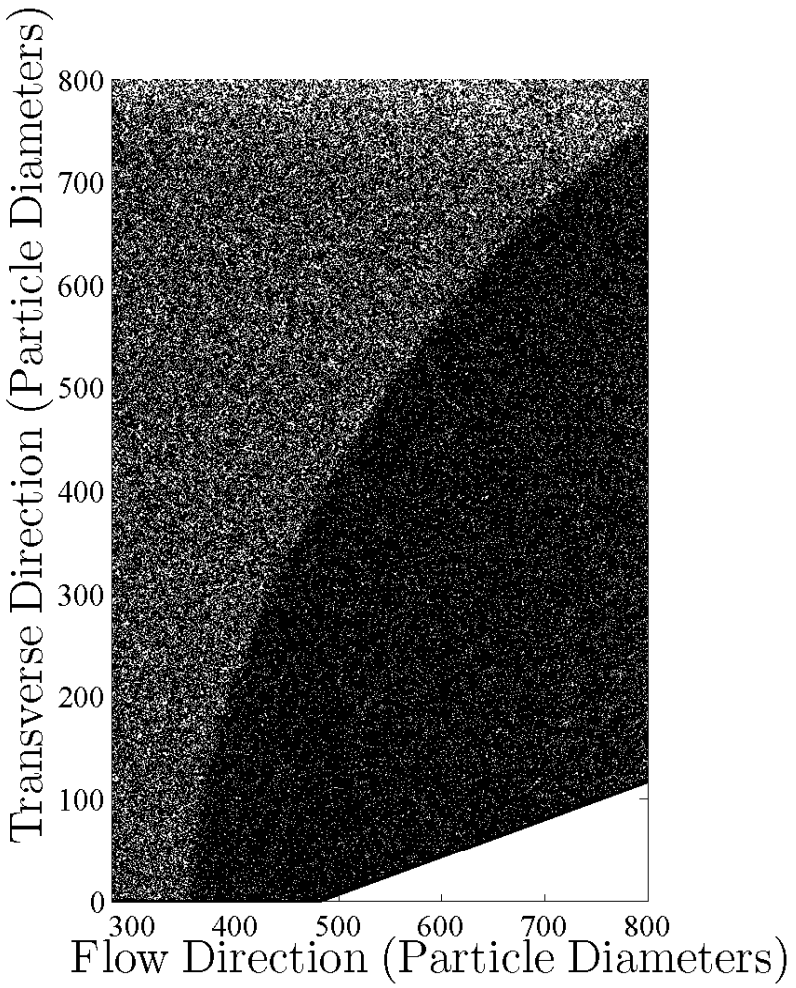

Figure 2.16: Bow shock for 20° wedge. Upstream conditions are $T_1/V_1^2 = 4.4 \times 10^{-3}$ and $\nu_1 = 0.3$

bow shock from the wedge tip. We plot the relationship between L and offset in Figure 2.17.

We see that for a prescribed wedge inclination, the shock offset is linearly dependent on the wedge length L. Scaling by the wedge opening $h_r = L \tan\theta$ does not reduce the data to a single curve, so offset distance is not linearly related to this measure. Investigation of this non–linear dependence warrants further investigation; analysis contained in this thesis does not provide evidence for the scaling.

2.6 Conclusions

In this chapter relations were derived to relate flow quantities across oblique granular shocks. These four algebraic equations were found to be in good quantitative agreement with the results of numerical simulations, with relative errors of $\sim 3\%$ on average. A perfect gas approximation is made in the dilute limit of the equations. Improved agreement with simulations might be obtained as the ratio of particle to system size decreases and the continuum approximation improves. Additional improvements might be obtained with an equation of state that is improved for the area fractions of interest. These remain open to investigation.

The shock relations were also accurate with simulations in the prediction of the critical wedge angle θ_c where shock detachment begins. The change in shock behavior resulting from detachment is significant, so the ability to model its occurrence is important. We examined supercritical wedges and found that bow shock detachment is linearly related to wedge length at a single angle θ. However, further analysis is necessary to determine the non–linear relationship between shock detachment, wedge height, and wedge inclination.

Our estimate for the sound speed derived from equilibrium thermodynamic

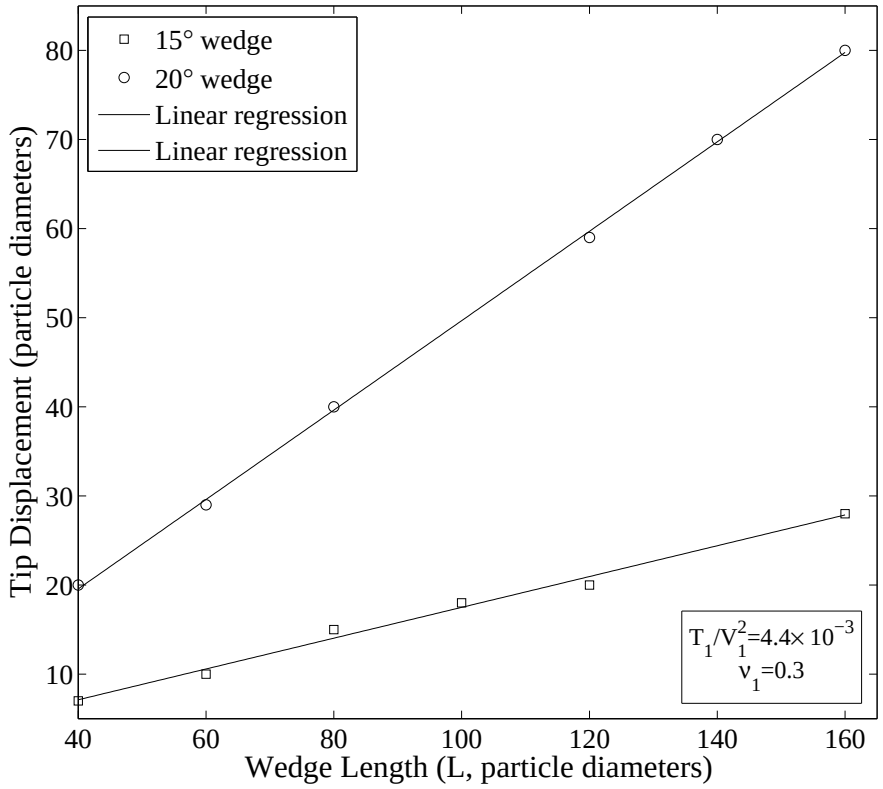

Figure 2.17: Bow shock offset for varied wedge length L for 20° and 15° wedges. Lines are linear least–square fits of the data. Upstream conditions are $T_1/V_1^2 = 4.4 \times 10^{-3}$ and $\nu_1 = 0.3$

analysis remains to be verified but we note that for simulations where upstream Σ and ν_1 are such that they approach $\mathfrak{a}$, resulting shock features are weak or do not exist. Significantly more particles exit the simulation domain on the upstream side, indicating that information about the obstructing wedge is propagating upstream. Particles become aware of the body and a shock does not develop. This suggests that the sound speed model is approximately valid, but more concrete evidence is needed to demonstrate this.

We finally note that the shock jump conditions are only locally valid and are unable to provide global information regarding shape or other attributes of the detached bow shock. Simulations indicate that the shock detachment distance is related to length scales in the wedge geometry. This motivates our work in Chapter 3.

CHAPTER 3

BALANCE RELATIONS FOR SHOCKED GRANULAR FLOW

3.1 Depth–averaged Relations

Consider a granular flow of known properties incident on a physical body of specified shape. Assuming initially supersonic flow and the presence of a shock, we look to determine post–shock flow properties and the shape of the shock front. In the study of compressible gases, systems of partial differential equations in the flow–field variables are often numerically solved using finite difference methods or the method of characteristics [2, 5]. Here we derive a system of four equations to determine the shock location (δ), and shock depth–averaged quantities: area fraction ($\overline{\nu}$), velocity ($\overline{u}, \overline{v}$), and pressure ($\overline{p}$) (or equivalently temperature, $\overline{T}$). Note that there are five scalar unknown functions in four equations, and simplifying assumptions are necessary to solve the system of ordinary differential equations.

In the derivations to follow, we choose an orthogonal body–oriented coordinate system (ξ, η) where the ξ–direction is tangent to the body, as shown in Figure 3.1. The local body orientation is θ and the shock angle is β, both measured with respect to the horizontal. We average the desired quantities in the η–direction, leaving body–tangent flow speed $\overline{u}(\xi)$, body–normal flow speed $\overline{v}(\xi)$, $\overline{p}(\xi)$, $\overline{\nu}(\xi)$, and $\delta(\xi)$.

As with the shock jump conditions derived in Chapter 2, known upstream (pre–shock) quantities are denoted with the subscript 1 and immediately post–shock quantities are denoted with the subscript 2. We assume horizontal incoming flow of speed V_1 and admit the possibility of velocity gradients for the case of shear

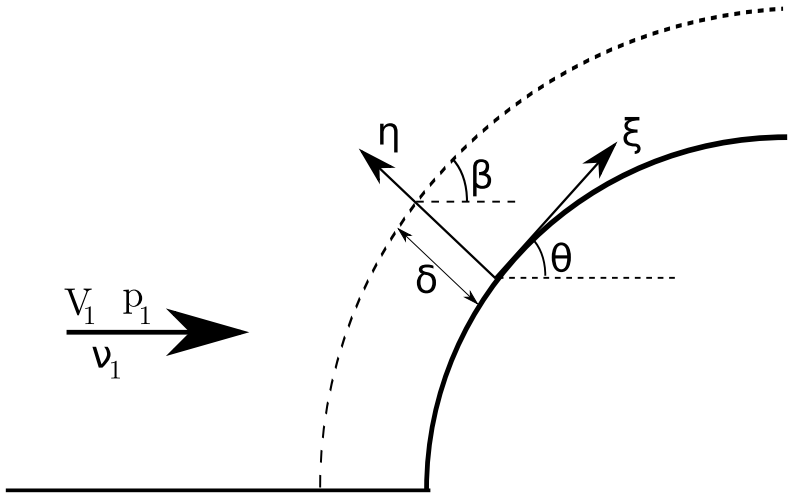

Figure 3.1: Geometry of the flow field. Known upstream parameters are denoted with 1 subscripts. The shock front is represented by a dotted line.

flow, where one may specify $V_1(\xi)$.

3.1.1 Continuity

We start with the general continuity equation,

$$\frac{\partial \rho}{\partial t} + \nabla \cdot (\rho \mathbf{u}) = 0 \tag{3.1}$$

For steady flow, we write this in terms of the body–oriented coordinate system (ξ, η),

$$\frac{\partial}{\partial \xi}(\rho u) + \frac{\partial}{\partial \eta}(\rho v) = 0 \tag{3.2}$$

where again, u is the flow speed in the ξ–direction, and v is the speed n the η–direction. We integrate this expression over the local shock–thickness $\delta(\xi)$,

$$\int_0^\delta \frac{\partial}{\partial \xi}(\rho u) d\eta + \int_0^\delta \frac{\partial}{\partial \eta}(\rho v) d\eta = 0 \tag{3.3}$$

which leads to,

$$\int_0^{\delta} \frac{\partial}{\partial \xi}(\rho u)d\eta + \rho v\Big|_{\eta=0}^{\eta=\delta} = 0 \tag{3.4}$$

The first integral can be handled using the Leibniz integral rule,

$$\frac{\partial}{\partial z}\int_{a(z)}^{b(z)} f(x,z)dx = \int_{a(z)}^{b(z)} \frac{\partial f}{\partial z}dx + f(b(z),z)\frac{db}{dz} - f(a(z),z)\frac{da}{dz} \tag{3.5}$$

which is applied to (3.4) to obtain,

$$\frac{\partial}{\partial \xi}\int_0^{\delta}(\rho u)d\eta - \frac{d\delta}{d\xi}(\rho u)\Big|_{\eta=\delta} + \rho v\Big|_{\eta=0}^{\eta=\delta} = 0 \tag{3.6}$$

The bottom boundary ($\eta = 0$) is the physical body, so an impermeability condition is applied. Thus, $v(\eta = 0) = 0$,

$$\frac{\partial}{\partial \xi}\int_0^{\delta}(\rho u)d\eta - \left[\frac{d\delta}{d\xi}\rho u - \rho v\right]_{\eta=\delta} = 0$$

$$\frac{\partial}{\partial \xi}\int_0^{\delta}(\rho u)d\eta - \rho_s\left(\frac{d\delta}{d\xi}u_s - v_s\right) = 0 \tag{3.7}$$

Note that (3.7) evaluates the density and velocity immediately behind the shock surface, $\eta = \delta$, which we denote with subscript "s" quantities. The density evaluated at the shock surface is simply the post–shock density, $\rho_s = \rho_2$. For u_s and v_s, we require a transformation to express these speeds in terms of speeds subscripted with "2" from the jump conditions of Chapter 2. Recall that in phrasing the jump conditions, we adopted u_2 and w_2 as the post–shock velocity components normal and tangential to the shock, respectively. We are looking for the post–shock velocity normal and parallel to the *physical body*, so we project each of these components into the appropriate directions,

$$u_s \equiv u(\xi, \eta = \delta) = u_2 \sin(\beta - \theta) + w_2 \cos(\beta - \theta) \tag{3.8}$$

$$v_s \equiv v(\xi, \eta = \delta) = -u_2 \cos(\beta - \theta) + w_2 \sin(\beta - \theta) \tag{3.9}$$

Note that we are *not* assuming any direction of the post–shock flow as in the case of the jump conditions of Chapter 2. In the local analysis performed there, we were limited to flows and geometries such that flow alignment with the wedge was a reasonable assumption ($\theta \leq \theta_c$). By the geometry of Figure 3.1,

$$\frac{d\delta}{d\xi} = \tan(\beta - \theta) \tag{3.10}$$

and using equations (3.8) and (3.9) the quantity $(d\delta/d\xi)u_s - v_s$ from Equation (3.7) becomes,

$$\frac{d\delta}{d\xi}u_s - v_s = \tan(\beta-\theta)\left[u_2\sin(\beta-\theta) + w_2\cos(\beta-\theta)\right] + \left[u_2\cos(\beta-\theta) - w_2\sin(\beta-\theta)\right]$$

$$\frac{d\delta}{d\xi}u_s - v_s = \frac{u_2\sin^2(\beta-\theta)}{\cos(\beta-\theta)} + u_2\cos(\beta-\theta)$$

$$\frac{d\delta}{d\xi}u_s - v_s = \frac{u_2}{\cos(\beta-\theta)} \tag{3.11}$$

The continuity expression (3.7) now simplifies to,

$$\frac{\partial}{\partial\xi}\int_0^\delta (\rho u)d\eta = \frac{\rho_2 u_2}{\cos(\beta-\theta)} \tag{3.12}$$

We recall the continuity jump condition Equation (2.75),

$$\rho_1 u_1 = \rho_1 V_1 \sin\beta = \rho_2 u_2 \tag{3.13}$$

and we obtain,

$$\frac{\partial}{\partial\xi}\int_0^\delta (\rho u)d\eta = \frac{\rho_1 V_1\sin\beta}{\cos(\beta-\theta)} \tag{3.14}$$

If we regard $(\rho u) = (\overline{\rho u})$ as depth–averaged quantities, we can remove it from the integral to obtain,

$$\frac{\partial}{\partial\xi}(\overline{\rho u}\delta) = \frac{\rho_1 V_1\sin\beta}{\cos(\beta-\theta)} \tag{3.15}$$

We now divide out the constituent material density (ρ_m) to express in terms of the area fraction ν,

$$\frac{\partial}{\partial \xi}(\overline{\nu u}\delta) = \frac{\nu_1 V_1 \sin\beta}{\cos(\beta - \theta)} \tag{3.16}$$

Finally, we seek to remove the explicit β dependence in favor of $d\delta/d\xi$. Using Equation (3.10) with the trigonometric identity,

$$\tan(\beta - \theta) = \frac{\tan\beta - \tan\theta}{1 + \tan\beta\tan\theta} \tag{3.17}$$

we are able to solve for $\tan\beta$,

$$\tan\beta = \frac{\delta' + \tan\theta}{1 - \delta'\tan\theta} \equiv \psi \tag{3.18}$$

where the prime denotes a derivative with respect to the ξ–coordinate. Then,

$$\beta = \tan^{-1}(\psi) \tag{3.19}$$

and,

$$\sin\beta = \sin\left(\tan^{-1}(\psi)\right) = \frac{\psi}{\sqrt{1+\psi^2}} = \frac{\delta'\cos\theta + \sin\theta}{\sqrt{1+\delta'^2}} \tag{3.20}$$

$$\cos\beta = \cos\left(\tan^{-1}(\psi)\right) = \frac{1}{\sqrt{1+\psi^2}} = \frac{\cos\theta - \delta'\sin\theta}{\sqrt{1+\delta'^2}} \tag{3.21}$$

Thus,

$$\frac{\sin\beta}{\cos(\beta-\theta)} = \frac{\sin\beta}{\cos\beta\cos\theta + \sin\beta\sin\theta} = \delta'\cos\theta + \sin\theta \tag{3.22}$$

and Equation (3.16) becomes,

$$\frac{\partial}{\partial \xi}(\overline{\nu u}\delta) = \nu_1 V_1(\delta'\cos\theta + \sin\theta) \tag{3.23}$$

3.1.2 Momentum– ξ direction

We start with a general form of the momentum equation,

$$\frac{\partial \tau_{ij}}{\partial x_i} + \rho b_j = \rho\frac{\partial v_j}{\partial t} + \rho v_i\frac{\partial v_j}{\partial x_i} \tag{3.24}$$

where $\mathbf{b}$ is the body force per unit mass. For steady flow in the ξ–direction,

$$\frac{\partial \tau_{\xi\xi}}{\partial \xi} + \frac{\partial \tau_{\eta\xi}}{\partial \eta} + \rho b_\xi = \rho v \frac{\partial u}{\partial \eta} + \rho u \frac{\partial u}{\partial \xi} \tag{3.25}$$

To this equation, we add ξ–direction speed u multiplied by the steady continuity equation (3.2),

$$\frac{\partial \tau_{\xi\xi}}{\partial \xi} + \frac{\partial \tau_{\eta\xi}}{\partial \eta} + \rho b_\xi = \rho v \frac{\partial u}{\partial \eta} + \rho u \frac{\partial u}{\partial \xi} + u \left[\frac{\partial}{\partial \xi}(\rho u) + \frac{\partial}{\partial \eta}(\rho v) \right]$$

$$\frac{\partial \tau_{\xi\xi}}{\partial \xi} + \frac{\partial \tau_{\eta\xi}}{\partial \eta} + \rho b_\xi = \rho v \frac{\partial u}{\partial \eta} + \rho u \frac{\partial u}{\partial \xi} + u \left[\rho \frac{\partial u}{\partial \xi} + \rho \frac{\partial v}{\partial \eta} + u \frac{\partial \rho}{\partial \xi} + v \frac{\partial \rho}{\partial \eta} \right]$$

$$\frac{\partial \tau_{\xi\xi}}{\partial \xi} + \frac{\partial \tau_{\eta\xi}}{\partial \eta} + \rho b_\xi = \rho v \frac{\partial u}{\partial \eta} + 2\rho u \frac{\partial u}{\partial \xi} + \rho u \frac{\partial v}{\partial \eta} + u^2 \frac{\partial \rho}{\partial \xi} + uv \frac{\partial \rho}{\partial \eta}$$

$$\frac{\partial \tau_{\xi\xi}}{\partial \xi} + \frac{\partial \tau_{\eta\xi}}{\partial \eta} + \rho b_\xi = \frac{\partial}{\partial \xi}\left(\rho u^2\right) + \frac{\partial}{\partial \eta}\left(\rho u v\right) \tag{3.26}$$

If we assume inviscid flow, the shear stress is absent, and we denote the isotropic stress tensor as $\tau = -p\mathbf{I}$, where $\mathbf{I}$ is the unit tensor. We depth–average over the shock thickness δ,

$$-\int_0^\delta \frac{\partial p}{\partial \xi} d\eta + \int_0^\delta \rho b_\xi d\eta = \int_0^\delta \frac{\partial}{\partial \xi}\left(\rho u^2\right) d\eta + \int_0^\delta \frac{\partial}{\partial \eta}\left(\rho u v\right) d\eta \tag{3.27}$$

Using Leibniz's rule and denoting the body force integral as $\mathbb{J}_1$,

$$-\frac{\partial}{\partial \xi}\int_0^\delta p d\eta + \frac{d\delta}{d\xi} p\Big|_{\eta=\delta} + \mathbb{J}_1 = \frac{\partial}{\partial \xi}\int_0^\delta \rho u^2 d\eta - \frac{d\delta}{d\xi}\rho u^2\Big|_{\eta=\delta} + \rho u v\Big|_0^\delta \tag{3.28}$$

Denoting depth–averaged quantities with overbars, and with the impermeable condition that $v(\eta = 0) = 0$,

$$-\frac{\partial}{\partial \xi}(\overline{p}\delta) + \frac{d\delta}{d\xi} p_s + \mathbb{J}_1 = \frac{\partial}{\partial \xi}\left(\delta\overline{\rho u^2}\right) - \frac{d\delta}{d\xi}\rho_s u_s^2 + \rho_s u_s v_s \tag{3.29}$$

Rearrange,

$$\frac{\partial \delta}{\partial \xi}\left(p_s + \rho_s u_s^2\right) - \rho_s u_s v_s + \mathbb{J}_1 = \frac{\partial}{\partial \xi}\left(\delta\overline{\rho u^2} + \overline{p}\delta\right) \tag{3.30}$$

The pressure at the shock is equivalent to p_2, the post–shock pressure that we obtain from the jump conditions of Chapter 2. We use equations (3.8) and (3.9) to express u_s and v_s in terms of the post–shock quantities. Along with jump conditions (2.75) and (2.77), we have a momentum jump condition Equation (2.76),

$$p_1 + \rho_1 u_1^2 = p_2 + \rho_2 u_2^2 \tag{3.31}$$

We evaluate the term $\delta'\left(p_s + \rho_s u_s^2\right) - \rho_s u_s v_s$ of (3.30), denoting $\phi \equiv \beta - \theta$ for convenience, and substituting for u_s and v_s,

$$\delta'\left[p_2 + \rho_2\left(u_2 \sin\phi + w_2 \cos\phi\right)^2\right]$$
$$-\rho_2\left[u_2 \sin\phi + w_2 \cos\phi\right]\left[-u_2 \cos\phi + w_2 \sin\phi\right]$$

expand,

$$\delta'\left[p_2 + \rho_2\left(u_2^2 \sin^2\phi + 2u_2 w_2 \sin\phi\cos\phi + w_2^2 \cos^2\phi\right)\right]$$
$$-\rho_2\left[-u_2^2 \sin\phi\cos\phi + w_2^2 \sin\phi\cos\phi - u_2 w_2 \cos^2\phi + u_2 w_2 \sin^2\phi\right]$$

Solve (3.31) for p_2,

$$\delta'(p_1 + \rho_1 u_1^2 - \rho_2 u_2^2) + \delta'\rho_2\left(u_2^2 \sin^2\phi + 2u_2 w_2 \sin\phi\cos\phi + w_2^2 \cos^2\phi\right)$$
$$-\rho_2\left[-u_2^2 \sin\phi\cos\phi + w_2^2 \sin\phi\cos\phi - u_2 w_2 \cos^2\phi + u_2 w_2 \sin^2\phi\right]$$

Employ relation (3.10) and simplify to,

$$\delta'(p_1 + \rho_1 u_1^2) + \rho_2 u_2 w_2$$

With (3.13), and (2.77) preserving the velocity component tangential to the shock,

$$\delta'(p_1 + \rho_1 u_1^2) + \rho_1 u_1 w_1$$

$$\delta'(p_1 + \rho_1 V_1^2 \sin^2\beta) + \rho_1 V_1^2 \sin\beta\cos\beta$$

$$\delta' p_1 + \rho_m \nu_1 V_1^2 \left(\sin\beta\cos\beta + \delta'\sin^2\beta\right) \tag{3.32}$$

With this substitution, Equation (3.30) becomes,

$$-\rho_m \frac{\partial}{\partial \xi}\left(\overline{\nu u^2}\delta + \frac{\overline{p}\delta}{\rho_m}\right) + \rho_m \nu_1 V_1^2 \left(\sin\beta\cos\beta + \delta'\sin^2\beta\right) + p_1\delta' + \mathbb{J}_1 = 0$$

We look to simplify the $\sin\beta\cos\beta + \delta'\sin^2\beta$ term to replace β in favor of δ'. From Equations (3.19)–(3.21),

$$\sin\beta\cos\beta + \delta'\sin^2\beta = \frac{\psi}{1+\psi^2} + \delta'\frac{\psi^2}{1+\psi^2} = \frac{\psi + \delta'\psi^2}{1+\psi^2} \tag{3.33}$$

After some simplification this gives,

$$\sin\beta\cos\beta + \delta'\sin^2\beta = \cos^2\theta(\delta' + \tan\theta) \tag{3.34}$$

Our ξ–momentum balance is now

$$-\rho_m \frac{\partial}{\partial \xi}\left(\overline{\nu u^2}\delta + \frac{\overline{p}\delta}{\rho_m}\right) + \rho_m \nu_1 V_1^2 \cos^2\theta(\delta' + \tan\theta) + p_1\delta' + \mathbb{J}_1 = 0 \tag{3.35}$$

which we can rewrite as,

$$\rho_m \frac{\partial}{\partial \xi}\left(\overline{\nu u^2}\delta + \frac{\overline{p}\delta}{\rho_m}\right) - (\rho_m \nu_1 V_1^2 \cos^2\theta + p_1)\frac{d\delta}{d\xi} - \mathbb{J}_1 = \rho_m \nu_1 V_1^2 \sin\theta\cos\theta \tag{3.36}$$

If we neglect the body force term,

$$\rho_m \frac{\partial}{\partial \xi}\left(\overline{\nu u^2}\delta + \frac{\overline{p}\delta}{\rho_m}\right) - (\rho_m \nu_1 V_1^2 \cos^2\theta + p_1)\frac{d\delta}{d\xi} = \rho_m \nu_1 V_1^2 \sin\theta\cos\theta \tag{3.37}$$

3.1.3 Momentum– η direction

Again, we start with the general form of the momentum equation,

$$\frac{\partial \tau_{ij}}{\partial x_i} + \rho b_j = \rho\frac{\partial v_j}{\partial t} + \rho v_i \frac{\partial v_j}{\partial x_i} \tag{3.38}$$

For steady flow in the η–direction,

$$\frac{\partial \tau_{\xi\eta}}{\partial \xi} + \frac{\partial \tau_{\eta\eta}}{\partial \eta} + \rho b_\eta = \rho v\frac{\partial v}{\partial \eta} + \rho u\frac{\partial v}{\partial \xi} \tag{3.39}$$

To this we add v multiplied by the steady continuity equation (3.2),

$$\frac{\partial \tau_{\xi\eta}}{\partial \xi} + \frac{\partial \tau_{\eta\eta}}{\partial \eta} + \rho b_\eta = \rho v \frac{\partial v}{\partial \eta} + \rho u \frac{\partial v}{\partial \xi} + v \left[\frac{\partial}{\partial \xi}(\rho u) + \frac{\partial}{\partial \eta}(\rho v) \right]$$

$$\frac{\partial \tau_{\xi\eta}}{\partial \xi} + \frac{\partial \tau_{\eta\eta}}{\partial \eta} + \rho b_\eta = \rho v \frac{\partial v}{\partial \eta} + \rho u \frac{\partial v}{\partial \xi} + v \left[\rho \frac{\partial u}{\partial \xi} + \rho \frac{\partial v}{\partial \eta} + u \frac{\partial \rho}{\partial \xi} + v \frac{\partial \rho}{\partial \eta} \right]$$

$$\frac{\partial \tau_{\xi\eta}}{\partial \xi} + \frac{\partial \tau_{\eta\eta}}{\partial \eta} + \rho b_\eta = 2\rho v \frac{\partial v}{\partial \eta} + \rho u \frac{\partial v}{\partial \xi} + \rho v \frac{\partial u}{\partial \xi} + uv \frac{\partial \rho}{\partial \xi} + v^2 \frac{\partial \rho}{\partial \eta}$$

$$\frac{\partial \tau_{\xi\eta}}{\partial \xi} + \frac{\partial \tau_{\eta\eta}}{\partial \eta} + \rho b_\eta = \frac{\partial}{\partial \eta}\left(\rho v^2\right) + \frac{\partial}{\partial \xi}\left(\rho u v\right) \tag{3.40}$$

Again assuming inviscid flow and averaging over the shock thickness,

$$-\int_0^\delta \frac{\partial p}{\partial \eta} d\eta + \int_0^\delta \rho b_\eta d\eta = \int_0^\delta \frac{\partial}{\partial \eta}\left(\rho v^2\right) d\eta + \int_0^\delta \frac{\partial}{\partial \xi}\left(\rho u v\right) d\eta$$

Denote the body force integral in the η–direction as $\mathbb{J}_2$ and re–state some of the terms,

$$-\Big[p(\eta = \delta) - p(\eta = 0)\Big] + \mathbb{J}_2 = \Big[\rho v^2\Big]_0^\delta + \int_0^\delta \frac{\partial}{\partial \xi}\left(\rho u v\right) d\eta \tag{3.41}$$

At the body we denote the pressure $p(\eta = 0)$ as p_b and we enfoce the impermeability of the body, $v(\eta = 0) = 0$. We apply Leibniz's rule to the final integral on the right hand side,

$$p_b - p_s + \mathbb{J}_2 = \rho_s v_s^2 + \frac{\partial}{\partial \xi}(\delta \overline{\rho u v}) - \frac{d\delta}{d\xi} \rho u v \Big|_{\eta = \delta} \tag{3.42}$$

Rearrange,

$$p_b + \mathbb{J}_2 = \frac{\partial}{\partial \xi}(\delta \overline{\rho u v}) + p_s + \rho_s v_s^2 - \frac{d\delta}{d\xi} \rho_s u_s v_s \tag{3.43}$$

Using the jump conditions, $\rho_s = \rho_2$, and $p_s = p_2$ we evaluate $p_s + \rho_s v_s^2 - \delta' \rho_s u_s v_s$. For convenience we again denote $\phi \equiv \beta - \theta$,

$$p_s + \rho_s v_s^2 - \frac{d\delta}{d\xi} \rho_s u_s v_s$$

$$p_2 + \rho_2 \left[-u_2 \cos\phi + w_2 \sin\phi\right]^2 - \rho_2 \tan\phi \left[u_2 \sin\phi + w_2 \cos\phi\right] \left[-u_2 \cos\phi + w_2 \sin\phi\right]$$

After some simplification, this yields

$$p_1 + \rho_1 u_1^2 - \rho_2 u_2 w_2 \tan\phi$$

which is equivalent to,

$$p_1 + \rho_1 u_1^2 - \rho_1 u_1 w_1 \delta'$$

$$p_1 + \rho_1 V_1^2 \sin^2\beta - \rho_1 V_1^2 \delta' \sin\beta\cos\beta$$

$$p_1 + \rho_m \nu_1 V_1^2 \sin\beta\cos\beta(\tan\beta - \delta') \tag{3.44}$$

Thus our η–direction momentum equation becomes

$$\frac{\partial}{\partial\xi}(\delta\overline{\rho u v}) + p_1 + \rho_m \nu_1 V_1^2 \sin\beta\cos\beta(\tan\beta - \delta') - \mathbb{J}_2 - p_b = 0 \tag{3.45}$$

We look to phrase $\sin\beta\cos\beta(\tan\beta - \delta')$ in favor of $d\delta/d\xi$ and θ. Employing (3.20) and (3.21)

$$\sin\beta\cos\beta(\tan\beta - \delta') = \left[\frac{\psi}{\sqrt{1+\psi^2}}\right]\left[\frac{1}{\sqrt{1+\psi^2}}\right](\psi - \delta')$$

$$\sin\beta\cos\beta(\tan\beta - \delta') = \left[\frac{\psi}{1+\psi^2}\right](\psi - \delta')$$

which simplifies to,

$$\sin\beta\cos\beta(\tan\beta - \delta') = \delta' \sin\theta\cos\theta + \sin^2\theta$$

and our momentum balance (3.45) is,

$$\rho_m \frac{\partial}{\partial\xi}(\delta\overline{\nu u v}) + p_1 + \rho_m \nu_1 V_1^2(\delta' \sin\theta\cos\theta + \sin^2\theta) - \mathbb{J}_2 - p_b = 0 \tag{3.46}$$

If we neglect the body force integral,

$$\rho_m \frac{\partial}{\partial\xi}(\delta\overline{\nu u v}) + p_1 + \rho_m \nu_1 V_1^2(\delta' \sin\theta\cos\theta + \sin^2\theta) - p_b = 0 \tag{3.47}$$

3.1.4 Energy

From Section 2.3.4 we start with the general energy equation (2.60),

$$\frac{D}{Dt}\int\limits_{\mathbb{V}(t)} \rho\left(\frac{1}{2}u_\alpha u_\alpha + \varepsilon\right) dV = \int\limits_{\mathbb{V}(t)} \rho(b_\alpha u_\alpha + c_1)dV + \\ + \int\limits_{\mathbb{A}(t)} (\tau_{\alpha\beta}u_\alpha - q_\beta + c_2)dA_\beta \tag{3.48}$$

Preserving only body force and stress–production terms we have,

$$\frac{D}{Dt}\int\limits_{\mathbb{V}(t)} \rho\left(\frac{1}{2}u_\alpha u_\alpha + \varepsilon\right) dV = \int\limits_{\mathbb{V}(t)} \rho b_\alpha u_\alpha dV + \int\limits_{\mathbb{A}(t)} \tau_{\alpha\beta}u_\alpha dA_\beta \tag{3.49}$$

Using Equation (2.37) we bring the material derivative inside the integral,

$$\int\limits_{\mathbb{V}(t)} \rho\frac{D}{Dt}\left(\frac{1}{2}u_\alpha u_\alpha + \varepsilon\right) dV = \int\limits_{\mathbb{V}(t)} \rho b_\alpha u_\alpha dV + \int\limits_{\mathbb{A}(t)} \tau_{\alpha\beta}u_\alpha dA_\beta \tag{3.50}$$

With the Divergence Theorem we transform the surface integral of stress–production to a volume integration,

$$\int\limits_{\mathbb{V}(t)} \rho\frac{D}{Dt}\left(\frac{1}{2}u_\alpha u_\alpha + \varepsilon\right) dV = \int\limits_{\mathbb{V}(t)} \rho b_\alpha u_\alpha dV + \int\limits_{\mathbb{V}(t)} \frac{\partial(\tau_{\alpha\beta}u_\alpha)}{\partial x_\beta} dV \tag{3.51}$$

In general we consider an arbitrary volume of integration, and thus we are required to satisfy,

$$\rho\frac{D}{Dt}\left(\frac{1}{2}u_\alpha u_\alpha + \varepsilon\right) - \rho b_\alpha u_\alpha - \frac{\partial(\tau_{\alpha\beta}u_\alpha)}{\partial x_\beta} = 0 \tag{3.52}$$

As with our continuity and momentum expressions, we seek to depth–average this relation. In a similar fashion, we manipulate this equation to phrase in a more convenient form. To begin, we set the velocity fluctuation energy (ε) equal to the temperature T and distribute the material derivative $D/Dt = \partial/\partial t + u_\alpha \partial/\partial x_\alpha$,

$$\rho\left[u_\beta\frac{\partial}{\partial x_\beta}\left(\frac{1}{2}u_\alpha u_\alpha\right) + u_\beta\frac{\partial T}{\partial x_\beta}\right] - \rho b_\alpha u_\alpha - \frac{\partial(\tau_{\alpha\beta}u_\alpha)}{\partial x_\beta} = 0 \tag{3.53}$$

where we have enforced the steady state $\partial/\partial t = 0$. Next we apply our inviscid stress tensor $\tau = -p\mathbf{I}$

$$\rho\left[u_\beta\frac{\partial}{\partial x_\beta}\left(\frac{1}{2}u_\alpha u_\alpha\right)+u_\beta\frac{\partial T}{\partial x_\beta}\right]-\rho b_\alpha u_\alpha+\frac{\partial(pu_\beta)}{\partial x_\beta}=0 \tag{3.54}$$

We now write out each component,

$$\rho\left[\frac{u}{2}\frac{\partial}{\partial\xi}\left(u^2+v^2\right)+\frac{v}{2}\frac{\partial}{\partial\eta}\left(u^2+v^2\right)+u\frac{\partial T}{\partial\xi}+v\frac{\partial T}{\partial\eta}\right]- \\ -\rho ub_\xi-\rho vb_\eta+\frac{\partial(pu)}{\partial\xi}+\frac{\partial(pv)}{\partial\eta}=0 \tag{3.55}$$

To this expression we add the steady continuity equation, $\nabla\cdot(\rho\mathbf{u})=0$, multiplied by the temperature,

$$\rho\left[\frac{u}{2}\frac{\partial}{\partial\xi}\left(u^2+v^2\right)+\frac{v}{2}\frac{\partial}{\partial\eta}\left(u^2+v^2\right)+u\frac{\partial T}{\partial\xi}+v\frac{\partial T}{\partial\eta}\right]- \\ -\rho ub_\xi-\rho vb_\eta+\frac{\partial(pu)}{\partial\xi}+\frac{\partial(pv)}{\partial\eta}+T\left[\frac{\partial}{\partial\xi}(\rho u)+\frac{\partial}{\partial\eta}(\rho v)\right]=0 \tag{3.56}$$

We combine terms,

$$\rho\left[\frac{u}{2}\frac{\partial}{\partial\xi}\left(u^2+v^2\right)+\frac{v}{2}\frac{\partial}{\partial\eta}\left(u^2+v^2\right)\right]+\frac{\partial}{\partial\xi}(\rho uT)+\frac{\partial}{\partial\eta}(\rho vT)- \\ -\rho ub_\xi-\rho vb_\eta+\frac{\partial(pu)}{\partial\xi}+\frac{\partial(pv)}{\partial\eta}=0 \tag{3.57}$$

To re–phrase the mean kinetic energy terms we again add the continuity equation multiplied by $(u^2+v^2)/2$,

$$\frac{\rho u}{2}\frac{\partial}{\partial\xi}\left(u^2+v^2\right)+\frac{\rho v}{2}\frac{\partial}{\partial\eta}\left(u^2+v^2\right)+\frac{\partial}{\partial\xi}(\rho uT)+\frac{\partial}{\partial\eta}(\rho vT)- \\ -\rho ub_\xi-\rho vb_\eta+\frac{\partial(pu)}{\partial\xi}+\frac{\partial(pv)}{\partial\eta}+\left(\frac{u^2+v^2}{2}\right)\left[\frac{\partial}{\partial\xi}(\rho u)+\frac{\partial}{\partial\eta}(\rho v)\right]=0 \tag{3.58}$$

Which combines to form,

$$\frac{1}{2}\frac{\partial}{\partial\xi}\left[(\rho u)(u^2+v^2)\right]+\frac{1}{2}\frac{\partial}{\partial\eta}\left[(\rho v)(u^2+v^2)\right]+\frac{\partial}{\partial\xi}(\rho uT)+\frac{\partial}{\partial\eta}(\rho vT)- \\ -\rho ub_\xi-\rho vb_\eta+\frac{\partial(pu)}{\partial\xi}+\frac{\partial(pv)}{\partial\eta}=0 \tag{3.59}$$

We integrate over the shock thickness $\delta(\xi)$,

$$\frac{1}{2}\int_0^\delta \frac{\partial}{\partial\xi}\left[(\rho u)(u^2+v^2)\right]d\eta + \frac{1}{2}\int_0^\delta \frac{\partial}{\partial\eta}\left[(\rho v)(u^2+v^2)\right]d\eta + \int_0^\delta \frac{\partial}{\partial\xi}(\rho uT)d\eta + \\ + \int_0^\delta \frac{\partial}{\partial\eta}(\rho vT)d\eta - \int_0^\delta \rho u b_\xi d\eta - \int_0^\delta \rho v b_\eta d\eta + \int_0^\delta \frac{\partial(pu)}{\partial\xi}d\eta + \int_0^\delta \frac{\partial(pv)}{\partial\eta}d\eta = 0 \quad (3.60)$$

Using Leibniz's rule on the appropriate integrals,

$$\frac{1}{2}\frac{\partial}{\partial\xi}\int_0^\delta \left[(\rho u)(u^2+v^2)\right]d\eta - \frac{1}{2}\frac{\partial\delta}{\partial\xi}(\rho u)(u^2+v^2)\Big|_{\eta=\delta} + \\ + \frac{1}{2}\Big[(\rho v)(u^2+v^2)\Big]_{\eta=0}^{\eta=\delta} + \frac{\partial}{\partial\xi}\int_0^\delta (\rho uT)d\eta - \frac{\partial\delta}{\partial\xi}(\rho uT)\Big|_{\eta=\delta} + \Big[\rho vT\Big]_{\eta=0}^{\eta=\delta} - \\ -\mathbb{J}_3 - \mathbb{J}_4 + \frac{\partial}{\partial\xi}\int_0^\delta pu d\eta - \frac{\partial\delta}{\partial\xi}pu\Big|_{\eta=\delta} + \Big[pv\Big]_{\eta=0}^{\eta=\delta} = 0 \quad (3.61)$$

where we have denoted the body force integrations as $\mathbb{J}_3$ and $\mathbb{J}_4$. Labeling depth–averaged quantities with overbars and shock–evaluated quantities with subscripted s,

$$\frac{1}{2}\frac{\partial}{\partial\xi}\left[\delta\overline{(\rho u)(u^2+v^2)}\right] - \frac{1}{2}\frac{\partial\delta}{\partial\xi}(\rho_s u_s)(u_s^2+v_s^2) + \\ + \frac{1}{2}(\rho_s v_s)(u_s^2+v_s^2) + \frac{\partial}{\partial\xi}\left[\delta\overline{\rho uT}\right] - \frac{\partial\delta}{\partial\xi}(\rho_s u_s T_s) + \rho_s v_s T_s - \\ -\mathbb{J}_3 - \mathbb{J}_4 + \frac{\partial}{\partial\xi}(\delta\overline{pu}) - \frac{\partial\delta}{\partial\xi}p_s u_s + p_s v_s = 0 \quad (3.62)$$

As usual we look to replace the shock–evaluated quantities in favor of upstream conditions, δ', and θ by use of the jump conditions of Chapter 2. Consider each term separately,

$$-\frac{1}{2}\delta'(\rho_s u_s)(u_s^2+v_s^2) + \frac{1}{2}(\rho_s v_s)(u_s^2+v_s^2)$$

$$\frac{1}{2}\rho_s(u_s^2+v_s^2)\left(v_s - \delta' u_s\right) \quad (3.63)$$

Consider the quantity $v_s - \delta' u_s$, (recall $\phi \equiv \beta - \theta$)

$$v_s - \delta' u_s = [-u_2 \cos\phi + w_2 \sin\phi] - \tan\phi\,[u_2 \sin\phi + w_2 \cos\phi]$$

$$v_s - \delta' u_s = -u_2 \cos\phi - u_2 \tan\phi \sin\phi$$

$$v_s - \delta' u_s = -\frac{u_2}{\cos\phi} = -\frac{u_2}{\cos(\beta - \theta)} \tag{3.64}$$

Note that $(u_s^2 + v_s^2)$ is the squared magnitude of the total post–shock velocity, V_2. Thus Equation (3.63) is,

$$-\frac{\rho_2 V_2^2 u_2}{2\cos(\beta - \theta)}$$

From Section 2.3.6 we have the continuity relation,

$$\rho_1 u_1 = \rho_1 V_1 \sin\beta = \rho_2 u_2 = \rho_2 V_2 \sin(\beta - \theta) \tag{3.65}$$

and thus our term of interest becomes,

$$-\frac{\rho_1^3 u_1^3}{2\delta'^2 \rho_2^2 \cos^3(\beta - \theta)}$$

$$-\frac{\rho_1^3 V_1^3 \sin^3\beta}{2\delta'^2 \rho_2^2 \cos^3(\beta - \theta)}$$

$$-\frac{\rho_1^3 V_1^3}{2\delta'^2 \rho_2^2} \left(\delta' \cos\theta + \sin\theta\right)^3$$

$$-\frac{\rho_1 r^2 V_1^3}{2\delta'^2} \left(\delta' \cos\theta + \sin\theta\right)^3 \tag{3.66}$$

where we have employed the definition $r \equiv \rho_1/\rho_2 = \nu_1/\nu_2$ as the ratio of densities we defined in Chapter 2.

The next term of (3.62) to evaluate is

$$-\delta'\rho_s u_s T_s + \rho_s v_s T_s$$

$$\rho_s T_s \left(v_s - \delta' u_s\right)$$

By (3.64) we have,

$$-\frac{\rho_2 T_2 u_2}{\cos(\beta-\theta)}$$

With Equation (2.90) for T_2,

$$-\frac{\rho_1 V_1 \sin\beta}{\cos(\beta-\theta)}\left[\frac{p_1 + \rho_1 V_1^2 \sin^2\beta\,(1-r)}{\rho_2\,(1+2G_2)}\right]$$

We rearrange,

$$-\frac{r p_1 V_1 \sin\beta + r(1-r)\rho_1 V_1^3 \sin^3\beta}{(1+2G_2)\cos(\beta-\theta)}$$

$$-\frac{\sin\beta}{\cos(\beta-\theta)}\left[\frac{r p_1 V_1 + r(1-r)\rho_1 V_1^3 \sin^2\beta}{(1+2G_2)}\right]$$

$$-\left[\delta'\cos\theta + \sin\theta\right]\left[\frac{r p_1 V_1(1+\delta'^2) + r(1-r)\rho_1 V_1^3(\delta'\cos\theta + \sin\theta)^2}{(1+2G_2)\,(1+\delta'^2)}\right]$$

Finally we look to manipulate

$$-\frac{\partial\delta}{\partial\xi}p_s u_s + p_s v_s$$

$$p_2\left(v_s - \delta' u_s\right)$$

with (3.64)

$$-\frac{p_2 u_2}{\cos(\beta-\theta)}$$

$$-\frac{(p_1 + \rho_1 u_1^2 - \rho_2 u_2^2)u_2}{\cos(\beta-\theta)}$$

with $u_2 = ru_1$,

$$-\frac{rp_1u_1 + r(1-r)\rho_1u_1^3}{\cos(\beta-\theta)}$$

$$-\frac{\sin\beta}{\cos(\beta-\theta)}\left[rp_1V_1 + r(1-r)\rho_1V_1^3\sin^2\beta\right]$$

$$-\left(\delta'\cos\theta+\sin\theta\right)\left[\frac{rp_1V_1(1+\delta'^2) + r(1-r)\rho_1V_1^3\left(\delta'\cos\theta+\sin\theta\right)^2}{1+\delta'^2}\right]$$

With the re–phrased terms the energy equation becomes (neglecting body force terms),

$$\begin{aligned}\frac{1}{2}\frac{\partial}{\partial\xi}\left[\delta\overline{(\rho u)(u^2+v^2)}\right] + \frac{\partial}{\partial\xi}\left[\delta\overline{\rho uT}\right] + \frac{\partial}{\partial\xi}(\delta\overline{pu}) - \frac{\rho_1r^2V_1^3}{2\delta'^2}\left(\delta'\cos\theta+\sin\theta\right)^3 - \\ -\left[\delta'\cos\theta+\sin\theta\right]\left[\frac{rp_1V_1(1+\delta'^2) + r(1-r)\rho_1V_1^3(\delta'\cos\theta+\sin\theta)^2}{(1+2G_2)\left(1+\delta'^2\right)}\right] \\ -\left(\delta'\cos\theta+\sin\theta\right)\left[\frac{rp_1V_1(1+\delta'^2) + r(1-r)\rho_1V_1^3\left(\delta'\cos\theta+\sin\theta\right)^2}{1+\delta'^2}\right] = 0\end{aligned} \tag{3.67}$$

which may be re–written,

$$\begin{aligned}\frac{1}{2}\frac{\partial}{\partial\xi}\left[\delta\overline{(\rho u)(u^2+v^2)}\right] + \frac{\partial}{\partial\xi}\left[\delta\overline{\rho uT}\right] + \frac{\partial}{\partial\xi}(\delta\overline{pu}) - \frac{\rho_1r^2V_1^3}{2\delta'^2}\left(\delta'\cos\theta+\sin\theta\right)^3 - \\ -\frac{2\left(\delta'\cos\theta+\sin\theta\right)\left(1+G_2\right)\left[rp_1V_1(1+\delta'^2) + r(1-r)\rho_1V_1^3(\delta'\cos\theta+\sin\theta)^2\right]}{(1+2G_2)\left(1+\delta'^2\right)} = 0\end{aligned} \tag{3.68}$$

Divide out the constituent material density ρ_m

$$\begin{aligned}\frac{1}{2}\frac{\partial}{\partial\xi}\left[\delta\overline{(\nu u)(u^2+v^2)}\right] + \frac{\partial}{\partial\xi}\left[\delta\overline{\nu uT}\right] + \frac{1}{\rho_m}\frac{\partial}{\partial\xi}(\delta\overline{pu}) - \frac{\nu_1r^2V_1^3}{2\delta'^2}\left(\delta'\cos\theta+\sin\theta\right)^3 - \\ -\frac{2\left(\delta'\cos\theta+\sin\theta\right)\left(1+G_2\right)\left[r(p_1/\rho_m)V_1(1+\delta'^2) + r(1-r)\nu_1V_1^3(\delta'\cos\theta+\sin\theta)^2\right]}{(1+2G_2)\left(1+\delta'^2\right)} = 0\end{aligned} \tag{3.69}$$

Note that the post–shock area fraction ν_2 appears without other post–shock quantities through r and the density function G_2. Thus we cannot eliminate ν_2 in favor of upstream quantities as we were able to accomplish with the mass and momentum relations. The use of (3.69) requires simplifying assumptions (such as $\nu_2 = \overline{\nu}$ or a dilute approxmation– see Section 2.3.8) or the solution to the jump conditions as in Chapter 2.

3.2 System of differential equations

To summarize the findings of the previous sections, we have the following relations for the shock thickness δ and shock depth–averaged quantities $\overline{\nu}$, $\overline{u}$, $\overline{v}$, and $\overline{p}$ (or $\overline{T}$):

Mass:

$$\frac{\partial}{\partial \xi}(\overline{\nu u}\delta) = \nu_1 V_1(\delta' \cos\theta + \sin\theta) \tag{3.70}$$

ξ–Momentum:

$$\rho_m \frac{\partial}{\partial \xi}\left(\overline{\nu u^2}\delta + \frac{\overline{p}\delta}{\rho_m}\right) - (\rho_m \nu_1 V_1^2 \cos^2\theta + p_1)\frac{d\delta}{d\xi} = \rho_m \nu_1 V_1^2 \sin\theta\cos\theta \tag{3.71}$$

η–Momentum:

$$\rho_m \frac{\partial}{\partial \xi}\left(\delta\overline{\nu u v}\right) + p_1 + \rho_m \nu_1 V_1^2(\delta' \sin\theta\cos\theta + \sin^2\theta) - p_b = 0 \tag{3.72}$$

Energy:

$$\frac{1}{2}\frac{\partial}{\partial \xi}\left[\delta\overline{(\nu u)(u^2+v^2)}\right] + \frac{\partial}{\partial \xi}\left[\delta\overline{\nu u T}\right] + \frac{1}{\rho_m}\frac{\partial}{\partial \xi}(\delta\overline{p u}) - \frac{\nu_1 r^2 V_1^3}{2\delta'^2}\left(\delta'\cos\theta + \sin\theta\right)^3 - \\ - \frac{2\left(\delta'\cos\theta + \sin\theta\right)\left(1+G_2\right)\left[r(p_1/\rho_m)V_1(1+\delta'^2) + r(1-r)\nu_1 V_1^3(\delta'\cos\theta + \sin\theta)^2\right]}{\left(1+2G_2\right)\left(1+\delta'^2\right)} = 0 \tag{3.73}$$

With 4 first–order differential equations in 6 unknowns ($\overline{\nu}, \overline{p}, \overline{u}, \overline{v}, \delta, p_b$), we require simplification of this system to obtain solutions for our variables of interest. We therefore require (at minimum) two fewer unknowns.

The first assumption is that of constant post–shock area fraction $\overline{\nu}$. The system of equations for the subcritical wedge with no body force (Section 2.5.2) is identically satisfied– all post–shock values are constant by nature of the constant wedge and upstream conditions. Inspection of simulation images of bow shocks such as with supercritical wedges (Section 2.5.3) indicates that there does not appear to

be a significant density gradient in the shocked region. Recall the shock transitions of Chapter 2. Figure 3.2 shows that the post–shock area fraction is relatively constant for strong shocks ($\beta > \beta_c$, where β_c is the shock angle at critical flow turning angle θ_c). That is, $d\nu_2/d\beta$ decreases as β increases towards the normal shock. We note that for the bow shock over the supercritical wedge (Figure 2.16) the shock angle β is relatively large and the local post–shock densities are, hence, nearly equal. This assumption reduces the number of differential equations to solve– we may neglect the energy equation and regard the fourth equation as $d\nu/d\xi = 0$.

We also make the assumption that the depth–averaged body–normal velocity component $\overline{v}$ is zero. Equivalently, the depth–averaged flow is parallel to the body at each point. As with the assumption of constant density, this condition is assumed satisfied in our prior use of the local jump equations of Chapter 2. Note that $\overline{v} = 0$ does not violate our restriction on the flow turning angle, which requires $\theta \leq \theta_c$. In the evaluation of the flow quantities at the shock (subscripted "s") we made use of the jump conditions that enforce this limit. Only in the depth–averaged sense does the flow align with the body of general angle θ, possibly supercritical.

With regards to the body pressure p_b, we discuss two simple approximations. The first, explored in Section 3.2.1, equates the body pressure and the depth–averaged pressure ($p_b = \overline{p}$). The second, Section 3.2.3 sets the depth–averaged pressure equal to the mean of the shock pressure p_2 and the body pressure, $p = \frac{1}{2}(p_2 + p_b)$, so that $p_b = 2\overline{p} - p_2$.

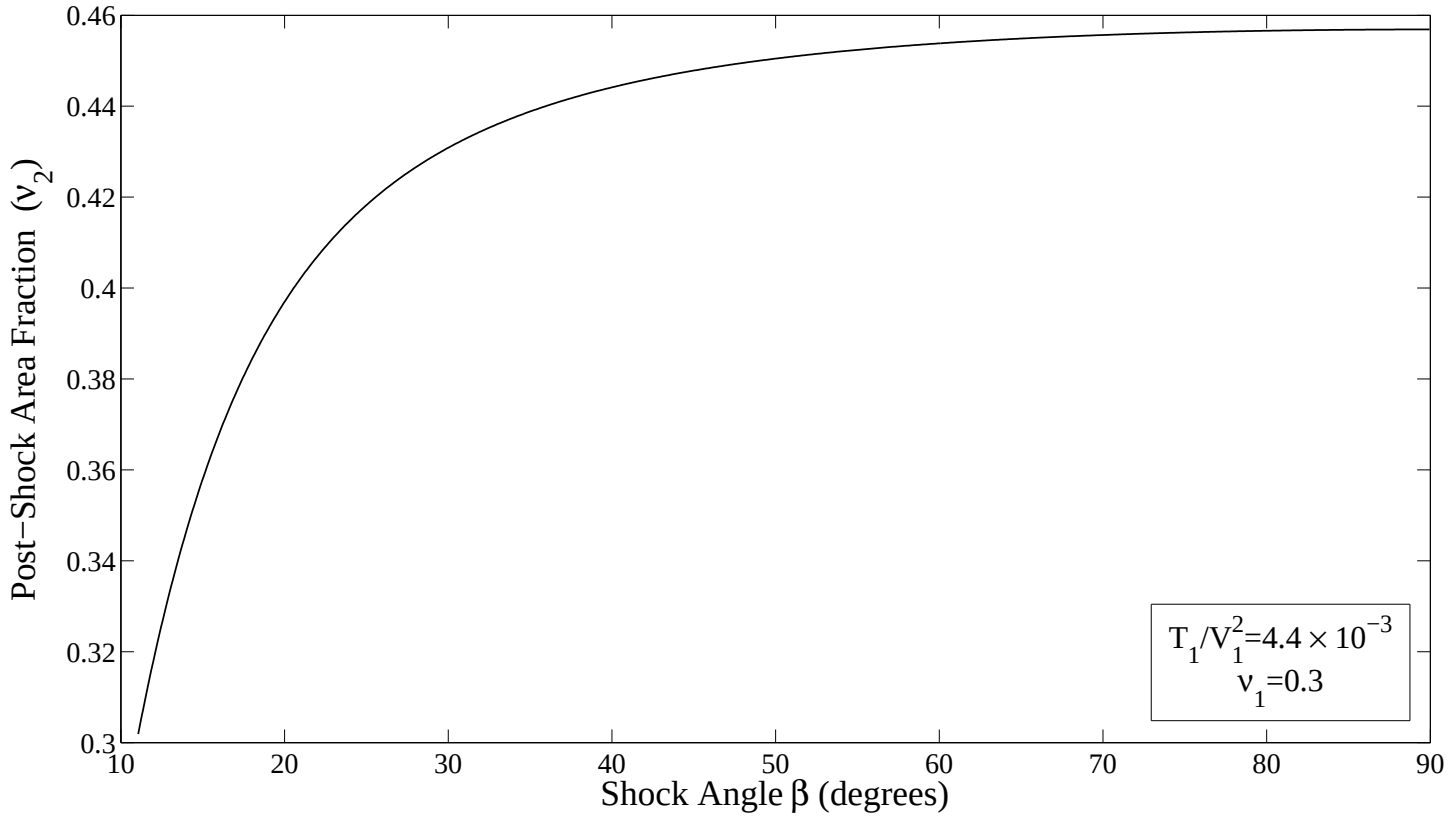

Figure 3.2: Post–shock density ν_2 plotted against shock angle β. Note that for larger β values, $d\nu_2/d\beta$ is small.

3.2.1 Case 1: $\overline{p} = p_b$

Specifying $\overline{p} = p_b$ with $\overline{v} = 0$ and constant $\overline{\nu}$ we have 3 unknowns $\overline{p}, \overline{u}, \delta$ in 3 differential equations. Equivalently we have 4 total equations in the 4 unknowns $\overline{p}, \overline{u}, \delta, \nu$ where the fourth differential equation is the trivial expression $d\nu/d\xi = 0$. The value of $\overline{\nu}$ may be determined from the energy equation, as we will show. We approximate the depth–averaged quantities as follows,

$$\overline{\nu u} \approx \overline{\nu}\ \overline{u}$$

$$\overline{\nu u^2} \approx \overline{\nu}\ \overline{u}^2$$

$$\overline{\nu u v} \approx 0$$

At this point we no longer maintain the overline notation to denote a depth–averaged quantity. Upstream and immediately post–shock conditions are still identified with subscripts. Our simplified governing equations reduce to,

$$\nu \frac{\partial}{\partial \xi}(u\delta) = \nu_1 V_1(\delta' \cos\theta + \sin\theta) \tag{3.74}$$

$$\rho_m \nu \frac{\partial}{\partial \xi}\left(u^2\delta\right) + \frac{\partial}{\partial \xi}(p\delta) - (\rho_m \nu_1 V_1^2 \cos^2\theta + p_1)\frac{d\delta}{d\xi} = \rho_m \nu_1 V_1^2 \sin\theta\cos\theta \tag{3.75}$$

$$p_1 + \rho_m \nu_1 V_1^2(\delta' \sin\theta\cos\theta + \sin^2\theta) - p = 0 \tag{3.76}$$

With knowledge of the body shape $\theta(\xi)$ and $\xi = 0$ boundary conditions on p, u, δ we are able, in principle, to solve this coupled system of non–linear differential equations. Note that we also require specification of ν, a boundary condition for our fourth equation $d\nu/d\xi = 0$, which must satisfy the energy equation.

We now apply equations (3.74)–(3.76) to the case of the straight wedge as in Chapter 2. In this geometry, terms involving θ may be reduced to constants.

With all quantities of interest having functional dependence on only ξ the partial derivatives become ordinary derivatives.

$$\nu \frac{d}{d\xi}(u\delta) - A\delta' = B \tag{3.77}$$

$$\rho_m \nu \frac{d}{d\xi}(u^2\delta) + \frac{d}{d\xi}(p\delta) - C\delta' = D \tag{3.78}$$

$$-D\delta' + p = E \tag{3.79}$$

where,

$$A \equiv \nu_1 V_1 \cos\theta$$

$$B \equiv \nu_1 V_1 \sin\theta$$

$$C \equiv \rho_m \nu_1 V_1^2 \cos^2\theta + p_1$$

$$D \equiv \rho_m \nu_1 V_1^2 \cos\theta \sin\theta$$

$$E \equiv \rho_m \nu_1 V_1^2 \sin^2\theta + p_1$$

We seek to write our equations in a first–order form appropriate for a numerical solver such as MATLAB's `ode45()`. We first expand the differential equations above,

$$\nu(u\delta' + u'\delta) - A\delta' = B \tag{3.80}$$

$$\rho_m \nu(u^2\delta' + 2u\delta u') + p'\delta + p\delta' - C\delta' = D \tag{3.81}$$

$$-D\delta' + p = E \tag{3.82}$$

We start with (3.82) and write as,

$$\delta' = \frac{p - E}{D} \tag{3.83}$$

We apply this to (3.80) solved for u',

$$u' = \frac{B + (A - \nu u)\delta'}{\nu\delta} \tag{3.84}$$

$$u' = \frac{BD + (A - \nu u)(p - E)}{D\nu\delta} \tag{3.85}$$

Finally we solve (3.81) for p',

$$p' = \frac{D}{\delta} + \frac{(C - \rho_m \nu u^2 - p)}{\delta}\delta' - 2\rho_m \nu u u'$$

$$p' = \frac{D}{\delta} + \frac{(C - \rho_m \nu u^2 - p)(p - E)}{D\delta} - 2\rho_m u \left(\frac{BD + (A - \nu u)(p - E)}{D\delta}\right) \tag{3.86}$$

Equations (3.83)–(3.86) are phrased in the standard form of $\mathbf{F}' = \underline{f}(\mathbf{F})$.

With expressions (3.83), (3.85), and (3.86) for our derivatives, the energy equation determines the value of ν.

Application to the subcritical and critical wedge

Here we examine our system of differential equations in an application to subcritical and critical wedges. In such a geometry, the governing equations simplify greatly and we are able to recover the results of Chapter 2. We employ our relations at the critical angle to yield an expression that determines θ_c as a function of upstream conditions T_1/V_1^2 and ν_1.

For the straight, *attached* shock, we expect the shock location δ to be a linear function of the body coordinate ξ,

$$\delta(\xi) = \omega\xi \tag{3.87}$$

where ω is a constant. Alternatively, we could obtain this by solution of the differential equation $\delta' = \omega$ with the attachment boundary condition $\delta(0) = 0$. Application of this to (3.80) results in a differential equation for the speed u,

$$\xi u' + u = \frac{B + A\omega}{\nu\omega} \tag{3.88}$$

This has the form of a Cauchy–Euler differential equation [7]. Our general solution is,

$$u(\xi) = \frac{C_1}{\xi} + \frac{B + A\omega}{\nu\omega} \tag{3.89}$$

We take $C_1 = 0$ which keeps u bounded as ξ approaches zero. Thus our constant post–shock depth–average flow speed is

$$u = \frac{B + A\omega}{\nu\omega} \tag{3.90}$$

which may be rewritten in terms of the density ratio r,

$$u = rV_1 \cos\theta + \frac{rV_1 \sin\theta}{\omega} \tag{3.91}$$

We thus note that $u' = 0$ as we expect for the subcritical wedge. By (3.82) we also note that

$$p = D\omega + E \tag{3.92}$$

and $p' = 0$. With these conditions we restate our simplified differential equation system,

$$\delta' = \omega = \tan(\beta - \theta) = \frac{p - E}{D} \tag{3.93}$$

$$u' = 0 = BD + (A - \nu u)(p - E) \tag{3.94}$$

$$p' = 0 = D^2 + (C - \rho_m \nu u^2 - p)(p - E) \tag{3.95}$$

where the constants are the same as in the previous section. Note that we have reduced our system to 3 *algebraic* equations. In adddition to these relations, the continuity of the velocity component tangent to the shock gives us,

$$V_1 \cos\beta = u\cos(\beta - \theta) \tag{3.96}$$

which can be solved for $\tan\beta$,

$$\tan\beta = \frac{V_1 - u\cos\theta}{u\sin\theta} \tag{3.97}$$

Using the trigonometric identity, (2.97), for $\tan(\beta-\theta)$ with the above equation we obtain,

$$\tan(\beta - \theta) = \frac{V_1\cos\theta - u}{V_1\sin\theta} \tag{3.98}$$

Our algebraic system of equations is now in terms of only u, p, and ν,

$$\frac{V_1\cos\theta - u}{V_1\sin\theta} = \frac{p-E}{D} \tag{3.99}$$

$$BD + (A - \nu u)(p - E) = 0 \tag{3.100}$$

$$D^2 + (C - \rho_m \nu u^2 - p)(p - E) = 0 \tag{3.101}$$

Solve (3.99) for p,

$$p = \frac{EV_1\sin\theta + DV_1\cos\theta - Du}{V_1\sin\theta} = \frac{F - Du}{V_1\sin\theta} \tag{3.102}$$

where $F \equiv EV_1\sin\theta + DV_1\cos\theta$. Use this result in (3.100),

$$BD + A\left[\frac{F-Du}{V_1\sin\theta}\right] - AE - \nu u\left[\frac{F-Du}{V_1\sin\theta}\right] + E\nu u = 0$$

which simplifies to,

$$\nu_1 V_1^2 - uV_1\cos\theta(\nu_1 + \nu) + \nu u^2 = 0 \tag{3.103}$$

We now solve this quadratic for u,

$$u = \frac{V_1(\nu_1+\nu)\cos\theta \pm \sqrt{V_1^2\cos^2\theta(\nu_1+\nu)^2 - 4V_1^2\nu\nu_1}}{2\nu} \tag{3.104}$$

Consider the discriminant of the radical phrased in terms of r,

$$\Delta = V_1^2 \nu^2 (\cos^2\theta (r+1)^2 - 4r) \tag{3.105}$$

For a real solution u, we require that,

$$\cos^2\theta (r+1)^2 - 4r \geq 0 \tag{3.106}$$

Thus we have a straight, attached shock if,

$$\frac{4r}{(r+1)^2} \leq \cos^2\theta \tag{3.107}$$

Note that this is equivalent to the condition on the discriminant of (2.98), where our concern was the requirement of real solutions of the jump equations for $\tan\beta$.

As with the solution of the algebraic jump conditions, we are unable to obtain a closed–form solution for the flow variables without additional simplification (such as a dilute approximation). Note that the solutions for p, u, and δ require a value of ν before any may be explicitly determined. We arrive at this value using the energy equation (3.73). With the knowledge that post–shock quantities are constant and $v = 0$, this simplifies to

$$\delta' \nu u \left[\frac{u^2}{2} + T + \frac{p}{\rho_m \nu}\right] - \frac{\nu_1 r^2 V_1^3}{2\delta'^2} K^3 - \\ - \frac{2K(1+G_2)\left[r(p_1/\rho_m)V_1(1+\delta'^2) + r(1-r)\nu_1 V_1^3 K^2\right]}{(1+2G_2)(1+\delta'^2)} = 0$$

where the common term $K \equiv \delta'\cos\theta + \sin\theta$ is used to shorten the expression. To avoid confusion with the quantity u_2 employed as the shock–normal velocity of Chapter 2, we write the total post–shock speed u as V_2. Additionally, we identify p, T, and ν as the familiar post–shock quantities subscripted with "2". By the energy jump condition (2.78) we modify the term in brackets,

$$\delta' \nu_2 V_2 \left[\frac{V_2^2}{2} + T_1 + \frac{p_1}{\rho_m \nu_1} + \frac{u_1^2}{2} - \frac{u_2^2}{2}\right] - \frac{\nu_1 r^2 V_1^3}{2\delta'^2} K^3 - \\ - \frac{2K(1+G_2)\left[r(p_1/\rho_m)V_1(1+\delta'^2) + r(1-r)\nu_1 V_1^3 K^2\right]}{(1+2G_2)(1+\delta'^2)} = 0$$

which may be rewritten as,

$$\delta'\nu_2 V_2\left[\frac{V_2^2\cos^2(\beta-\theta)}{2}+T_1+\frac{p_1}{\rho_m\nu_1}+\frac{V_1^2\sin^2\beta}{2}\right]-\frac{\nu_1 r^2 V_1^3}{2\delta'^2}K^3- \\ -\frac{2K(1+G_2)\left[r(p_1/\rho_m)V_1(1+\delta'^2)+r(1-r)\nu_1 V_1^3K^2\right]}{(1+2G_2)\,(1+\delta'^2)}=0$$

After simplification we arrive at,

$$\left(1+\delta'^2\right)\left[\frac{2p_1}{\rho_m\nu_1}(K-2\delta' MN_2)+2T_1K-V_1^2M^2K\right]+ \\ M^2KV_1^2+V_1^2F^3-4\delta' MK^2N_2V_1^2+4\delta'^2M^2KN_2V_1^2=0 \qquad (3.108)$$

where $M \equiv \cos\theta - \delta'\sin\theta$ and $N_2 \equiv (1+G_2)/(1+2G_2)$. This expression is currently in terms of δ' and ν_2. However, with the use of (2.96) we are able to write $\nu_2(\delta')$ or $\delta'(\nu_2)$. To complete the solution of our simplified algebraic system Equation (3.108) we must find the roots of (3.108).

The solutions obtained from (3.91) and (3.102) with (3.108) yield the same results as from the jump conditions alone. Indeed, the jump conditions were employed in the derivation of the differential expressions; without gradients in the flow quantities, the differential equation system was reduced to the re–phrased algebraic system of Chapter 2.

While, in general, solutions at $\theta < \theta_c$ in general require a root finding process as described above and in Chapter 2, our expressions simplify greatly at $\theta = \theta_c$. At this critical angle we expect a single solution; we return to (3.104) and set the discriminant equal to zero,

$$u_c = \frac{V_1(r_c+1)\cos\theta_c}{2} \qquad (3.109)$$

where we use the subscript c to make it explicit that we consider a quantity at θ_c.

We equate this with our general solution for u, equation (3.91),

$$r_c V_1 \cos\theta_c + \frac{r_c V_1 \sin\theta_c}{\omega_c} = \frac{V_1(r_c+1)\cos\theta_c}{2} \tag{3.110}$$

$$\frac{r_c \sin\theta_c}{\omega_c} = \frac{(1-r_c)\cos\theta_c}{2} \tag{3.111}$$

$$\omega_c = \frac{2r_c \tan\theta_c}{(1-r_c)} \tag{3.112}$$

From (2.96) we have in general,

$$r = \frac{\tan(\beta-\theta)}{\tan\beta} = \frac{\omega}{\tan\beta} \tag{3.113}$$

Then,

$$\tan\beta_c = \frac{2\tan\theta_c}{(1-r_c)} \tag{3.114}$$

From (3.107), at $\theta = \theta_c$ we satisfy,

$$\frac{4r_c}{(r_c+1)^2} = \cos^2\theta_c \tag{3.115}$$

or,

$$4r_c \tan^2\theta_c = (r_c-1)^2 \tag{3.116}$$

We square (3.114) and substitute to arrive at,

$$\tan^2\beta_c = \frac{1}{r_c} \tag{3.117}$$

which may be written as,

$$\tan\beta_c = \frac{1}{\tan(\beta_c-\theta_c)} \tag{3.118}$$

Using the trigonometric identity (2.97) for $\tan(\beta-\theta)$, we obtain

$$\tan^2\beta_c - 2\tan\beta_c \tan\theta_c - 1 = 0 \tag{3.119}$$

which has the solution,

$$\tan\beta_c = \frac{\sin\theta_c \pm 1}{\cos\theta_c} \tag{3.120}$$

of which only the positive solution is physically meaningful if $\beta \geq 0$.

With the $\beta_c - \theta_c$ relationship satisfied, we have a density ratio given by (3.117) as,

$$r_c = \frac{\cos^2\theta_c}{(\sin\theta_c + 1)^2} \tag{3.121}$$

or

$$\nu_2 = \nu_1 \frac{(\sin\theta_c + 1)^2}{\cos^2\theta_c} \tag{3.122}$$

We also solve for the speed u_c from (3.109),

$$u_c = \frac{V_1 \cos\theta_c}{\sin\theta_c + 1} \tag{3.123}$$

(equivalent to V_2. The pressure, from (3.102), is

$$p_c = \rho_m \nu_1 V_1^2 \sin\theta_c + p_1 \tag{3.124}$$

If we apply these expressions in the energy equation, we are able to obtain a relationship between the upstream quantities and the critical angle. Specifically, we use equation (2.95) applied at the critical angle,

$$\begin{aligned} &\left[16(1-\nu_1)^2\sin^2\beta + 4\Sigma(9\nu_1^2 - 16\nu_1 + 16)\right]\nu_2^3 - \\ &- \left[272\nu_1(1-\nu_1)^2\sin^2\beta + 32\Sigma(7\nu_1 + 2\nu_1^2)\right]\nu_2^2 + \\ &+ \left[128(1-\nu_1)^2(1+4\nu_1)\sin^2\beta + 64\Sigma(\nu_1^2+8)\right]\nu_2 - \\ &- \left[384\nu_1(1-\nu_1)^2\sin^2\beta\right] = 0 \end{aligned} \tag{3.125}$$

where we recall that $\Sigma = T_1/V_1^2$. We denote $\kappa \equiv (\sin\theta_c + 1)/\cos\theta_c$ and use (3.120) to write,

$$\sin^2\beta = \frac{\kappa^2}{1+\kappa} \tag{3.126}$$

With $\nu_2 = \nu_1\kappa^2$, we arrive at an expression in terms of θ_c and upstream quantities. In principle, we are able to solve this numerically to determine $\theta_c(\Sigma, \nu_1)$. Thus, given upstream flow conditions, we are able to determine the wedge angle at which we lose the straight shock solution and expect a detached bow shock to form.

3.2.2 Dilute Approximation

As in Chapter 2 the dilute approximation gives us an equation of state $p = \rho_m \nu T$ because the density function $G(\nu)$ is small compared to one. This only affects the energy equation, which becomes

$$\frac{1}{2}\frac{\partial}{\partial\xi}\left[\delta\overline{(\nu u)(u^2+v^2)}\right] + \frac{\partial}{\partial\xi}\left[\delta\overline{\nu u T}\right] + \frac{1}{\rho_m}\frac{\partial}{\partial\xi}(\delta\overline{pu}) - \frac{\nu_1 r^2 V_1^3}{2\delta'^2}\left(\delta'\cos\theta + \sin\theta\right)^3 - \\ -\frac{2\left(\delta'\cos\theta+\sin\theta\right)\left[r(p_1/\rho_m)V_1(1+\delta'^2) + r(1-r)\nu_1 V_1^3(\delta'\cos\theta+\sin\theta)^2\right]}{(1+\delta'^2)} = 0 \tag{3.127}$$

With regards to the subcritical/critical wedge, solutions for the quantities u, p, δ remain the same in terms of the area fraction ν. The dilute approximation alters the roots of the energy equation determining ν and thus the dependent quantities.

Recall our solution for ν_2 resulting from use of the dilute jump equations, (2.104)

$$\nu_2 = \frac{3\nu_1 V_1^2 \sin^2\beta}{V_1^2\sin^2\beta + 4T_1} \tag{3.128}$$

At the critical angle we found $\nu_2 = \nu_1\kappa^2$. We apply this with (3.126) for $\sin^2\beta$ to

find

$$\kappa^2 = \frac{3V_1^2 - 4T_1}{V_1^2 + 4T_1} \equiv \mathbb{A} \tag{3.129}$$

Employ the definition of κ,

$$\frac{(\sin\theta_c + 1)^2}{\cos^2\theta_c} = \mathbb{A} \tag{3.130}$$

which results in a quadratic in $\sin\theta_c$

$$(1 + \mathbb{A})\sin^2\theta_c + 2\sin\theta_c + 1 - \mathbb{A} = 0 \tag{3.131}$$

which has the solution,

$$\sin\theta_c = \frac{-1 \pm \mathbb{A}}{1 + \mathbb{A}} \tag{3.132}$$

The solution corresponding to the negative sign is not physically sensible ($\sin\theta_c = -1$), so we are left with,

$$\sin\theta_c = \frac{-1 + \mathbb{A}}{1 + \mathbb{A}} \tag{3.133}$$

which simplifies to,

$$\sin\theta_c = \frac{1}{2} - 2\Sigma \tag{3.134}$$

If $V_1^2 \gg T_1$, in this limit $\theta_c = \sin^{-1}(1/2) = 30^\circ$ and $\beta_c = 60^\circ$. Note the comparison with Figure 2.8 where $\Sigma = 4 \times 10^{-4}$. Also note that if $\theta_c = 0^\circ$, $\Sigma = 1/4$. At this value we have a Mach Number of $M = \sqrt{2}$ and a Mach angle (β_{min}) of 45° by 2.107.

3.2.3 Case 2: $\overline{p} = \frac{1}{2}(p_2 + p_b)$

In our second assumption regarding the body pressure p_b term of (3.72), we regard the depth–averaged pressure as the mean of p_b and the post–shock pressure p_2. Thus,

$$p_b = 2\overline{p} - p_2 \tag{3.135}$$

Applied to (3.72) we have,

$$\rho_m \frac{\partial}{\partial \xi}\left(\delta \overline{\nu u v}\right) + p_1 + \rho_m \nu_1 V_1^2(\delta' \sin\theta\cos\theta + \sin^2\theta) - (2\overline{p} - p_2) = 0 \qquad (3.136)$$

With our assumptions of $\overline{v} = 0$ and constant area fraction this reduces to .

$$p_1 + p_2 + \rho_m \nu_1 V_1^2(\delta' \sin\theta\cos\theta + \sin^2\theta) - 2\overline{p} = 0 \qquad (3.137)$$

Using the jump condition for the shock–normal momentum (2.76), we substitute for p_2,

$$p_1 + \left(p_1 + \rho_m \nu_1 u_1^2 - \rho_m \nu_2 u_2^2\right) + \rho_m \nu_1 V_1^2 \left(\delta' \sin\theta\cos\theta + \sin^2\theta\right) - 2p = 0$$

$$2p_1 + \rho_m \nu_1 u_1^2 - \rho_m \nu_2 u_2^2 + \rho_m \nu_1 V_1^2 \left(\delta' \sin\theta\cos\theta + \sin^2\theta\right) - 2p = 0 \qquad (3.138)$$

Using the continuity jump condition, $u_2 = \nu_1 u_1/\nu_2$,

$$2p_1 + \rho_m \nu_1 V_1^2 \sin^2\beta \left(1 - \frac{\nu_1}{\nu_2}\right) + \rho_m \nu_1 V_1^2 \left(\delta' \sin\theta\cos\theta + \sin^2\theta\right) - 2p = 0 (3.139)$$

We substitute for $\sin^2\beta$ from (3.20),

$$p = p_1 + \frac{\rho_m \nu_1 V_1^2(\delta'\cos\theta + \sin\theta)^2}{2(1+\delta'^2)}\left(1 - \frac{\nu_1}{\nu}\right) + \frac{\rho_m \nu_1 V_1^2}{2}\left(\delta' \sin\theta\cos\theta + \sin^2\theta\right)$$

After some rearrangement we obtain,

$$\begin{aligned} D\delta'^3 + \left[(2+r)p_1 - 2p + \rho_m \nu_1 V_1^2 - rC\right]\delta'^2 + \\ +(3D - 2rD)\delta' + 2E - rE + rp_1 - 2p = 0 \end{aligned} \qquad (3.140)$$

where the constants C, D, E, r are all as defined above. With this expression, (3.77), and (3.78) we have our three equations in p, δ, u. We solve the cubic of (3.140) to determine δ' in terms of p, known upstream quantities, and ν, which is determined from the energy equation or by approximation. This may then be used as in the prior section to obtain an equation system of the form $\mathbf{F}' = \underline{f}(\mathbf{F})$.

3.3 Numerical Solutions

Here we apply the governing differential equations to both the subcritical and supercritical wedge geometries and examine the resulting shock loci and post–shock flow variables. We investigate the differences arising from our two assumptions regarding the body pressure and the effect of boundary conditions on the resulting solutions. We also compare the findings of our numerical methods to those obtained from discrete element simulations.

We first apply our governing depth–averaged differential equations to the subcritical wedge where we expect to recover the straight shock solution. As noted in a prior section, the differential equations reduce to an algebraic system in this context; we retain the differential system here. To begin, roots of the energy equation (3.73) are numerically determined using MATLAB's `fzero()`. We select the root corresponding to the weak or strong solution depending on which case we seek. With known ν we employ MATLAB's `ode45()` solver to numerically integrate the three differential equations in p, u, δ. Although it is possible to use the jump conditions of Chapter 2 to determine boundary conditions on p and u, such accurate values are not necessary. Upon integration over sufficient wedge distance, the numerical solutions converge to their correct values which agree with those obtained from the algebraic jump condtions. Figure 3.3 shows the convergence of $u(\xi)$ and $p(\xi)$ divided by the algebraic solutions of the respective quantities. Over successive iterations of the solver, one may subsequently improve the boundary conditions p_0 and u_0 to obtain faster convergence. As for the boundary condition on the attached shock, by definition $\delta_0 = 0$. In practice we cannot specify this to be exactly zero due to the form of the differential equations with factors of $1/\delta$. However, as with u_0 and p_0, the value of this boundary condition is not essential to

obtain the appropriate shock inclination β with a sufficiently long integration. In a more general body geometry we do not expect attached shocks and therefore we do not seek to re–phrase the equations in a form that would amend the possibility of numerical problems associated with $1/\delta$ evaluations.

We omit plots of the subcritical wedge shocks but note observed differences in the solutions resulting from our two models of the body pressure. In the case of $p_b = p$ the numerical solution of the differential equations typically converges to a strong shock solution, even upon specifying a value of ν_w corresponding to the weak shock for known ν_1, T_1, V_1. The solution proceeds as if ν_w were in fact the strong shock area fraction resulting from different upstream conditions at the same θ. That is, it does not converge to the strong solution we expect given our wedge inclination and incoming flow. This issue is similarly encountered in the case where we model the body pressure as $p_b = 2p - p_2$. Given ν as a root of the energy equation, we converge to the correct branch of the solution, but only with an accurate estimate for the boundary conditions on u and p. Poorly specified boundary conditions lead to the same strong shock solution as with $p_b = p$ or result in imaginary roots of the cubic (3.140).

With algebraic solutions available for the subcritical wedge geometry, there is little need to apply our system of differential equations to such a case. However, for the curved bow shock about a wedge discussed in Section 2.5.3, our local anaysis of Chapter 2 does not provide a means to estimate the shape of the resulting shock. Here we apply our governing differential equations to this supercritical wedge. We first note that the equations were derived in a body oriented coordinate system (ξ, η). With a body such as a disk we are able to capture the full extent of the

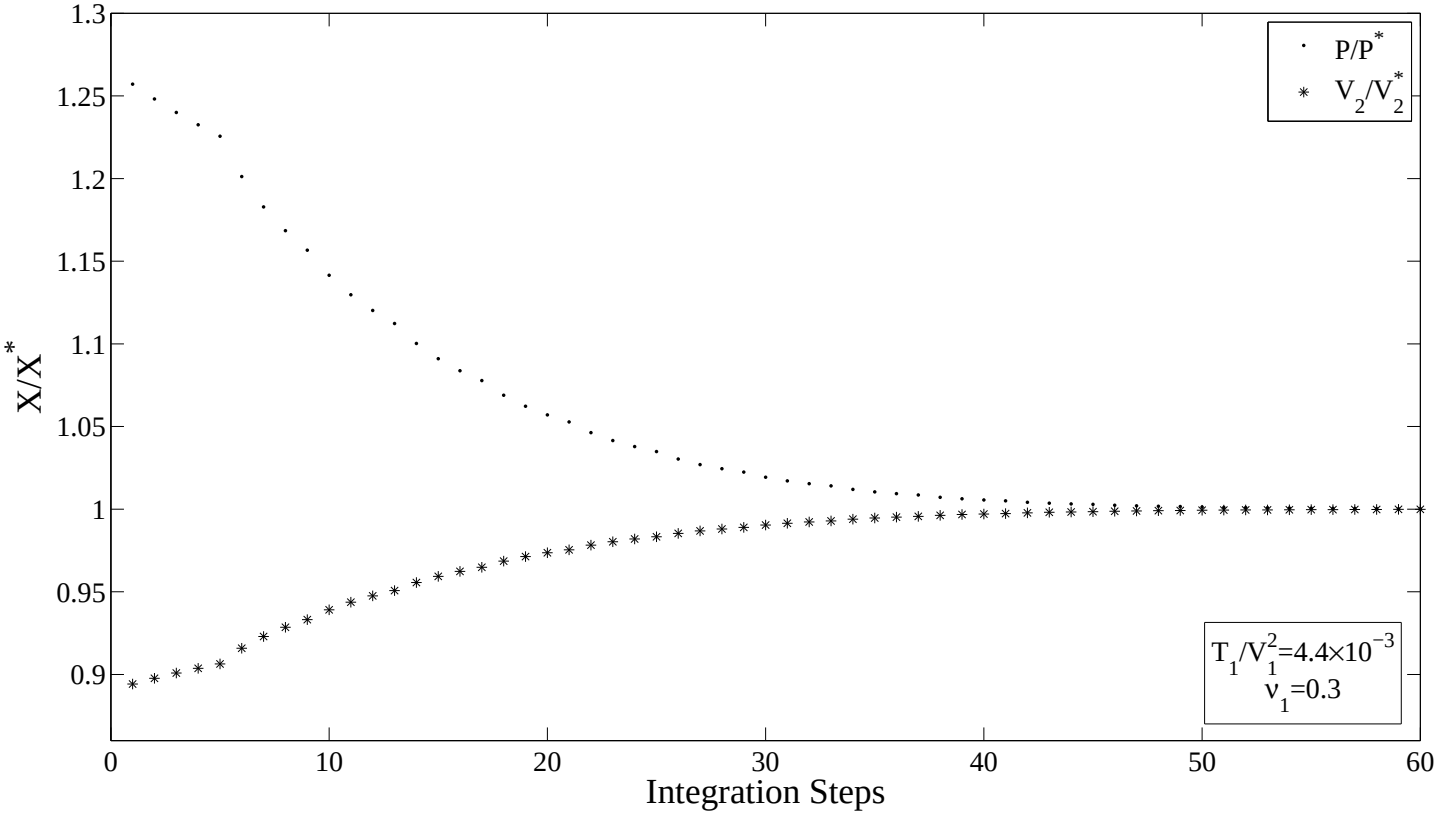

Figure 3.3: Convergence of numerical solutions for u and p to values obtained from jump conditions.

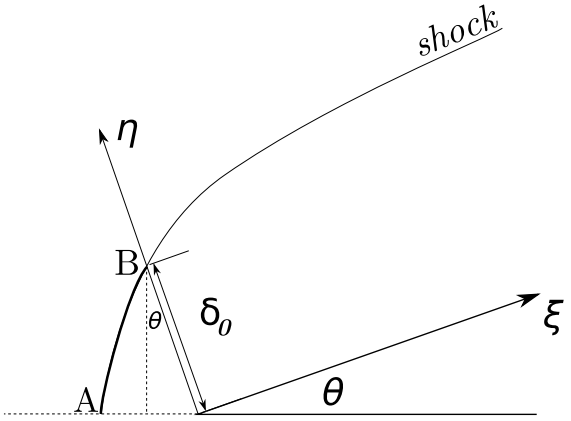

Figure 3.4: Bow shock geometry over supercritical wedge. By the construction of the differential equations we may only solve for shock position δ when $\xi \geq 0$.

shock front. We employ this geometry in Chapter 5. However, for the wedge geometry this treatment does not provide the ability to solve for the entire shock front in the case of a detached bow shock. Rather, we are obligated to neglect a portion of the shock from the horizontal to an inclination of $\pi/2 - \theta$ (from points A to B) as shown in Figure 3.4.

3.3.1 Boundary Conditions

The solution to our system of three differential equations requires appropriate boundary conditions for the variables p, δ, u. In addition, we must specify a value for the post–shock density ν. Recall that in our assumption of constant density we are solving the trivial expression $d\nu/d\xi = 0$ with the boundary condition ν. In the instance of a subcritical wedge where all gradients vanish, the energy equation provided an algebraic expression to determine ν. Without this simplification we may no longer obtain ν by use of the energy equation. Thus we seek an approximation for the boundary conditions of interest. We examine the portion of the

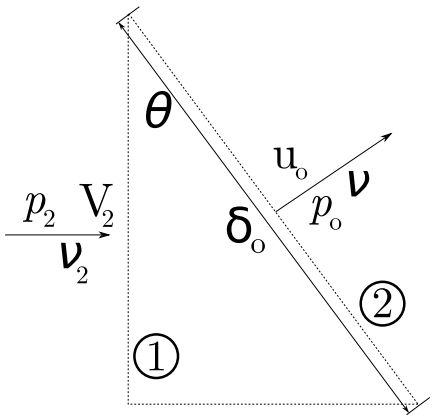

Figure 3.5: Control surface for determination of approximate boundary conditions

shocked region upstream of $\xi = 0$. See Figure 3.5.

Suggested by the qualitative shape of the bow shock and the small change in post–shock flow properties (such as ν_2) associated with β values approaching $\pi/2$ (Figure 3.2), we analyze the control volume depicted in Figure 3.5, an expanded portion of Figure 3.4. We approximate the unknown curve with a normal shock of height $\delta_0 \cos\theta$, across which upstream properties change in accordance with the algebraic jump conditions, thus determining the state of flow entering our control surface. We then perform balances of mass and momentum on this surface to obtain approximate boundary conditions for the solution of our differential equation system.

For the change across the normal shock we employ the jump equations of Chap-

ter 2. We recall the cubic expression (2.95) with $\sin^2\beta = 1$

$$\begin{aligned}\left[16(1-\nu_1)^2 + 4\Sigma(9\nu_1^2 - 16\nu_1 + 16)\right]\nu_2^3 - \\ - \left[272\nu_1(1-\nu_1)^2 + 32\Sigma(7\nu_1 + 2\nu_1^2)\right]\nu_2^2 + \\ + \left[128(1-\nu_1)^2(1+4\nu_1) + 64\Sigma(\nu_1^2+8)\right]\nu_2 - \\ - \left[384\nu_1(1-\nu_1)^2\right] = 0 \end{aligned} \tag{3.141}$$

With this expression solved for ν_2 we use the remaining normal–shock jump equations to determine V_2 and T_2 (or p_2).

Mass Balance

In a steady, fully–developed state our mass flux across the control surface is balanced,

$$\int_A \rho u_\alpha n_\alpha dA = 0$$

For sides ① and ② of length $\delta_0 \cos\theta$ and δ_0, respectively, we have the average velocity perpendicular to the surface. Our density is treated as constant, consistent with the assumption of our governing differential equations. By a physical boundary or by a condition of symmetry we treat the bottom surface as free of mass flux. The balance of mass flux is,

$$\nu_2 V_2 \delta_0 \cos\theta = \nu_2 u_0 \delta_0$$

which gives us an approximate boundary condition on the speed u,

$$u(\xi = 0) = u_0 = V_2 \cos\theta \tag{3.142}$$

Momentum Balance

Similarly, we balance the momentum in the horizontal direction according to

$$\int_A \rho u_\alpha u_\gamma n_\gamma dA = \int_A \tau_{\alpha\gamma} n_\gamma dA$$

with our usual inviscid stress tensor $\tau = -p\mathbf{I}$, we have an expression for an approximate pressure boundary condition,

$$p_0 = p(\xi = 0) = \rho_2 V_2^2 + p_2 - \rho_2 u_0^2 = 0 \tag{3.143}$$

The designation of a normal shock approximation to the unknown curve connecting points A and B in Figure 3.4 is naturally not the only choice for obtaining our boundary conditions. In Figure 3.6 we plot the resulting shocks given by 65° and 90° assumptions and note their relative agreement.

Note that the mass and momentum considerations do not give any evidence for a boundary condition on the shock thickness δ_0. As we recall from Section 2.5.3, there is an apparent length scale for the supercritical wedge due to effect of wedge size on the detachment distance of the bow shock.

3.3.2 Results

In Figure 3.7 we compare the solution of our differential equations with an image from a discrete element simulation under the same prescribed upstream conditions. We employ the pressure model of Section 3.2.3 where $p_b = 2p - p_2$. The solution for $\delta(\xi)$ is plotted with the solid black line and the shock front is apparent by the visual change in area fraction. The boundary condition on shock thickness δ_0 is fit by

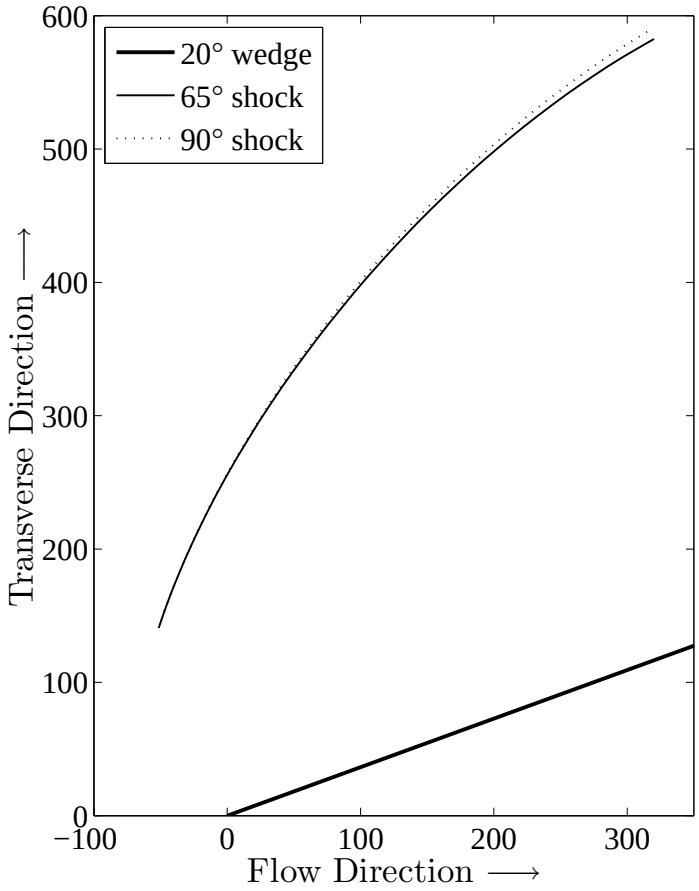

Figure 3.6: Comparison of ODE solutions for varied bow shock approximations. The 65° curve represents the resulting shock locus if points A ane B in Figure 3.4 are connected by a 65° line. Similar for the normal (90°) curve.

inspection. We note the relative agreement between the model and simulation– the difference at the rear edge of the domain (right side) is several particle diameters (pd) over an integration distance of approximately $\xi = 85$pd. Shock thickness varies from $\sim$75 to over 200pd. Relative error in our model is comparable to that of the algebraic jump conditions employed to determine changes across straight attached shocks over subcritical wedges (see Figure 2.14). Improvement of the jump conditions with simulation (e.g. with T redefined as mentioned in Section 2.5.2) indeed leads to closer agreement between the locus of the shock fronts.

In Figure 3.8 we plot the results obtained from our two body–pressure approximations and note their difference along the entire range of ξ. The agreement with simulation displayed by Figure 3.7 suggests that the simple $p_b = p$ model is not correctly characterizing the pressure at the body and across the shock depth. For the remaining results we therefore use $p_b = 2p - p_2$.

Figures 3.9 and 3.11 plot the depth–averaged speed $u(\xi)$ and pressure $p(\xi)$ for wedge angles of 15° and 20°. We normalize the values by their respective upstream quantities V_1 and p_1. Shock offset boundary condition (δ_0) values were determined by fitting with simulation images. We note that the wedges have the effect of decreasing the speed and increasing the pressure with respect to the upstream values. For the wedge angles studied, these curves are characteristic– after the initial change by passage through the shock, the speed and pressure vary with ξ in the shown qualitative manner. Figure 3.10 confirms this with a plot of the velocity field for a bow shock over a 20° wedge. Yellow and red vectors denote higher speeds, green and blues denote lower. The interface between the bow shock and the upstream flow is clearly marked by the difference in the average color. Note that over the length of the wedge, the color "warms" to approach yellow, indicating increasing speed.

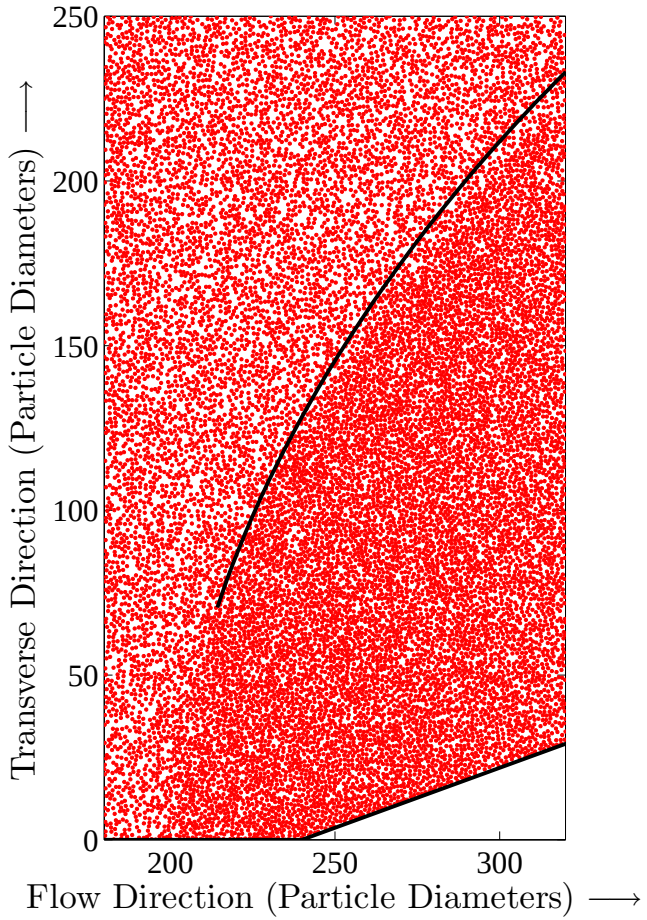

Figure 3.7: Simulation image at 20° with overlay of ODE solution for $\delta(\xi)$. $\nu_1 = 0.3$, $\Sigma = 4.4 \times 10^{-3}$. Boundary condition δ_0 set by fitting to image. Pressure model $p_b = 2\overline{p} - p_2$ used in ODE system.

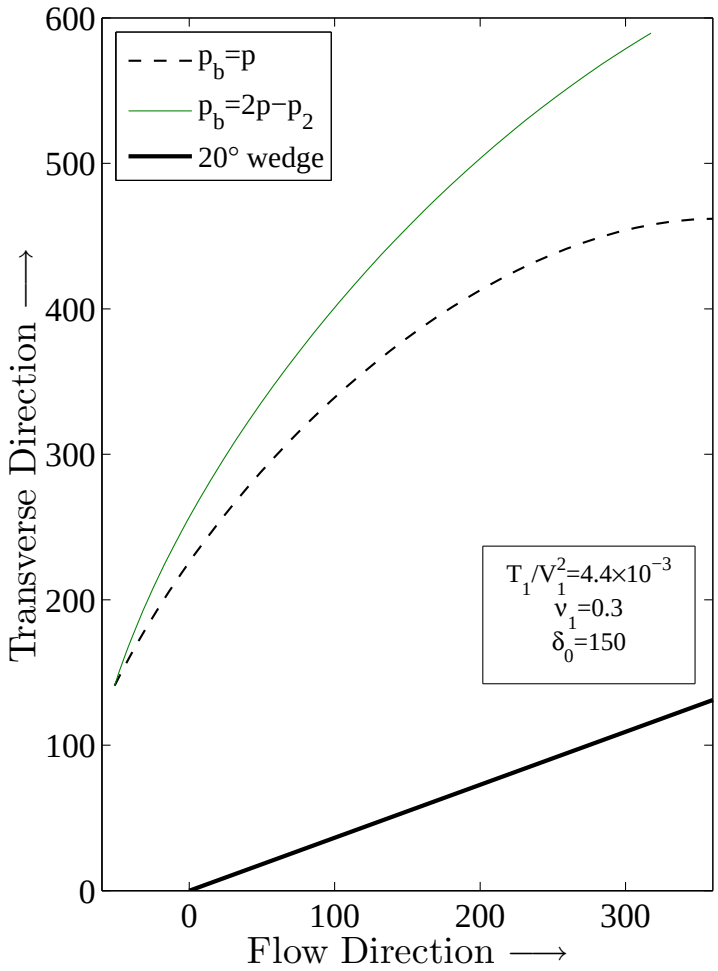

Figure 3.8: Comparison of ODE solution of $\delta(\xi)$ for $p_b = p$ and $p_b = 2p - p_2$.

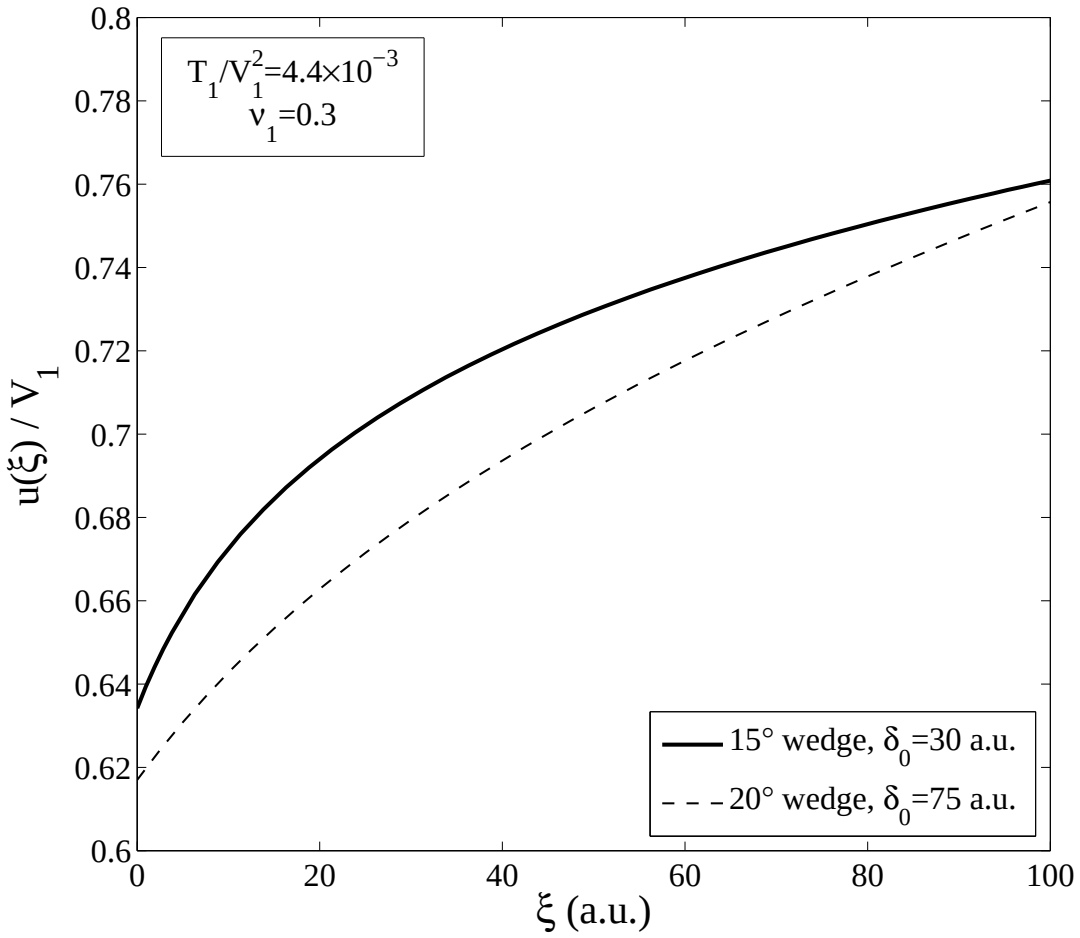

Figure 3.9: Depth–averaged speed $u(\xi)$ for wedge angles of 15° and 20°. Shock thickness boundary condition δ_0 is set by inspection of simulation images.

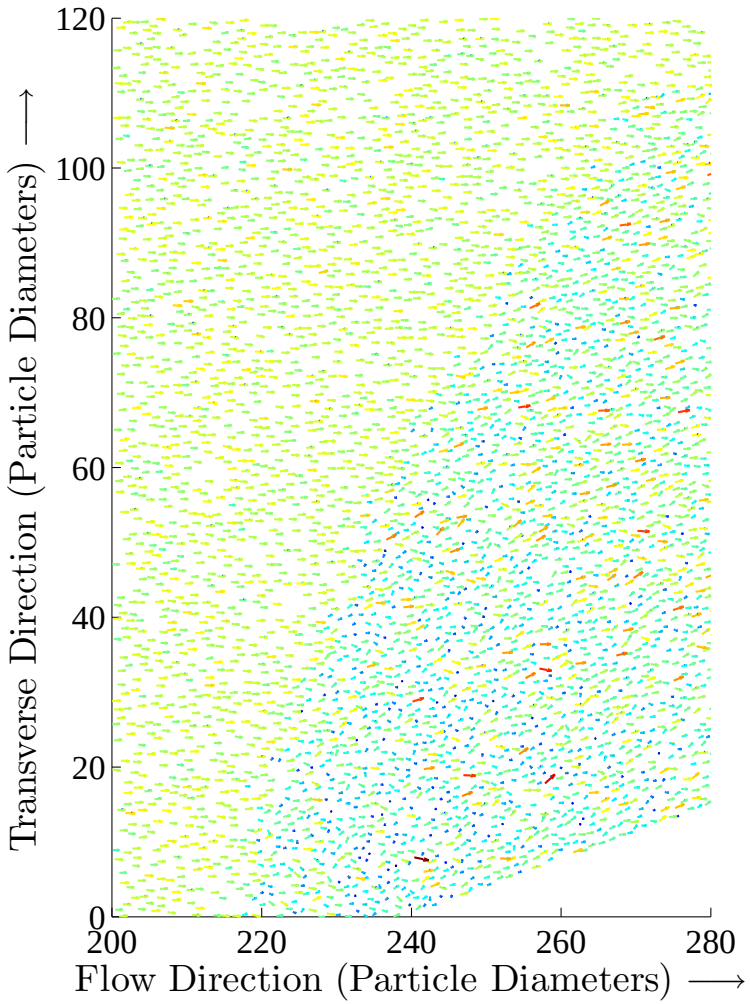

Figure 3.10: Velocity field for bow shock over 20° wedge. Yellow and red represent higher speeds, blue and green lower.

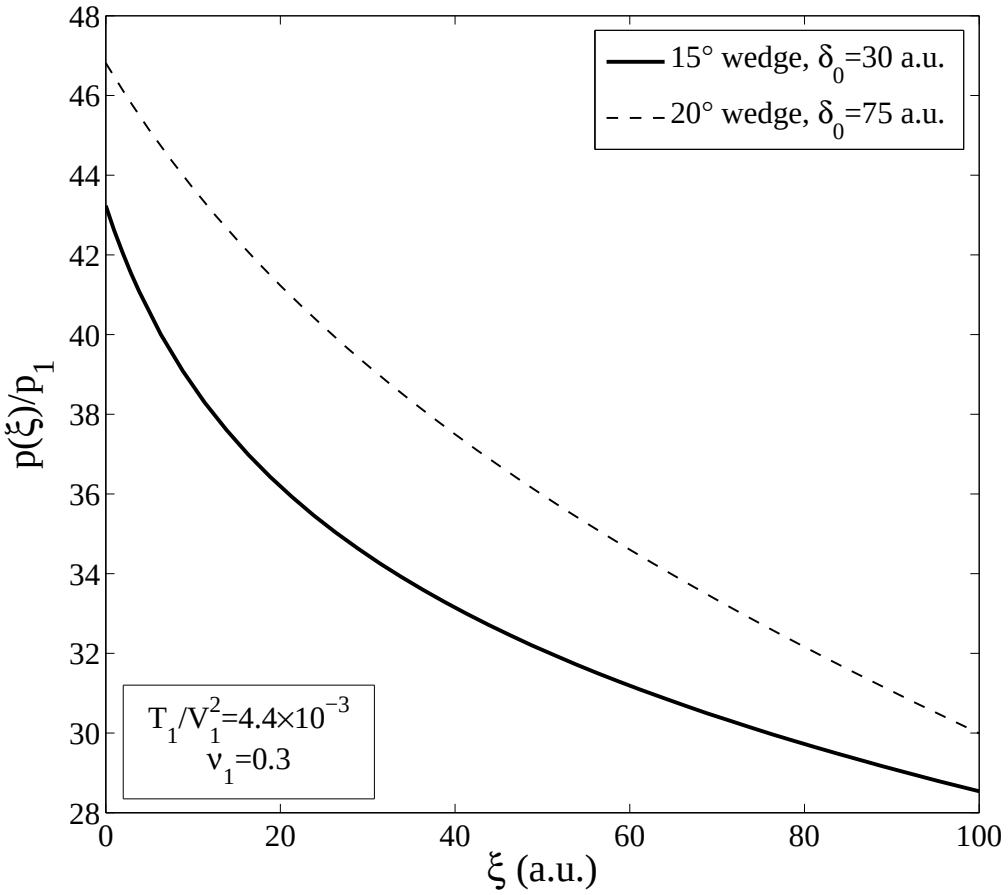

Figure 3.11: Depth–averaged pressure $p(\xi)$ for wedge angles of 15° and 20°. Shock thickness boundary condition δ_0 is set by inspection of simulation images.

Figure 3.12 plots shock solutions for various boundary condition δ_0. We note that solutions are qualitatively similar for the largest three values. For $\delta_0 = 100$ particle diameters we see the shock curve towards the body near the right side of the domain, which is inconsistent with observations of detached bow shocks from our simulations. Upon further reduction of δ_0 we no longer obtain real solutions– at $\xi \approx 210$pd note the turn in the curve corresponding to $\delta_0 = 50$pd. The remaining portion of the curve plots only the real component of the solution.

It might be of interest to plot the solutions for situations where upstream conditions Σ and ν_1 are varied. However, without knowledge of appropriate δ_0 values, such plots are not particularly useful. Altering upstream conditions while maintaining the same δ_0 is not an accurate characterization of the shock behavior– changes in upstream conditions are accompanied by changes in the offset and hence δ_0.

3.4 Conclusions

In this chapter we employed our usual transport equations to derive shock depth–averaged differential equations for the shock thickness δ, body–tangential speed u, and pressure p over general bodies. To obtain numerical solutions for our differential equations we adopted several assumptions: constant post–shock density ν, zero average velocity normal to the body, and we employed two models to relate the depth–averaged pressure p and body pressure p_b. This allowed us to neglect the relatively cumbersome differential equation resulting from the energy balance. For the case of the straight wedge, it was found that our equations and subsequent simplifications were in good agreement with simulations. It remains to see whether the equations are as applicable for more general bodies. It is possible that the inherent assumptions may only be properly applied to specific geometries. In

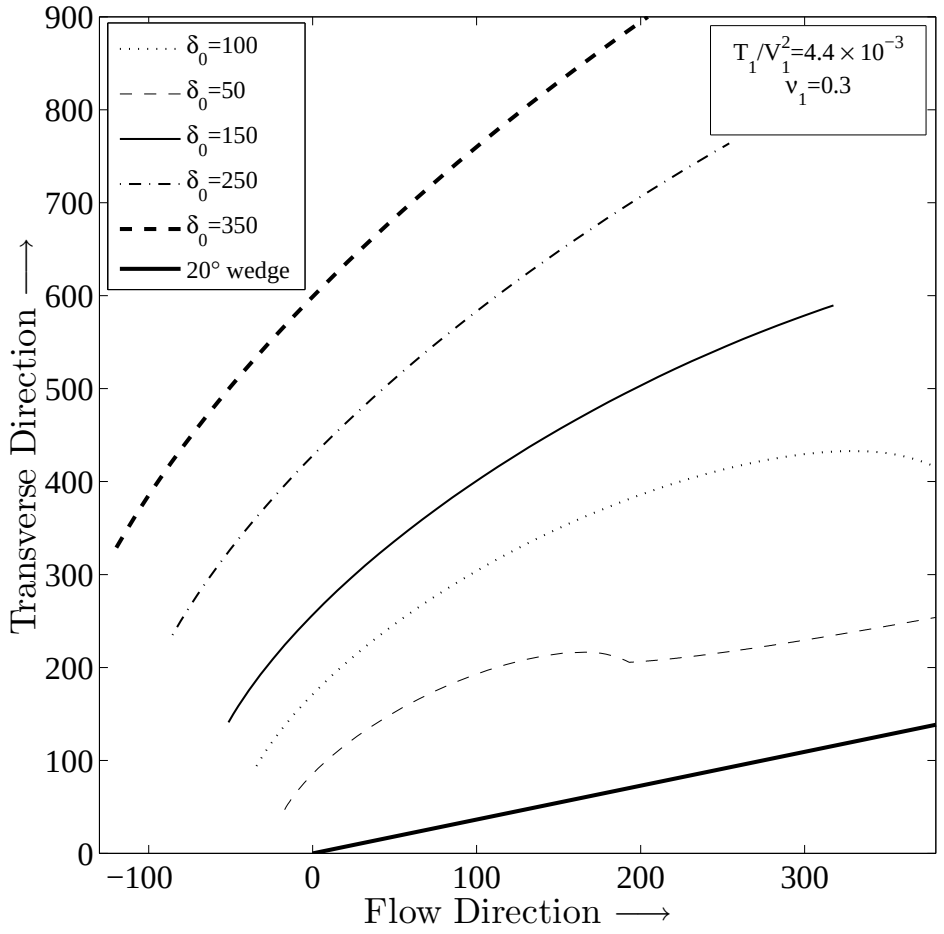

Figure 3.12: ODE solution for $\delta(\xi)$ with varied boundary condition δ_0. Note that for $\delta_0 = 50$a.u. the solution becomes complex where the shock front changes direction abruptly.

Chapter 5 we investigate the application of the governing differential equations for a circular body in shear flow. It may also be of interest to remove the assumption of constant density and make use of the energy equation for possibly improved predictions. Finally, while we were able to obtain reasonable assumptions for boundary conditions on u and p, the boundary condition on shock detachment δ remains a fitting parameter. Further study illuminating the relation between obstructing body length scales (e.g. wedge opening distance $L \sin \theta$) and bow shock detachment could remove the need for simulations to supply this parameter.

CHAPTER 4

SATURN'S PROPELLERS

4.1 Introduction

Saturn's rings are composed of water ice particles with an approximate power–law size distribution ranging from 10^{-2}m to meters [39]. They also contain fewer larger bodies on the order of 10 meters (moonlets). Differing from the larger moons which open gaps in the rings (e.g. Encke Gap via Pan), these smaller moonlets are believed to be responsible for the formation of propeller–shaped density features, referred to as propellers. Due to the inability to resolve the moonlets in satellite images, investigations of the propellers attempt to infer the body's size indirectly through their disturbance of the ring material. Propellers may also provide additional information on the particle size distribution in the rings.

To date, there have been several studies of propeller formation. Spahn and Sremčević [30] applied a viscous continuum model to numerically examine density disturbances due to a perturbing body. In their treament, the ring is composed of two portions– a scattering region and a mean Keplerian flow. The gravitational influence of the moonlet is restricted to a line at the moonlet's azimuthal location and the scattering is modeled as a Markov process. The flux of scattered particles provides a boundary condition for the viscous transport to the mean flow. Sremčević *et al.* [32] also employed this model, using Green's functions to solve the diffusion–type boundary value problem. Both studies considered energetic effects to be of minor importance with respect to mass and momentum transport. More recently, Seiß et al. [28] conducted two–dimensional N–body simulations of uniform, inelastic particles at a restitution coefficient of $e = 0.5$. They found the

azimuthal–averaged optical depth of the propellers scaled well with the Hill radius in the radial direction and the azimuthal extent of the features correlated with moonlet mass and ring viscosity. It is worth noting that observation of such scaling laws have been confirmed by some [31] and not found by others [34]. Lewis and Stewart [21] furthered the complexity of these numerical studies, employing a three–dimensional N–body simulation that included both particle size distributions and self–gravity. As well as looking at these additional effects on propeller formation, they examined particle clustering about the moonlet and accretion in the sheared flow.

A feature common to all prior work has been the inclusion of the moonlet as a gravitationally perturbing body. None of the aforementioned studies have examined the problem in the absence of moonlet gravity, creating a purely collisional system under the sole guidance of Saturn's tidal forces. We do not argue against the importance of gravitational effects in a realistic model, but present here a different perspective on propeller formation, motivated by phenomena observed in granular flow without attractive potentials.

Similar to the behavior of supersonic compressible gases, granular systems can also experience spatially rapid changes in its properties (shock) when flow speed exceeds that of the sound speed in the material. Granular shock has been investigated in simple geometries both experimentally [10, 25] and numerically [25], but only limited analytical work has been performed [10, 12]. Using an adapted kinetic theory for plane flows of inelastic, frictionless disks, we derive an expression for the velocity fluctuation (granular temperature) in shear flow. Following this, we employ elements of equilibrium thermodynamics to arrive at a relation for the sound

speed as a function of this temperature and packing fraction. It is shown that for observed planar ring densities (e.g. in the Saturnian A–ring) incident flows upon the moonlet are predominantly supersonic, and the hallmark propeller feature may in fact be the locus of a detached bow shock.

4.2 Simulation

To numerically simulate the problem, a two–dimensional N–body simulation of identical, frictionless, circular disks was developed without moonlet and interparticle gravitation.

4.2.1 Methodology

We denote the diameter of the simulation particles as d. Defining the vector $\mathbf{g} \equiv \mathbf{c}_1 - \mathbf{c}_2$ as the relative velocity of a pair of particles, interactions are treated as instantaneous binary collisions with energy dissipation modeled via constant restitution coefficient, e.

$$g'_\alpha k_\alpha = -e g_\alpha k_\alpha \tag{4.1}$$

where the unit vector $\mathbf{k}$ defines the direction from the center of particle 1 to the center of particle 2 and the prime denotes a post–collision quantity. Vector components (denoted with Greek indices) are given with respect to a set of orthogonal basis vectors in the plane and we sum over a repeated index. The restitution coefficient ranges from 0 to 1, the latter of which describes a perfectly elastic interaction. In addition to the collision model we have an expression of conservation of linear momentum,

$$\mathbf{c}_1 + \mathbf{c}_2 = \mathbf{c}'_1 + \mathbf{c}'_2 \tag{4.2}$$

With (4.1) and (4.2) we can write the post–collisional velocities as,

$$c'_{1\alpha} = c_{1\alpha} - \left(\frac{1+e}{2}\right) g_\beta k_\beta k_\alpha \tag{4.3}$$

$$c'_{2\alpha} = c_{2\alpha} + \left(\frac{1+e}{2}\right) g_\beta k_\beta k_\alpha \tag{4.4}$$

Because the particles are frictionless, particle rotations are not considered. Due to the collisional nature of the granular gas, the neglect of tangential forces is a reasonable simplification.

4.2.2 Governing Equations of Motion– The homogeneous Hill Equations

Particle Accelerations

In our simulations, we fix the origin of a translating and rotating reference frame to the moonlet. We define unit vectors $\hat{\mathbf{e}}_r$, $\hat{\mathbf{e}}_t$, and $\hat{\mathbf{e}}_b$ corresponding to directions toward Saturn, tangent to the circular orbit, and out of the plane, respectively (defined such that $\hat{\mathbf{e}}_t \times \hat{\mathbf{e}}_r = \hat{\mathbf{e}}_b$). See Figure 4.1. Our local coordinates x and y coincide with $\hat{\mathbf{e}}_t$ and $\hat{\mathbf{e}}_r$, respectively. A general acceleration in this frame can be expressed as

$$\mathbf{a} = \ddot{\mathbf{R}} + \dot{\omega} \times \rho + \omega \times (\omega \times \rho) + \ddot{\rho} + 2\omega \times \dot{\rho} \tag{4.5}$$

where $\mathbf{R}$ is a position vector from Saturn to the moonlet, ρ is a position vector for a point of interest *relative* to the moonlet, and ω is the rotation rate of the moving coordinate system. We assume that the moonlet is moving in a circular orbit of radius R at constant angular speed Ω. Thus, the first term representing

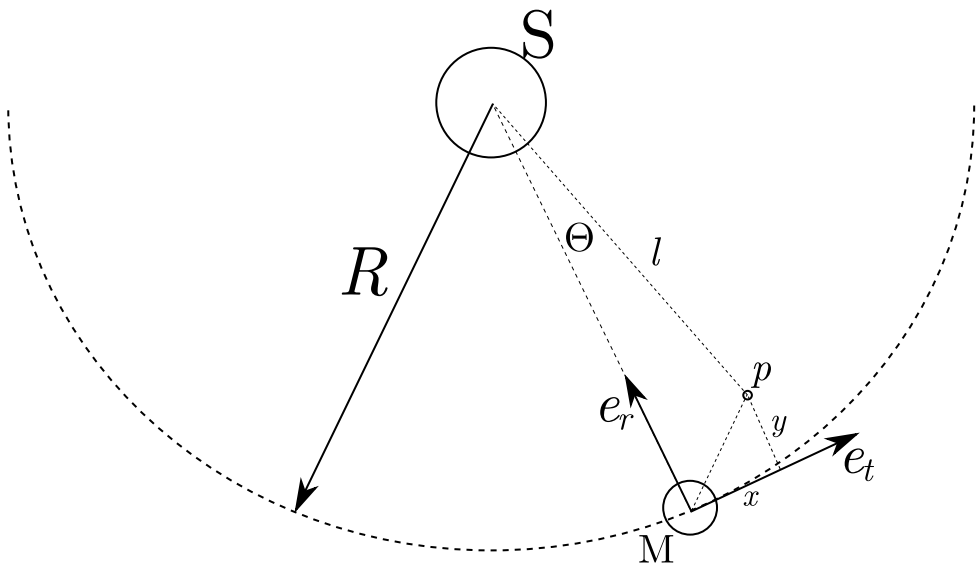

Figure 4.1: Geometry of ($\hat{\mathbf{e}}_r$,$\hat{\mathbf{e}}_t$) coordinate system with origin at moonlet M

the acceleration of the reference frame is simply $\ddot{\mathbf{R}} = \Omega^2 R\hat{\mathbf{e}}_r$. Other terms are, $\omega = \Omega\hat{\mathbf{e}}_b$, $\rho = x\hat{\mathbf{e}}_t + y\hat{\mathbf{e}}_r$, $\dot{\omega} = 0$, $\dot{\rho} = u\hat{\mathbf{e}}_t + v\hat{\mathbf{e}}_r$, and $\ddot{\rho} = \dot{u}\hat{\mathbf{e}}_t + \dot{v}\hat{\mathbf{e}}_r$. It is emphasized that $x, y, u, v, \dot{u}, \dot{v}$ are positions, speeds and accelerations relative to the moving system. These are the quantities of interest in our simulations. Equation (4.5) becomes,

$$\begin{aligned}\mathbf{a} = \Omega^2 R\hat{\mathbf{e}}_r + \Omega\hat{\mathbf{e}}_b \times (\Omega\hat{\mathbf{e}}_b \times (x\hat{\mathbf{e}}_t + y\hat{\mathbf{e}}_r)) + \\ +(\dot{u}\hat{\mathbf{e}}_t + \dot{v}\hat{\mathbf{e}}_r) + 2\Omega\hat{\mathbf{e}}_b \times (u\hat{\mathbf{e}}_t + v\hat{\mathbf{e}}_r)\end{aligned} \tag{4.6}$$

which evaluates to,

$$\mathbf{a} = \left(\Omega^2(R-y) + \dot{v} + 2\Omega u\right)\hat{\mathbf{e}}_r + \left(\dot{u} - x\Omega^2 - 2\Omega v\right)\hat{\mathbf{e}}_t \tag{4.7}$$

The Orbital Speed

To determine the angular speed Ω of the moonlet (mass m_m) about Saturn (mass m_s), we write a radial force balance on the moonlet,

$$m_m \Omega^2 R = \frac{\mathfrak{G} m_s m_m}{R^2} \tag{4.8}$$

where $\mathfrak{G}$ is the gravitational constant. Thus we have

$$\Omega^2 = \frac{\mathfrak{G} m_s}{R^3} \tag{4.9}$$

Linear Momentum Balance

We perform a balance of linear momentum on a particle of mass m_p at location p given by coordinates (x, y). At a distance l from Saturn (mass m_s), we have a gravitational force of,

$$\mathbf{F} = \frac{\mathfrak{G} m_p m_s}{l^2} \hat{\mathbf{r}} \tag{4.10}$$

where $\hat{\mathbf{r}}$ is a unit vector from the particle's location towards Saturn. Note that we neglect any gravitational forces due to the moonlet. In terms of our local unit vectors, this can be expressed as,

$$\mathbf{F} = \frac{\mathfrak{G} m_p m_s}{(R-y)^2 + x^2} \hat{r} = \frac{\mathfrak{G} m_p m_s}{(R-y)^2 + x^2} (\cos\Theta \hat{\mathbf{e}}_r - \sin\Theta \hat{\mathbf{e}}_t) \tag{4.11}$$

where

$$\tan\Theta = \frac{x}{R-y} \tag{4.12}$$

Equation (4.12) can be used to express $\hat{\mathbf{r}}$ as,

$$\hat{\mathbf{r}} = \frac{1}{\sqrt{x^2 + (R-y)^2}} \left[(R-y)\hat{\mathbf{e}}_r - x\hat{\mathbf{e}}_t \right] \tag{4.13}$$

Thus, in the radial and tangential directions, the force balances are respectively,

$$\Omega^2 (R-y) + \dot{v} + 2\Omega u = \frac{\mathfrak{G} m_s (R-y)}{[x^2 + (R-y)^2]^{3/2}} \tag{4.14}$$

$$\dot{u} - \Omega^2 x - 2\Omega v = -\frac{\mathfrak{G} m_s x}{[x^2 + (R-y)^2]^{3/2}} \tag{4.15}$$

The radial equation

Consider the radial force balance,

$$\Omega^2(R-y)+\dot{v}+2\Omega u=\frac{\mathfrak{G}m_s(R-y)}{[x^2+(R-y)^2]^{3/2}} \tag{4.16}$$

we divide by R and define $\tilde{y}=y/R$ and $\tilde{x}=x/R$

$$\Omega^2(1-\tilde{y})+\frac{\dot{v}}{R}+\frac{2\Omega u}{R}=\frac{\mathfrak{G}m_s(1-\tilde{y})}{R^3[\tilde{x}^2+(1-\tilde{y})^2]^{3/2}} \tag{4.17}$$

Denote the right hand side as $f(\tilde{x},\tilde{y})$. We take an expansion of this about ($\tilde{x}=0,\tilde{y}=0$). In general, the expansion is,

$$f(\tilde{x},\tilde{y})=f(0,0)+(\tilde{x}-0)\frac{\partial f}{\partial\tilde{x}}(0,0)+(\tilde{y}-0)\frac{\partial f}{\partial\tilde{y}}(0,0)+\ldots \tag{4.18}$$

The partial derivatives are,

$$\frac{\partial f}{\partial\tilde{x}}=\frac{-3\mathfrak{G}m_s\tilde{x}(1-\tilde{y})}{R^3[\tilde{x}^2+(1-\tilde{y})^2]^{5/2}} \tag{4.19}$$

$$\frac{\partial f}{\partial\tilde{y}}=\frac{\mathfrak{G}m_s[2(1-\tilde{y})^2-\tilde{x}^2]}{R^3[\tilde{x}^2+(1-\tilde{y})^2]^{5/2}} \tag{4.20}$$

Evaluating at $(0,0)$,

$$f(\tilde{x},\tilde{y})=f(0,0)+(\tilde{x}-0)\cancel{\frac{\partial f}{\partial\tilde{x}}(0,0)}^{\,0}+(\tilde{y}-0)\frac{\partial f}{\partial\tilde{y}}(0,0)+\ldots \tag{4.21}$$

$$f(\tilde{x},\tilde{y})=\frac{\mathfrak{G}m_s}{R^3}(1+2\tilde{y}) \tag{4.22}$$

To first order, the radial balance of linear momentum is,

$$\Omega^2(1-\tilde{y})+\frac{\dot{v}}{R}+\frac{2\Omega u}{R}=\frac{\mathfrak{G}m_s}{R^3}(1+2\tilde{y}) \tag{4.23}$$

Using Equation (4.9) for the orbital speed we have,

$$-3\Omega^2\tilde{y}+\frac{\dot{v}}{R}+\frac{2\Omega u}{R}=0 \tag{4.24}$$

which can be written as,

$$\frac{d^2y}{dt^2}+2\Omega\frac{dx}{dt}-3\Omega^2y=0 \tag{4.25}$$

The azimuthal equation

Consider the azimuthal force balance,

$$\dot{u} - \Omega^2 x - 2\Omega v = -\frac{\mathfrak{G} m_s x}{[x^2 + (R-y)^2]^{3/2}} \tag{4.26}$$

again we divide by R and define $\tilde{y} = y/R$ and $\tilde{x} = x/R$

$$\frac{\dot{u}}{R} - \Omega^2 \tilde{x} - \frac{2\Omega v}{R} = -\frac{\mathfrak{G} m_s \tilde{x}}{R^3[\tilde{x}^2 + (1-\tilde{y})^2]^{3/2}} \tag{4.27}$$

Denote the right hand side as $g(\tilde{x}, \tilde{y})$ and expand about $(\tilde{x} = 0, \tilde{y} = 0)$. The partial derivatives for the expansion are,

$$\frac{\partial g}{\partial \tilde{x}} = \frac{\mathfrak{G} m_s (2\tilde{x}^2 - (1-\tilde{y})^2)}{R^3[\tilde{x}^2 + (1-\tilde{y})^2]^{5/2}} \tag{4.28}$$

$$\frac{\partial g}{\partial \tilde{y}} = \frac{-3\mathfrak{G} m_s x (1-\tilde{y})}{R^3[\tilde{x}^2 + (1-\tilde{y})^2]^{5/2}} \tag{4.29}$$

Evaluating at $(0, 0)$,

$$g(\tilde{x}, \tilde{y}) = g(0,0) + (\tilde{x} - 0)\frac{\partial g}{\partial \tilde{x}}(0,0) + (\tilde{y} - 0)\cancelto{0}{\frac{\partial g}{\partial \tilde{y}}(0,0)} + \ldots \tag{4.30}$$

$$g(\tilde{x}, \tilde{y}) = -\frac{\mathfrak{G} m_s}{R^3}\tilde{x} \tag{4.31}$$

To first order the azimuthal linear momentum balance is,

$$\frac{\dot{u}}{R} - \Omega^2 \tilde{x} - \frac{2\Omega v}{R} = -\frac{\mathfrak{G} m_s \tilde{x}}{R^3} \tag{4.32}$$

Again using Equation (4.9) for Ω we have,

$$\frac{\dot{u}}{R} - \Omega^2 \tilde{x} - \frac{2\Omega v}{R} = -\Omega^2 \tilde{x} \tag{4.33}$$

so that we may write,

$$\frac{d^2 x}{dt^2} - 2\Omega \frac{dy}{dt} = 0 \tag{4.34}$$

The Hill Equations

For a simulation particle at location (x, y) with corresponding velocity components (u, v), particle dynamics are governed by Equations (4.25) and (4.34),

$$\frac{d^2y}{dt^2} + 2\Omega\frac{dx}{dt} - 3\Omega^2 y = 0 \tag{4.35}$$

$$\frac{d^2x}{dt^2} - 2\Omega\frac{dy}{dt} = 0 \tag{4.36}$$

In the absence of gravitational forces from the moonlet the Hill Equations are homogeneous and permit an analytical solution. We write as a first–order system of coupled differential equations

$$\begin{aligned} \dot{x} &= u \\ \dot{y} &= v \\ \dot{u} = \ddot{x} &= 2\Omega\dot{y} = 2\Omega v \\ \dot{v} = \ddot{y} &= 3\Omega^2 y - 2\Omega\dot{x} = 3\Omega^2 y - 2\Omega u \end{aligned}$$

With this we write the first order system in the form $\dot{\mathbf{z}} = \mathbf{A}\mathbf{z}$

$$\begin{bmatrix} \dot{x} \\ \dot{y} \\ \dot{u} \\ \dot{v} \end{bmatrix} = \begin{bmatrix} 0 & 0 & 1 & 0 \\ 0 & 0 & 0 & 1 \\ 0 & 0 & 0 & 2\Omega \\ 0 & 3\Omega^2 & -2\Omega & 0 \end{bmatrix} \begin{bmatrix} x \\ y \\ u \\ v \end{bmatrix} \tag{4.37}$$

The coefficient matrix has the characteristic equation $\lambda^4 + \Omega^2\lambda^2 = 0$, so the eigenvalues are $\lambda = 0$ (with algebraic multiplicity 2) and the conjugate pair $\lambda = \pm\imath\Omega$. To obtain a pair of linearly independent eigenvectors from the repeated eigenvalue, we use the concept of the generalized eigenvector and the fundamental matrix $e^{\mathbf{A}t}$.

A solution of $(\mathbf{A} - \lambda\mathbf{I})\mathbf{q}_1 = 0$ for $\lambda = 0$ is,

$$(\mathbf{A} - \cancel{\lambda}^{0}\mathbf{I})\mathbf{q}_1 = 0$$

$$\mathbf{A}\mathbf{q}_1 = 0 \rightarrow \mathbf{q}_1 = \begin{bmatrix} a \\ 0 \\ 0 \\ 0 \end{bmatrix} \tag{4.38}$$

where a is a free variable. The solution associated with this eigenvector is,

$$\mathfrak{z}_1(t) = e^{\lambda t}\mathbf{q}_1 = \mathbf{q}_1 \tag{4.39}$$

.

To find the second linearly independent eigenvector associated with $\lambda = 0$, we find the vector $\mathbf{q}_2$ that solves $(\mathbf{A} - \lambda\mathbf{I})^2\mathbf{q}_2 = 0$:

$$(\mathbf{A} - \cancel{\lambda}^{0}\mathbf{I})^2\mathbf{q}_2 = 0$$

$$\mathbf{A}^2\mathbf{q}_2 = 0 \rightarrow \mathbf{q}_2 = \begin{bmatrix} b \\ c \\ \frac{3}{2}\Omega c \\ 0 \end{bmatrix} \tag{4.40}$$

where again, b and c are free variables. The solution associated with this vector is,

$$\mathfrak{z}_2(t) = e^{\mathbf{A}t}\mathbf{q}_2 = e^{\lambda t}\left[\mathbf{q}_2 + t(\mathbf{A} - \lambda\mathbf{I})\mathbf{q}_2\right]$$

$$\mathfrak{z}_2(t) = \begin{bmatrix} b \\ c \\ \frac{3}{2}\Omega c \\ 0 \end{bmatrix} + t \begin{bmatrix} 0 & 0 & 1 & 0 \\ 0 & 0 & 0 & 1 \\ 0 & 0 & 0 & 2\Omega \\ 0 & 3\Omega^2 & -2\Omega & 0 \end{bmatrix} \begin{bmatrix} b \\ c \\ \frac{3}{2}\Omega c \\ 0 \end{bmatrix}$$

$$\mathfrak{z}_2(t) = \begin{bmatrix} b \\ c \\ \frac{3}{2}\Omega c \\ 0 \end{bmatrix} + t \begin{bmatrix} \frac{3}{2}\Omega c \\ 0 \\ 0 \\ 0 \end{bmatrix} = \begin{bmatrix} b + \frac{3}{2}\Omega ct \\ c \\ \frac{3}{2}\Omega c \\ 0 \end{bmatrix} \tag{4.41}$$

Following this we calculate eigenvectors $\mathbf{q}_3$ and $\mathbf{q}_4$ for $\lambda = \imath\Omega$ and $\lambda = -\imath\Omega$, respectively. These have the form,

$$\mathbf{q}_3 = \begin{bmatrix} -2\imath \\ 1 \\ 2\Omega \\ \imath\Omega \end{bmatrix}, \qquad \mathbf{q}_4 = \begin{bmatrix} +2\imath \\ 1 \\ 2\Omega \\ -\imath\Omega \end{bmatrix} \tag{4.42}$$

The solutions of the original system associated with the complex eigenvales are,

$$\mathfrak{z}_3(t) = d_1 \cos\Omega t \begin{bmatrix} 0 \\ 1 \\ 2\Omega \\ 0 \end{bmatrix} - d_1 \sin\Omega t \begin{bmatrix} -2 \\ 0 \\ 0 \\ \Omega \end{bmatrix} = d_1 \begin{bmatrix} 2\sin\Omega t \\ \cos\Omega t \\ 2\Omega\cos\Omega t \\ -\Omega\sin\Omega t \end{bmatrix} \tag{4.43}$$

$$\mathfrak{z}_4(t) = d_2 \sin\Omega t \begin{bmatrix} 0 \\ 1 \\ 2\Omega \\ 0 \end{bmatrix} + d_2 \cos\Omega t \begin{bmatrix} -2 \\ 0 \\ 0 \\ \Omega \end{bmatrix} = d_2 \begin{bmatrix} -2\cos\Omega t \\ \sin\Omega t \\ 2\Omega\sin\Omega t \\ \Omega\cos\Omega t \end{bmatrix} \tag{4.44}$$

where d_1 and d_2 are arbitrary. We can now compose complete solutions of the homogeneous Hill Equations from the linear combination of the individual $\mathfrak{z}_i(t)$,

$$x(t) = a + b + \frac{3}{2}\Omega ct + 2d_1 \sin\Omega t - 2d_2 \cos\Omega t$$

$$y(t) = c + d_1 \cos\Omega t + d_2 \sin\Omega t$$

If initial conditions of (x_0, y_0) and (u_0, v_0) are specified for the position and velocity we have

$$x(0) = x_0 = a + b - 2d_2$$

$$y(0) = y_0 = c + d_1$$

$$u(0) = u_0 = \frac{3}{2}\Omega c + 2d_1\Omega$$

$$v(0) = v_0 = d_2\Omega$$

Which results in the following solution for a particle trajectory as a function of time,

$$x(t) = x_0 + \frac{2v_0}{\Omega} + (6\Omega y_0 - 3u_0)\, t + \left(\frac{4u_0}{\Omega} - 6y_0\right)\sin\Omega t - \frac{2v_0}{\Omega}\cos\Omega t \qquad (4.45)$$

$$y(t) = 4y_0 - \frac{2u_0}{\Omega} + \left(\frac{2u_0}{\Omega} - 3y_0\right)\cos\Omega t + \frac{v_0}{\Omega}\sin\Omega t \qquad (4.46)$$

where the explicit dependence upon the initial conditions is retained for clarity. Note that if $v_0 = 0$ and $u_0 = \frac{3}{2}\Omega y_0$, we obtain locally straight trajectories

$$x(t) = x_0 + u_0 t$$

$$y(t) = y_0$$

which correspond to circular orbits about Saturn.

4.2.3 Dimensionless Hill Equations

We define dimensionless time $\tau \equiv \Omega t$ and scale all lengths by the small particle diameter d ($y^* = y/d$, $x^* = x/d$) to obtain a dimensionless form of the Hill Equations,

$$\frac{d^2y^*}{d\tau^2} + 2\frac{dx^*}{d\tau} - 3y^* = 0 \qquad (4.47)$$

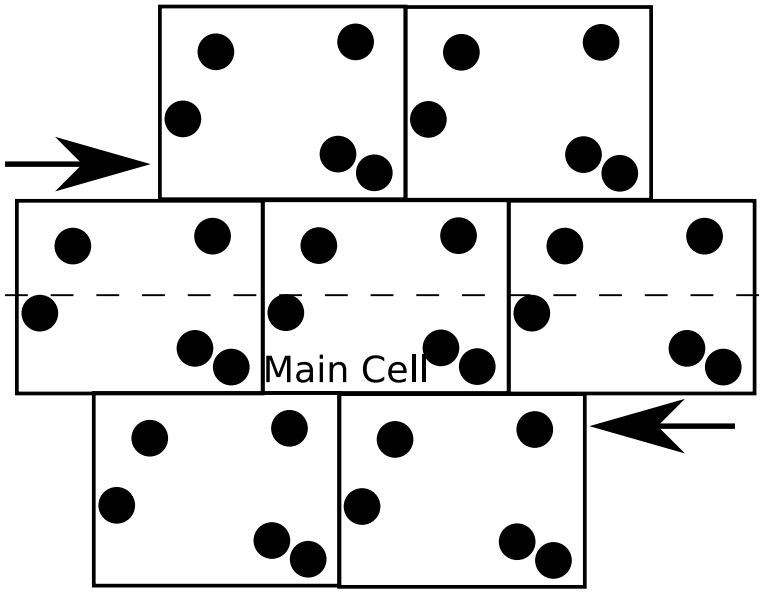

Figure 4.2: Sliding–block diagram of Lees–Edwards boundary conditions.

and

$$\frac{d^2x^*}{d\tau^2} - 2\frac{dy^*}{d\tau} = 0 \tag{4.48}$$

The dimensionless shear rate is $\gamma^* = du^*/dy^* = 3/2$, where u^* is the dimensionless speed in the azimuthal direction.

4.2.4 Boundary Conditions

The simulation domain ($0 \leq x \leq w^*,\ 0 \leq y \leq h^*$) makes use of Lees-Edwards boundary conditions [15, 20], visualized as a "sliding–block" diagram, shown in Figure 4.2. Image cells are placed adjacent to the main calculation domain, and particles pass between the cells. Image cells above and below the main cell are sheared with respect to the centerline (dashed in the figure).

In this construction, particles exiting the main cell in the azimuthal (x) directions are "replaced" by an image particle entering the opposing side. We note,

however, that it is not necessary to explicitly account for the image particles as the periodic condition can be accomplished with a x–coordinate change,

$$\text{if } \; x > w^* : \; x^+ = x - w^*$$
$$\text{if } \; x < 0 : \; x^+ = x + w^*$$

where the (+) sign indicates the new x–position. Radial (y) position and total velocity are preserved in the transformation.

Radial periodicity is similar, but due to shearing, position and velocity transformations are necessary to create the transitions in the sliding–block idealization,

$$\text{if } \; y > h^* : \; y^+ = y - h^*, \; u^+ = u - \frac{3}{2}h^*, \; x^+ = x - \frac{3}{2}h^*\tau$$
$$\text{if } \; y < 0 : \; y^+ = y + h^*, \; u^+ = u + \frac{3}{2}h^*, \; x^+ = x + \frac{3}{2}h^*\tau$$

where τ is the dimensionless simulation time. It can be shown that the Hill Equations are invariant under such transformations of position and velocity [38].

The use of Lees-Edwards boundary conditions permits the simulation to have a fixed number of particles and hence preserves the global packing fraction. Additionally, without such a periodic boundary or other appropriate physical constraints in the radial direction, particle pressure will cause the ring material to expand in any reasonable simulation time.

4.2.5 Particle Translations

Particle movement is governed by the dimensionless Hill Equations (4.47) and (4.48) and by collisional interactions. At every time step we integrate the Hill

Equations of motion with a second–order Runge–Kutta scheme and update the velocity and position of all particles. Following this, collisions are detected and post–collisional velocities are calculated according to Equations (4.3) and (4.4).

4.2.6 Simulation Parameters

Because of the scaling, control of the simulation without moonlet gravity is limited to the specification of scaled domain size (w^*, h^*), moonlet size D (in small–particle diameters), restitution coefficient e, and global area fraction, ν. Particles are initially homogeneously distributed with the specified area fraction and are given appropriate azimuthal speeds for their radial distance from the moonlet, $u^* = \frac{3}{2}(y^* - h^*/2)$. After this, particle motions are governed by the Hill Equations and collisional interactions with the moonlet and each other. Simulations are performed for increasing durations to ensure that a steady state has been reached.

The azimuthal extent of the simulation is taken to be great enough that apparent positional correlations/structure are destroyed by the agitation of the shear flow before particles are periodically circulated. The radial dimension of the simulations is similarly chosen large enough that the Lees-Edwards boundary conditions do not affect behavior in the region of interest near the moonlet.

4.3 Analysis

In this section we use kinetic theory to derive an expression for the temperature in a steady–state sheared granular flow. With this expression and our equilibrium sound speed from Chapter 2 we are able to obtain an estimate for the Mach number and hence an estimate for the sonic character of flow in Saturn's rings. We show

that flow particle speed relative to the moonlet exceeds the sound speed within several particle diameters of the moonlet's radial location and as a result shocks are likely to develop.

4.3.1 Shear Flow Temperature

Here we derive an expression for the velocity dispersion of identical, inelastic, circular disks of diameter d in steady shear flow. We show that Saturn's rings have relatively low mean agitation with respect to flow speed and thus disturbance information is slow to propagate through the medium. We first examine the energy balance equation [18],

$$\rho\dot{T} + P_{\alpha\beta}D_{\alpha\beta} + \frac{\partial q_\alpha}{\partial x_\alpha} = \Gamma \tag{4.49}$$

where ρ is density, T the granular temperature, $\mathbf{P}$ the pressure tensor, $\mathbf{D}$ the rate of strain tensor, $\nabla \cdot \mathbf{q}$ the divergence of the heat flux, and Γ the collisional energy dissipation. Again, subscripts denote components with respect to orthogonal basis vectors in the plane and we employ the convention of summing over repeated indices. Given an ensemble mean velocity $\mathbf{u} \equiv \langle \mathbf{c} \rangle$, the fluctuating velocity component is $\mathbf{C} = \mathbf{c} - \mathbf{u}$, and the granular temperature is $T \equiv \langle \mathbf{C} \cdot \mathbf{C} \rangle$ in two–dimensions. The mass density is the product of constituent material density ρ_m and the area fraction ν. Given a number density n, the area fraction is defined as $\nu = n\pi d^2/4$.

In steady state, the adiabatic energy equation simplifies to,

$$P_{\alpha\beta}D_{\alpha\beta} = \Gamma \tag{4.50}$$

which states the balance of stress–work and collisional dissipation. For $D_{\alpha\beta} \equiv \frac{1}{2}(u_{\alpha,\beta} + u_{\beta,\alpha})$, the only non-trivial component in fully-developed shear flow is

$D_{12} = D_{21} = \gamma/2$, where $\gamma \equiv \partial u_1/\partial x_2$ is the shear rate. Due to symmetry of the pressure tensor we may write,

$$P_{12}\gamma = \Gamma \tag{4.51}$$

The collisional dissipation term for frictionless disks of restitution coefficient e is [18]

$$\Gamma = -\frac{4\alpha T(1-e)}{d^2} \tag{4.52}$$

where the bulk viscosity term is $\alpha \equiv 8m\nu^2 g_0 \breve{r} T^{\frac{1}{2}}/d\pi^{\frac{3}{2}}$, m is the mass of a disk, $\breve{r} \equiv (1+e)/2$, and $g_0(\nu)$ is the radial distribution function for disks in contact [36],

$$g_0(\nu) = \frac{16 - 7\nu}{16(1-\nu)^2} \tag{4.53}$$

Additionally, we define $G \equiv \nu g_0$. The pressure tensor is

$$P_{\alpha\beta} = (p - \alpha D_{\gamma\gamma})\delta_{\alpha\beta} - 2\mu\hat{D}_{\alpha\beta} \tag{4.54}$$

where the hat denotes the deviatoric part of the tensor. The isotropic pressure is,

$$p = \rho(1 + 2G\breve{r})T \tag{4.55}$$

and the viscosity is [18],

$$\mu = \mu'(1 + G\breve{r}) + \frac{\alpha}{2} \tag{4.56}$$

where,

$$\mu' = \frac{m\nu\overline{T}^{1/2}}{Gd(5 - 3\breve{r})\sqrt{\pi}}[1 + G\breve{r}(3r - 2)] \tag{4.57}$$

The shear stress is then

$$P_{12} = \frac{-m\nu T^{1/2}\gamma}{Gd\sqrt{\pi}(5 - 3\breve{r})}\left[1 - G\breve{r} + (3G - 2G^2)\breve{r}^2 + 3G^2\breve{r}^3\right] - \frac{\alpha\gamma}{2} \tag{4.58}$$

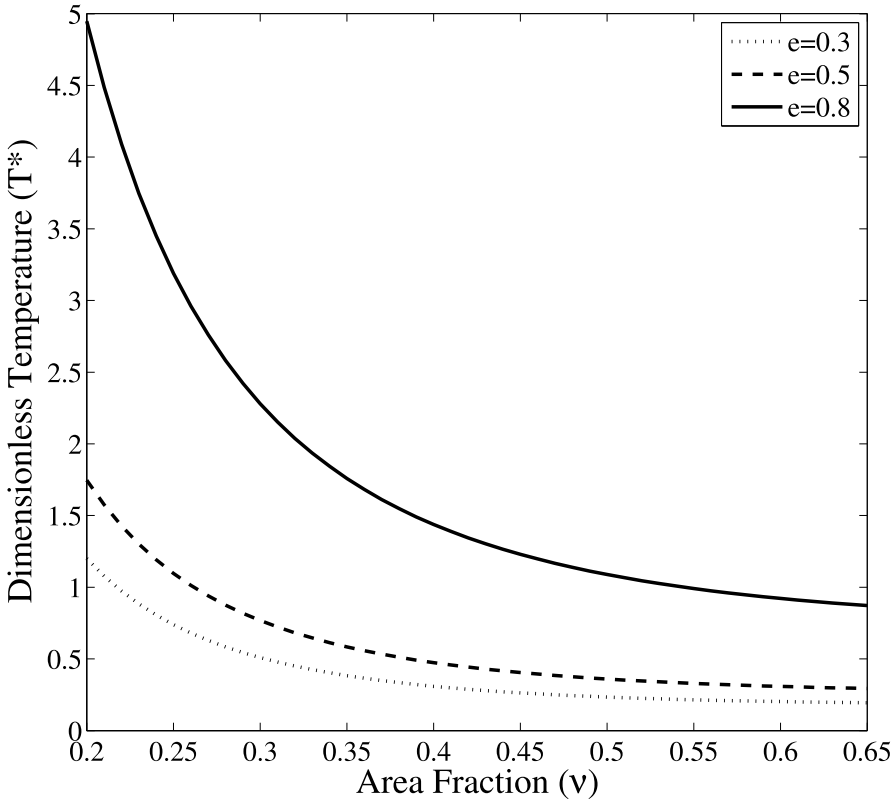

Figure 4.3: Non–dimensional temperature variation with area fraction. Equation (4.59) is plotted for restitution coefficients of $e = 0.3, 0.5, 0.8$.

Equations (4.52) and (4.58) used in the energy equation yield an expression for $T^* \equiv T/d^2\gamma^2$,

$$T^* = \frac{1}{16(1-\breve{r})}\left[\frac{\pi[1-G\breve{r}+(3G-2G^2)\breve{r}^2+3G^2\breve{r}^3]}{4G^2\breve{r}(5-3\breve{r})}+1\right] \tag{4.59}$$

This is plotted for several restitution coefficients in Figure 4.3 below.

For nearly elastic particles $e \approx 1$, so $\breve{r} \approx 1$ and

$$T^* = \frac{1}{8(1-e)}\left[1+\frac{\pi}{8}\left(1+\frac{1}{G}\right)^2\right] \tag{4.60}$$

It is noted that Equation (4.59) is valid for intermediate area fractions where $G(\nu)$ is near 1. Jenkins and Richman [19] derive expressions in the limit of dilute and dense shearing, but observed optical depths of Saturn's A–ring indicate that intermediate area fractions are of interest.

4.3.2 Mach Number

The mach number M is defined as the ratio of flow speed to sound speed, such that $M = 1$ defines the transition from subsonic ($M < 1$) to supersonic ($M > 1$). In Keplerian flow with shear rate γ, we may write the azimuthal speed as a function of the radial distance from the moonlet's azimuthal axis as,

$$u = \gamma y = \gamma y^* d \tag{4.61}$$

where we consider the dimensional speed in terms of particle diameter and the dimensionless radial coordinate. We divide by the dimensional temperature from equation (4.59), cancelling any dependence upon d and γ in the ratio,

$$\frac{u^2}{T} = \frac{16y^{*2}(1-\breve{r})}{\left[\frac{\pi[1-G\breve{r}+(3G-2G^2)\breve{r}^2+3G^2\breve{r}^3]}{4G^2\breve{r}(5-3\breve{r})}+1\right]} \tag{4.62}$$

Using (4.62) divided by the expression for the sound speed (Equation (2.27)), we write the square of the mach number as,

$$M^2 = \frac{4096G^2y^{*2}(5\breve{r}-8\breve{r}^2+3\breve{r}^3)(1-\nu)^4}{\varsigma(\nu)\left[\pi+(20G^2-G\pi)\breve{r}+(3\pi G-2\pi G^2-12G^2)\breve{r}^2+3\pi G^2\breve{r}^3\right]} \tag{4.63}$$

where,

$$\varsigma(\nu) = 9\nu^4 - 32\nu^3 - 24\nu^2 + 128 \tag{4.64}$$

and we see that the Mach number is a function of restitution coefficient (via r), area fraction, and the radial displacement from the moonlet's semi–major axis. Dividing by the dimensionless radial coordinate, we plot M/y^* in Figure 4.4. From the plot, one can see that the shear flow becomes supersonic ($M > 1$) within several particle diameters of the moonlet's semi–major axis. Note that for a given restitution coefficient, the Mach Number is lower at the dilute and dense extremes of area fraction. This is due to the competing nature of the temperature and the sound speed as they appear in the ratio; dilute states have lower relative sound speeds, but the temperature is higher due to lower collision frequency. Conversely, denser states have greater sound speeds, but are lower in temperature. From this analysis it is reasonable to expect that incident flow with respect to the moonlet has significantly exceeded the sonic speed and we are in consideration of bow shock development about a blunt body.

4.4 Results

Based on inferred packing fraction and the dissipative nature of the ring material, shear flow in Saturn's rings is predominantly supersonic. Within several particle diameters of the moonlet's radius we experience average azimuthal (orbital) speeds sufficient to exceed the sound speed. The creation of shocks is indicative of supersonic flow, as we saw in our examination of shocks created by wedge bodies.

In our simulations we look to obtain information regarding the effects of contact energetics (via the restitution coefficient), the global density of particles, and the relative size of the moonlet with respect to characteristic ring particles. In the

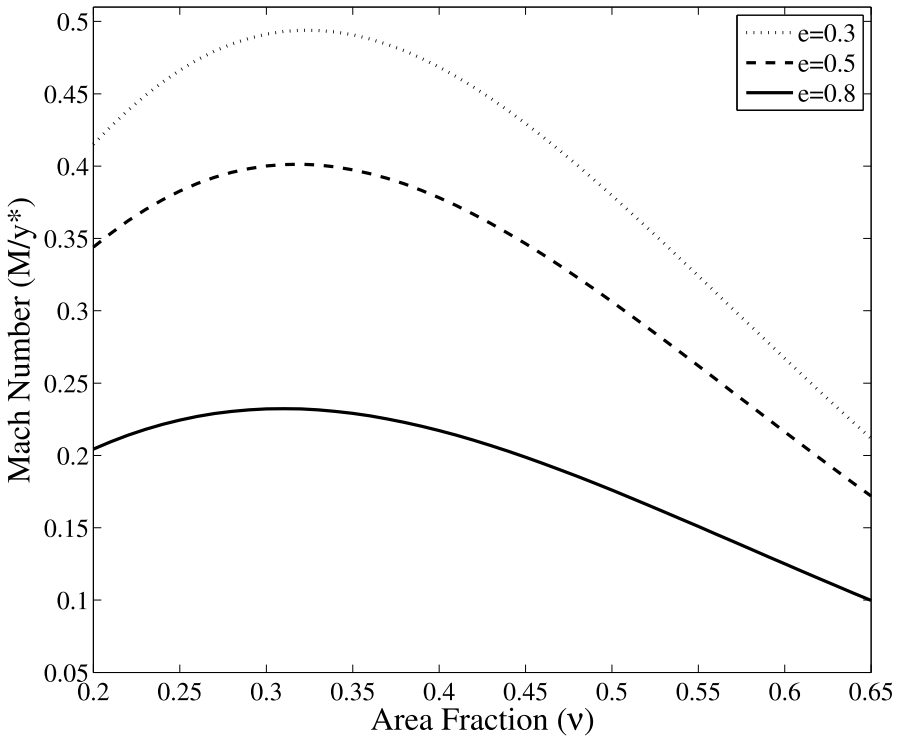

Figure 4.4: Mach Number (divided by dimensionless radial distance) variation with area fraction. Equation (4.63) is plotted for restitution coefficients of $e = 0.3, 0.5, 0.8$.

following images, only a portion of the entire simulation is pictured– the full simulation extends significantly further in both the radial and azimuthal directions. Simulation domains were chosen to be 900pd in the azimuthal direction and 150pd radially. Shock features did not approach the radial (Lees-Edwards) boundary and secondary structures did not extend across the azimuthal periodic boundary.

In Figure 4.5 we vary the restitution coefficient and note the change in both the detached shock feature and the vacancy behind the moonlet. As shown in Figure 4.4 the mach number (and hence the strength of the shock) increases with decreasing restitution coefficient– we see the density in the shocked region is greater for the more dissipative collisions. It is also apparent that the more elastic collisions have a shorter vacant region behind downstream of the moonlet. This is consistent with more elastic particles having a greater temperature. At the same global density the higher granular temperature results in increased collision frequency and faster diffision of particles. This suggests the change in the length of the empty region is dependent on factors other than the orbital dynamics (the Hill Equations). Since the moonlet size remains constant between simulations, the perturbations in the particle orbits and the resulting eccentric orbits should be similar.

In Figure 4.6 we vary the size of the moonlet relative to the small particles. We note that the resulting shock formations decrease in size and strength (density) as the ratio decreases. For a size ratio of 10 there is indeed a very minimal shock and the global area fraction of the simulation is spatially uniform. From the larger size ratios we also note that shock features do not begin at the semi–major axis of the moonlet; one can observe that the bottom of the shock begins several particle diameters displaced from this line. Both of these findings suggest a threshold speed for shock creation, which we identify as the sound speed. The minimal shock for the

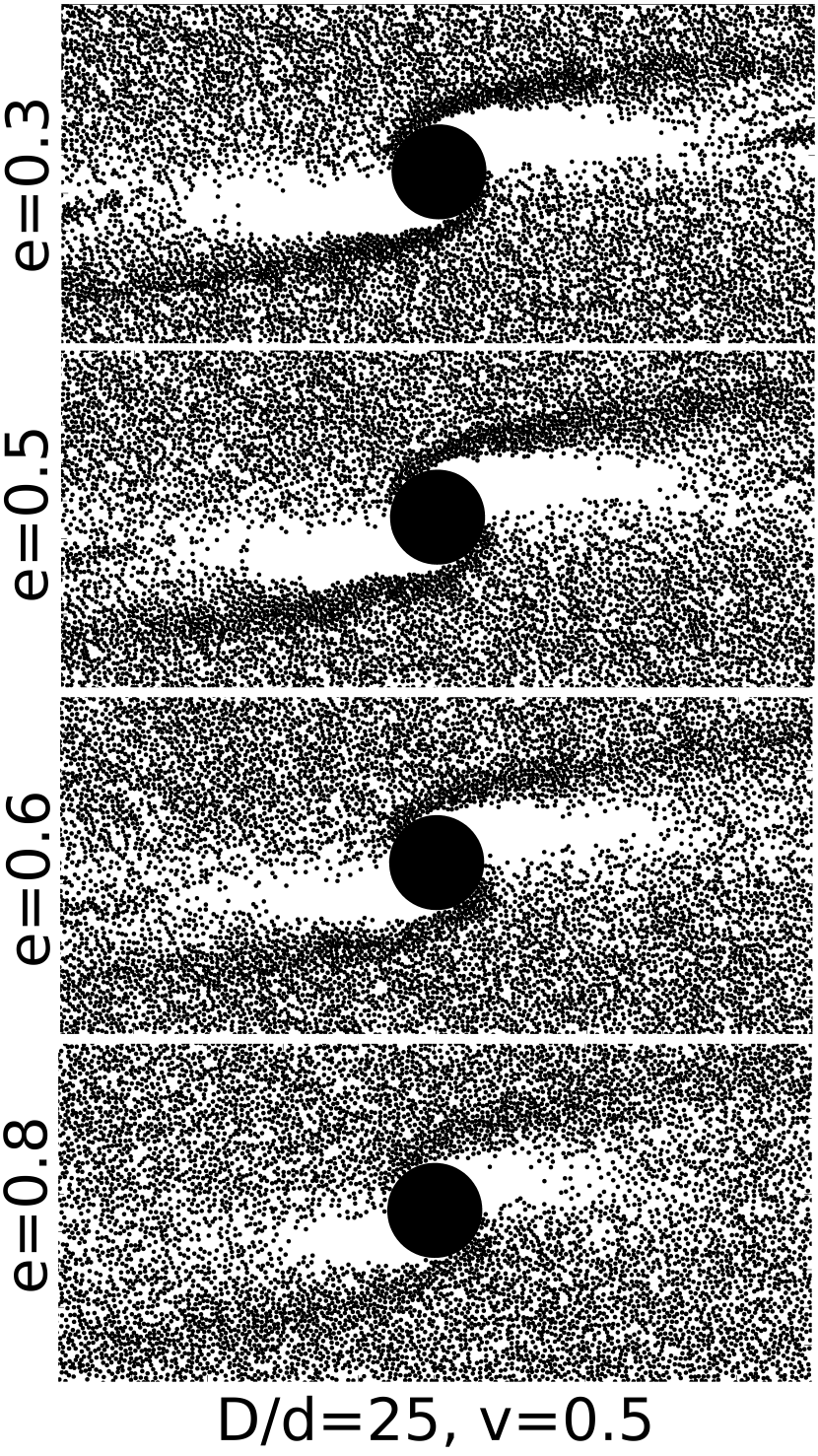

Figure 4.5: Propeller formation for varied collisional restitution coefficients

instance of $D/d = 10$ indicates that incident shear flow is approximately sonic at a maximum of 5 particle diameters from the semi-major axis. Given the restitution coefficient of $e = 0.3$ and global area fraction of $\nu = 0.5$, Figure 4.4 suggests that one will achieve $M = 1$ at approximately 2.5-3 particle diameters, which is in good agreement with our simulations. The other striking feature of these images is the size of the vacant regions. As referenced, some studies suggest the extent of these features is dependent on the Hill radius (for the case where a moonlet gravitational potential is present) while others do not see this scaling. Without a gravitational force from the moonlet we are unable to define a Hill radius, but it is clear that merely the size of the body (without regard for mass) has a great effect on the resulting structure of the propeller. We examine gravitational effects of the moonlet below.

In Figure 4.7 we plot the steady–state simulation images for three values of global area fraction. We see shock formation in all three, as expected, but the thickness of the shock varies significantly. Suggested by Figure 4.4, we expect $M > 1$ within several particle diameters of the moonlet's axis for all densities shown. Even at the highest area fraction, we may still characterize the flow as supersonic. We do note, however, that the length of the vacancies decreases with increasing area fraction. If the propeller is identified by the transmission (or reflection) of light relative to the surrounding ring material, we see that the denser situations will exhibit shorter empty regions. Although the increased density in turn decreases the velocity fluctuations, collision frequency is higher and hence particles will diffuse into the empty region within a shorter distance. As in the case where we varied the restitution coefficient, this emphasizes that the spatial extent of these features is not solely determined by the orbital dynamics, but by collisional effects.

In Figure 4.8 for the top half of the simulation we plot the velocity field of

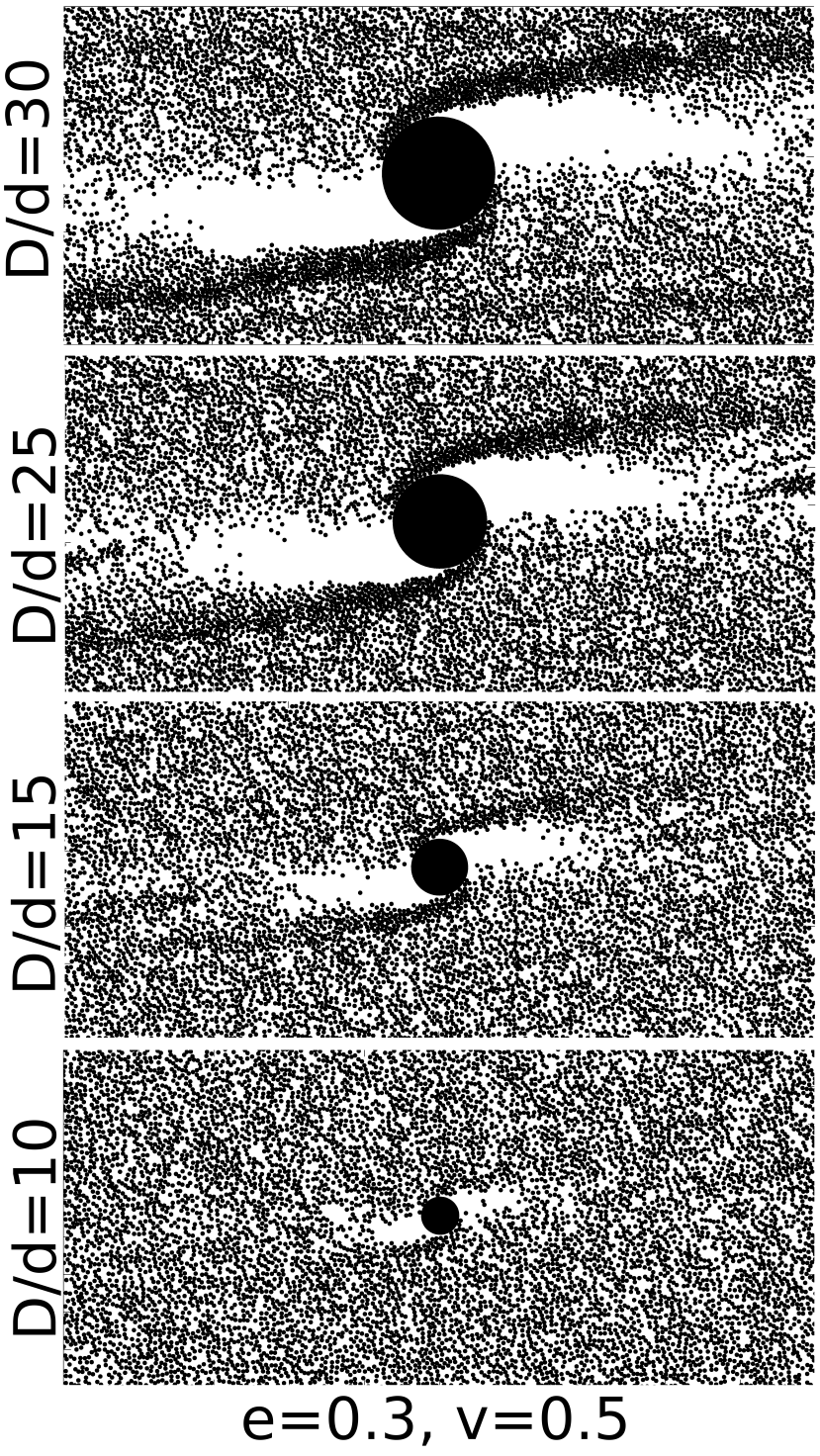

Figure 4.6: Propeller formation for varied moonlet size

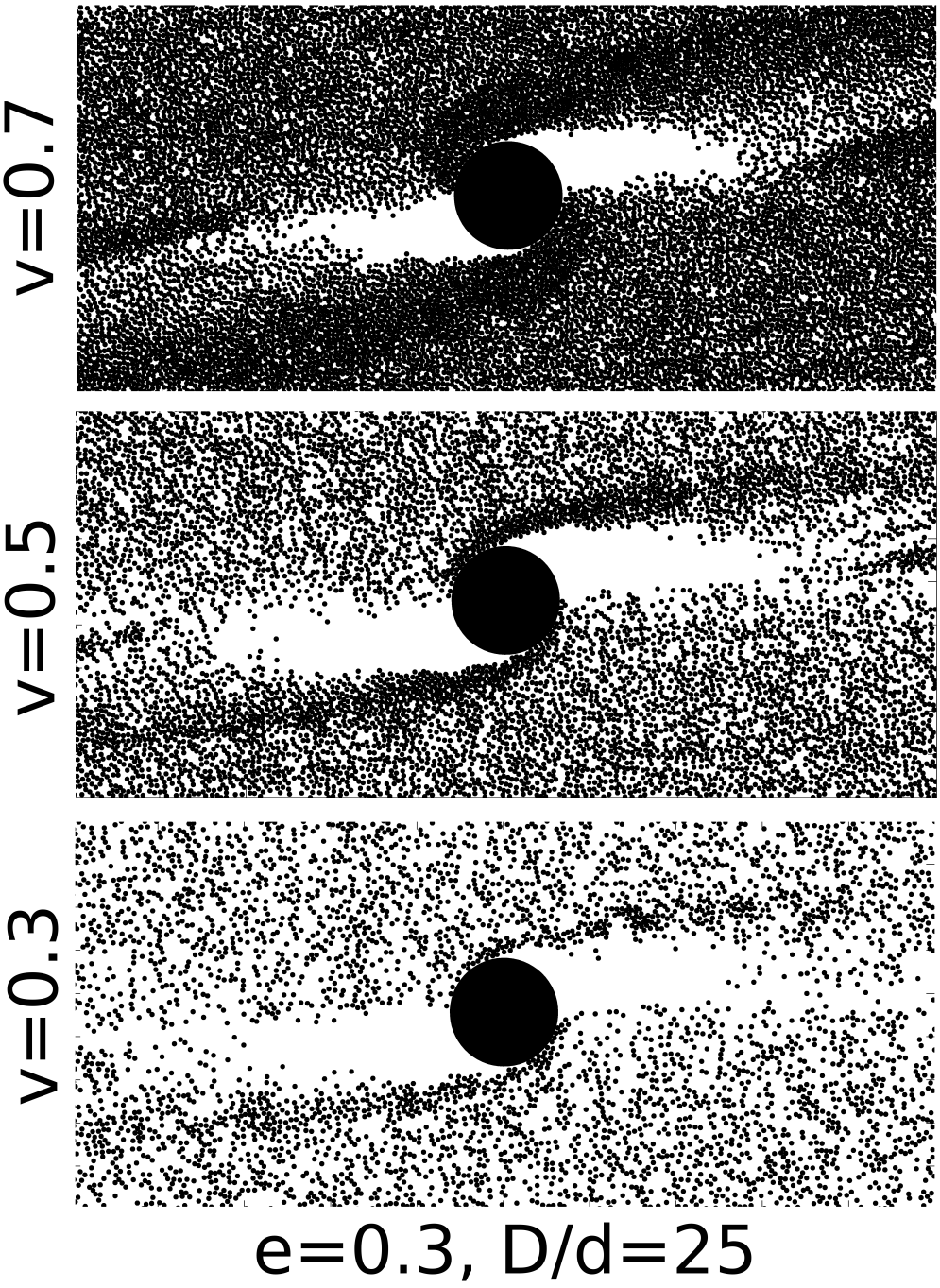

Figure 4.7: Propeller formation for varied global density

particles local to the moonlet. This confirms that the shock is not a static aggregate of particles, but rather the flow is turned by the body and experiences changes in its properties. The shock's spatial characteristics are steady in time but there is an appropriate flux of mass entering and exiting the shocked region. This is in accord with our observations of granular flow over an obstructing wedge.

We may compare these findings with that of [21] where moonlet gravity is included in their more realistic simulation. In this way we may be able to obtain some estimate of the relative importance of collisional and gravitational effects. We note that moonlet gravity has the effect of accreting flow particles on the bodies' perimeter and also altering the shape and orientation of the high density regions. We see that with the inclusion of gravity, the high density propeller feature is oriented in a more radial direction. Lewis and Stewart's images of particle clusters about the moonlet show significant accretion on the "top" and "bottom" of the moonlet, depending upon size ratios, particle polydispersity, and self–gravitation. In contrast, the purely collisional simulation naturally does not develop clustering and the particles comprising the shock feature do not remain "stuck" to the moonlet. We do not believe that clustering precludes shock development, however. It is possible that in addition to the static accretion, there may be a shock developed in addition to the clustering. This would be of interest for further study.

For the gravitational simulations we also note that the apparent vacant regions are spatially larger in both the radial and azimuthal directions. Images show the persistence of vacancies for distances significantly further than those displayed in the collisional simulations. Collisional propellers extinguish within several moonlet diameters whereas those including gravitation remain apparent for the entire azimuthal extent shown in Lewis and Stewart's images (approximately 60 moonlet diameters shown to either side of the moonlet). With the ability to resolve the size

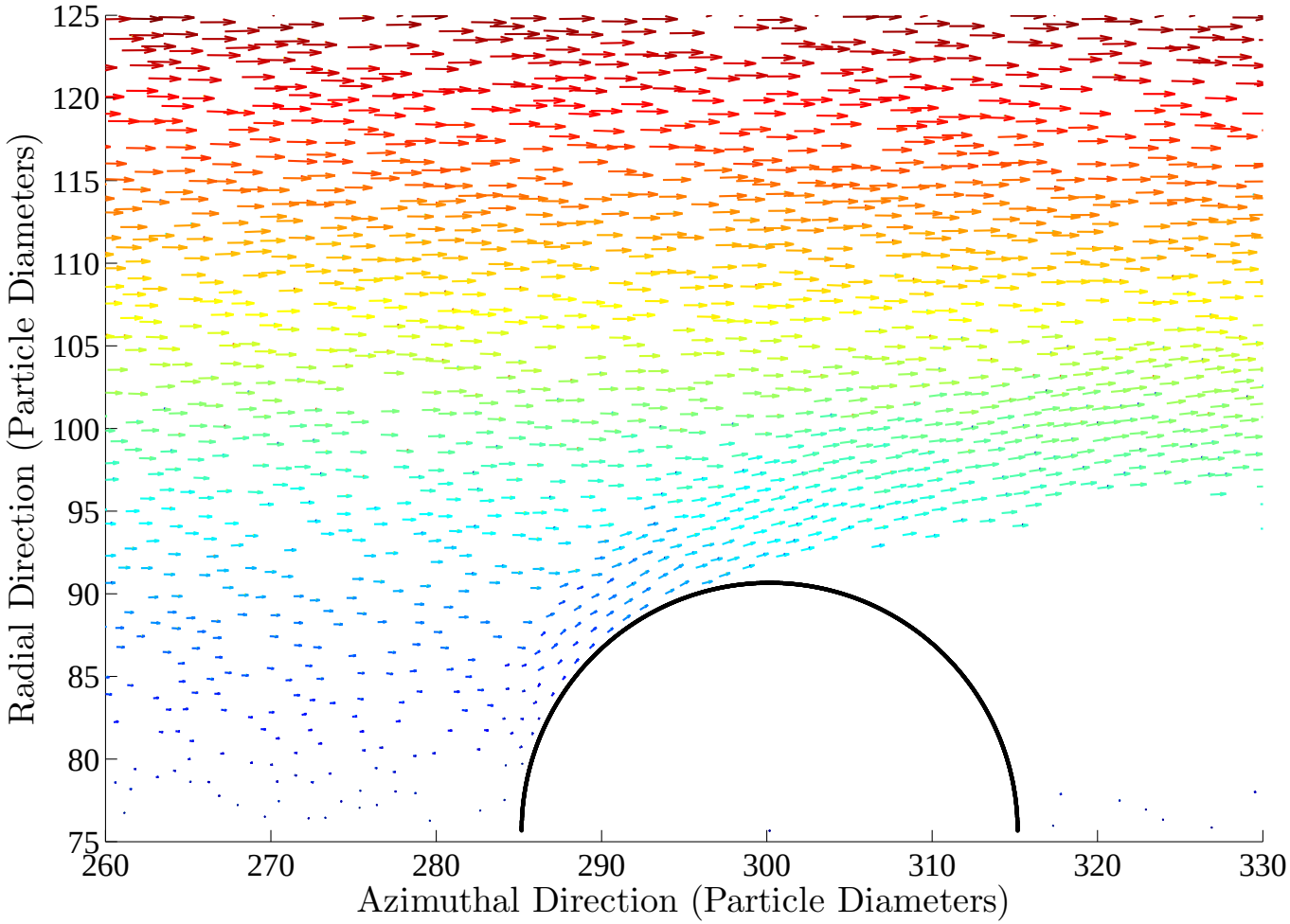

Figure 4.8: Velocity field about the top half of a simulation. Increasing velocity is denoted with "warmer" colors.

of the moonlet and propellers from satellite images, it might be possible to determine the relative importance of the two effects. However, it is noted that while the two–dimensional simulations show clear vacancies, the light regions appearing in Cassini images are not necessarily empty regions. In fact, [34] indicates that the observed features in field images may in fact be due to local increases in the optical depth (a measure of light transmission/reflection, related to density) but not necessarily mass density. For the moment we note that numerical simulations create visible gaps with bordering density increases (aggregation, shocks), but propeller observations are still subject to further interpretation and is discussed in the cited work by Tiscareno.

We also note the appearance of secondary high density features bordering the vacant regions in both simulations with and without gravity. At significant distances from the moonlet where gravitational effects due to the presence of the moonlet are smaller in comparison to that of Saturn, the creation of these structures may be determined solely by the dynamics which drive particle collisions. In Figure 4.9 we plot particle positions with sample streamlines overlaid for the lower half of a simulation. These streamlines display the epicyclic orbits consistent with objects perturbed (in this case by the moonlet and interparticle collisions) from their appropriate radial position. We see that the streamlines converge in the same region where we observe the secondary high density structure. The higher density of streamlines suggests an increased collision probability. Inelastic collisions damp the energy and create the resulting density structure. As shown in the simulations, we expect the size of the moonlet to affect the perturbation of the orbits and hence the location of convergence regions. We note that the aspect ratio of the image is altered to allow viewing of the particles and the streamlines. At the proper aspect ratio the streamlines obscure the viewing of particle positions. The correlation of

streamlines with these features suggests the Hill equations dominate the formation of the secondary structures.

It warrants further study to determine what effect the moonlet's mass has on the relative importance of gravitational and collisional effects. Terms in the inhomogeneous Hill Equations related to the gravitational force of the moonlet contain the ratio of Saturn's mass to that of the moonlet so that it is related to the cube of the moonlet size and the moonlet constituent density. With increasing size, we expect the contribution of the gravitational term to be increasingly significant. It may be possible that smaller moonlets exhibit behavior more consistent with that of a granular shock.

4.5 Conclusions

In this chapter we examined propeller formation in Saturn's rings without moonlet gravity in the context of granular shock. The effects of collisional energetics, global density, and moonlet size were qualitatively examined with the use of discrete particle numerical simulations. By the use of our prior derived equilibrium sound speed and the determination of the granular temperature in the steady shear flow, we were able to obtain an estimate for the nature of flow in Saturn's rings. The analysis suggests that such flow is inherently supersonic and granular shock may be partially responsible for propeller formation. By our study in Chapter 2 we are led to believe that our sound speed estimate is approximately correct and we are indeed witnessing, in part, a granular shock. The shock may be formed on top of gravitationally accreted particles. Our findings are similar to that of the more complete simulations, but with some distinct differences, namely the azimuthal extent of low density regions and the orientation and thickness of higher density formations. However, without additional observation at sufficient image resolution,

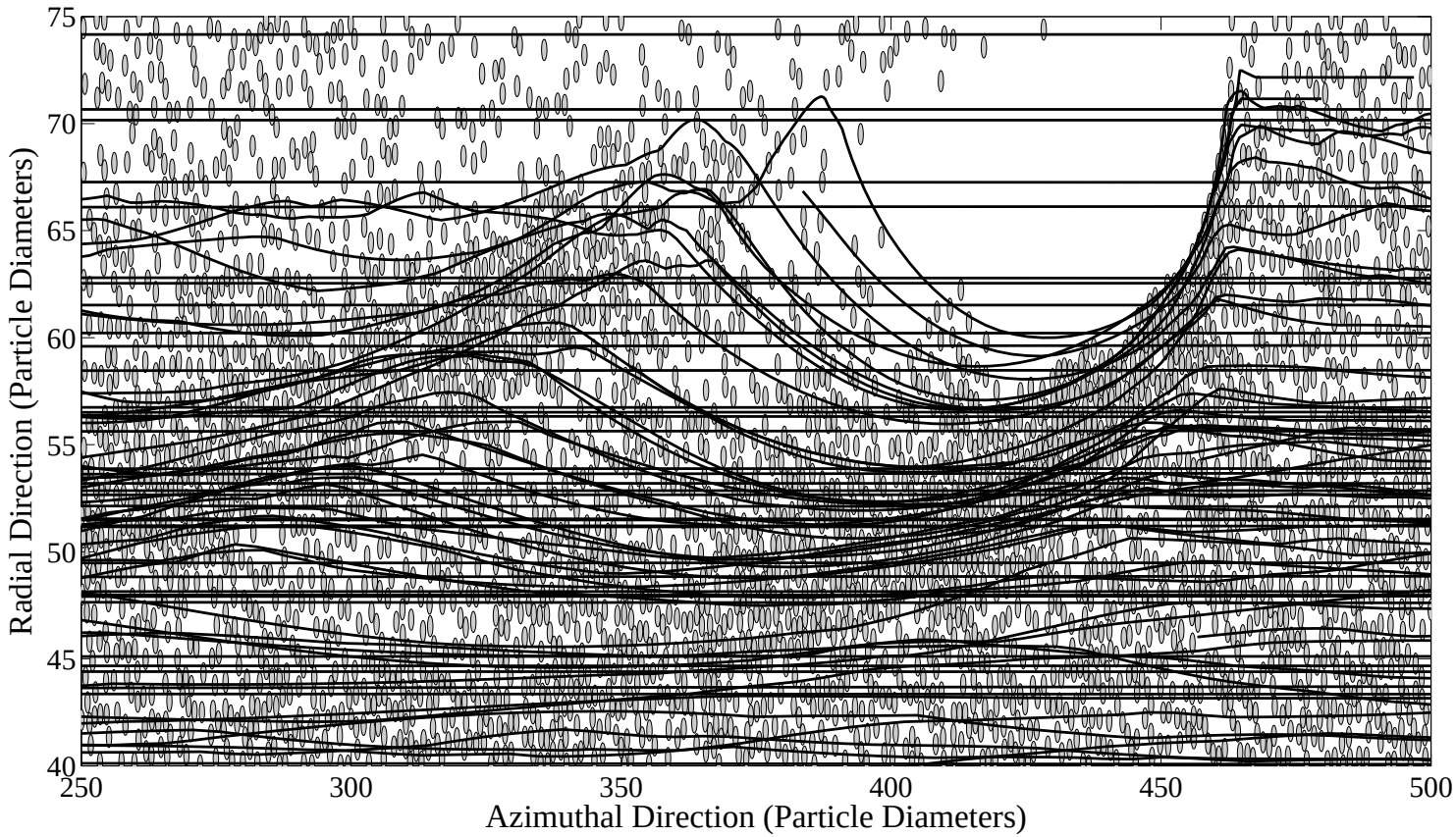

Figure 4.9: Overlay of particle positions and streamlines of sample particles. Aspect ratio is altered to allow for easier differentiation of particles and the streamlines.

the details of the propeller gaps and density enhancements are not accessible. As we were interested in solely collisional effects, it remains to definitively quantify the relative importance of the collisional effects against the gravitational forces that are present in nature. It is suggested that the size of moonlet may determine the nature (and hence the morphology) of the resulting structure– small moonlets may be collisionally dominated while larger bodies could have more gravitationally relevant features.

CHAPTER 5

BALANCE RELATIONS APPLIED MOONLET SHOCKS

Here we use the depth–averaged differential equations derived in Chapter 3 to approximate the shape and properties of the shock front about an embedded moonlet in Saturn's rings. Starting from the general differential relations with our usual assumptions regarding the body pressure, area fraction, and body–normal flow speed we also look to introduce the previously neglected body force terms in the analysis. We also introduce incoming shear flow, consistent with Keperlian flow in the reference frame of the moonlet.

5.1 Governing Equations

We model the depth–averaged pressure as the mean of the post–shock and body pressure as in Section 3.2.3. Retaining the body force terms $\mathbb{J}_1$ and $\mathbb{J}_2$, our three differential equations in δ, p, u are,

Mass:

$$\nu \frac{d}{d\xi}(u\delta) - A\delta' = B \tag{5.1}$$

ξ–Momentum:

$$\rho_m \nu \frac{d}{d\xi}\left(u^2\delta\right) + \frac{d}{d\xi}(p\delta) - C\delta' - \mathbb{J}_1 = D \tag{5.2}$$

η–Momentum:

$$\begin{aligned} D\delta'^3 + \left[(2+r)p_1 - 2p + \rho_m \nu_1 V_1^2 - rC - \mathbb{J}_2\right]\delta'^2 + \\ +(3D - 2rD)\delta' + 2E - rE + rp_1 - 2p - \mathbb{J}_2 = 0 \end{aligned} \tag{5.3}$$

where

$$\mathbb{J}_1 = \int_0^\delta \rho b_\xi \, d\eta \tag{5.4}$$

$$\mathbb{J}_2 = \int_0^\delta \rho b_\eta \, d\eta \tag{5.5}$$

and the constants A–E are defined in Chapter 3.

We now use the homogeneous Hill Equations to determine the body force $\mathbf{b}$ in the ξ and η directions. We write these in dimensional form,

$$\frac{d^2y}{dt^2} + 2\Omega\frac{dx}{dt} - 3\Omega^2 y = 0 \tag{5.6}$$

$$\frac{d^2x}{dt^2} - 2\Omega\frac{dy}{dt} = 0 \tag{5.7}$$

The body forces (per unit mass) are,

$$b_y = -2\Omega\frac{dx}{dt} + 3\Omega^2 y \tag{5.8}$$

$$b_x = 2\Omega\frac{dy}{dt} \tag{5.9}$$

Given that the local shock–oriented frame is rotated by angle θ with respect to the azimuthal/radial (x, y) axes , we can relate dx/dt and dy/dt to the body–aligned speed u and body–normal speed v,

$$\frac{dx}{dt} = u\cos\theta - v\sin\theta$$

$$\frac{dy}{dt} = u\sin\theta + v\cos\theta$$

then we project the body force into our (ξ, η) system to obtain,

$$b_\xi = 3\Omega^2 y\sin\theta + 2\Omega v$$

$$b_\eta = 3\Omega^2 y\cos\theta - 2\Omega u$$

With knowledge of the body shape (a quarter circle in this instance) we are able to express the coordinate y in terms of ξ, η, and the moonlet radius R_m,

$$y = (R_m + \eta)\sin\left(\xi/R_m\right) \tag{5.10}$$

Note that for the circular geometry, $\sin(\xi/R_m) = \cos\theta$ and we may write,

$$y = (R_m + \eta)\cos\theta(\xi) \tag{5.11}$$

where we explicitly denote that θ changes with the coordinate ξ. Thus, For $\mathbb{J}_1$ we have,

$$\mathbb{J}_1 = \int_0^\delta \rho\left[3\Omega^2 y\sin\theta + 2\Omega v\right]\ d\eta \tag{5.12}$$

with our assumption of constant ν we may remove the density from the integration. We also use 5.11 to substitute for y,

$$\mathbb{J}_1 = \rho_m\nu\int_0^\delta (3\Omega^2(R_m+\eta)\cos\theta\sin\theta + 2\Omega v)\ d\eta \tag{5.13}$$

Employing our assumption $\overline{v} = 0$ we can see that the second term will vanish. We are then left with,

$$\mathbb{J}_1 = 3\rho_m\nu\Omega^2\sin\theta\cos\theta\left(R_m\delta + \frac{\delta^2}{2}\right) \tag{5.14}$$

In a similar manner we determine $\mathbb{J}_2$,

$$\mathbb{J}_2 = 3\rho_m\nu\Omega^2\cos^2\theta\left(R_m\delta + \frac{\delta^2}{2}\right) - 2\rho_m\nu\Omega u\delta \tag{5.15}$$

We now look to phrase the differential equations in a non–dimensional form using appropriate scalings. In our discrete element simulations the natural scales for length and time were particle size and the inverse shear rate (Ω), respectively.

Lacking a small particle dimension in our continuum approach here, an appropriate length scaling is the moonlet radius R_m. With the inclusion of the body force terms featuring Ω, we again choose the inverse shear rate to scale times. We define dimensionless parameters as follows:

$$\xi^* = \frac{\xi}{R_m}, \qquad \delta^* = \frac{\delta}{R_m}, \qquad u^* = \frac{u}{R_m\Omega}, \qquad p^* = \frac{p}{\rho_m R_m^2 \Omega^2}$$

We also note that due to the Keplerian shear flow with respect to the moonlet, incoming horizontal speed V_1 is a function of distance from the moonlet's radius. Thus,

$$V_1 = \frac{3}{2}\Omega y = \frac{3}{2}\Omega(R_m + \delta)\cos\theta \tag{5.16}$$

in non–dimensional form,

$$V_1^* = \frac{3}{2}(1 + \delta^*)\cos\theta \tag{5.17}$$

We now phrase our governing differential equations in non-dimensional form:

Mass:

$$\nu\frac{d}{d\xi^*}(u^*\delta^*) - \frac{3}{2}\nu_1\cos\theta(1+\delta^*)(\delta'\cos\theta + \sin\theta) = 0 \tag{5.18}$$

ξ–momentum:

$$\nu\frac{d}{d\xi^*}\left(u^{*2}\delta^*\right) + \frac{d}{d\xi^*}(p^*\delta^*) - \frac{9}{4}\nu_1(1+\delta^*)^2\cos^3\theta(\delta'\cos\theta + \sin\theta) - \\ -p_1^*\delta' - \frac{3}{2}\delta^*\nu\sin\theta\cos\theta(2+\delta^*) = 0 \tag{5.19}$$

η–Momentum:

$$\left[\frac{9}{4}\nu_1(1+\delta^*)^2\cos^3\theta\sin\theta\right]\delta'^3 + \\ + \left[2(p_1^* - p^*) + \frac{9}{4}\nu_1(1+\delta^*)^2\cos^2\theta(1 - r\cos^2\theta) - \right. \\ \left. - \frac{3}{2}\delta^*\nu\cos^2\theta(2+\delta^*) + 2\nu u^*\delta^*\right]\delta'^2 + \\ + \frac{9}{4}\nu_1(1+\delta^*)^2\cos^3\theta\sin\theta(3-2r)\delta' + 2(p_1^* - p^*) + \\ + \frac{9}{4}\nu_1(1+\delta^*)^2(2-r)\cos^2\theta\sin^2\theta - \frac{3}{2}\delta^*\nu\cos^2\theta(2+\delta^*) + 2\nu u^*\delta^* = 0 \tag{5.20}$$

Although not particularly obvious in the form of these differential equations, the first order form of these equations contain terms of the form $1/\sin\theta$ and $1/\cos\theta$ which result in numerical issues as $\theta \to 0$ and $\theta \to \pi/2$, respectively. Fortunately we have shown that shocks do not begin at the radial location of the moonlet's center; the shear flow transitions to supersonic at a finite distance from $y = 0$, on the order of several particle diameters. Additionally, simulation images indicates that the flow does not remain attached to the body as θ approaches $\pi/2$. This allows us to neglect these regions in the integration of the differential equations.

5.2 Boundary Conditions

As with our application to the wedge geometry, we require boundary conditions on the variables p,u, and δ. For the flow speed, we enforce the symmetry condition of zero mass flux– on average, the incident shear flow is normal to the moonlet at $y = 0$. Thus u_o is set to be approximately zero We expect the shock to be approximately normal, indicating that the flow turning angle θ is small and hence flow tangential to the body is negligible.

For the boundary condition on pressure, we once again approximate the shock as normal to the incoming flow. Likewise we approximate the body as being vertical. Although the shock does not begin exactly at the center of the moonlet– the offset is on the order of several particle diameters– both the bow shock and the body are close to perpendicular in this region. These pressures balance accordingly. From our model of the depth–averaged pressure as $p = (p_2 + p_b)/2$ this sets our boundary condition to be $p_o = p_2$.

Similar to the case of the bow shock over the wedge, we are left with the initial shock offset as a fitting parameter.

5.3 Results

As input to the differential equation solver we specify the global area fraction (ν_1), the moonlet radius R_m, and the restitution coefficient for collisions. The upstream flow speed V_1^* is set according to (5.17) and non–dimensional temperature by (4.59). Boundary conditions are set according to the approximations described above. The offset of the shock from the moonlet's radius is also set– this is typically several particle diameters depending upon where the shear flow becomes supersonic (Figure 4.4). The initial offset δ_o is also given as an input.

In a similar fashion to the solutions presented in Chapter 3, we phrase the governing differential equations in first–order form. We use MATLAB's root–finding algorithm `fzero()` to find roots of the cubic (5.20) and determine $d\delta/d\xi$. The range of integration extends from where the shock begins (given as input) and terminates at a position prior to the top of the moonlet ($\theta = \pi/2$) where we might encounter numerical issues related to $1/\cos\theta$ terms. This difficulty could be addressed, but since simulations show the shock detaching prior to the top of the moonlet, it is not necessary to integrate to that limit.

In Figure 5.1 we plot the shock solutions for several boundary conditions on the shock thickness δ_o. The values $\delta_o = 0.4,\ 0.48,\ 0.6$ correspond to shock thicknesses of 10,12, and 15 particle diameters, respectively. The upstream area fraction is 0.5, restitution coefficient 0.3, and the moonlet diameter is specified to be 25 small particle diameters to match the simulations. The solutions shown have rougly the same qualitative nature although the curves begin to deviate further as θ approaches $\pi/2$. Additionally, the solution corresponding to the smallest δ_o more closely follows the shape of the body. Further decreasing the boundary condition on δ_o results in imaginary components to the solution. One can see from the simulation images that δ_o at this density and restitution coefficient is on the order

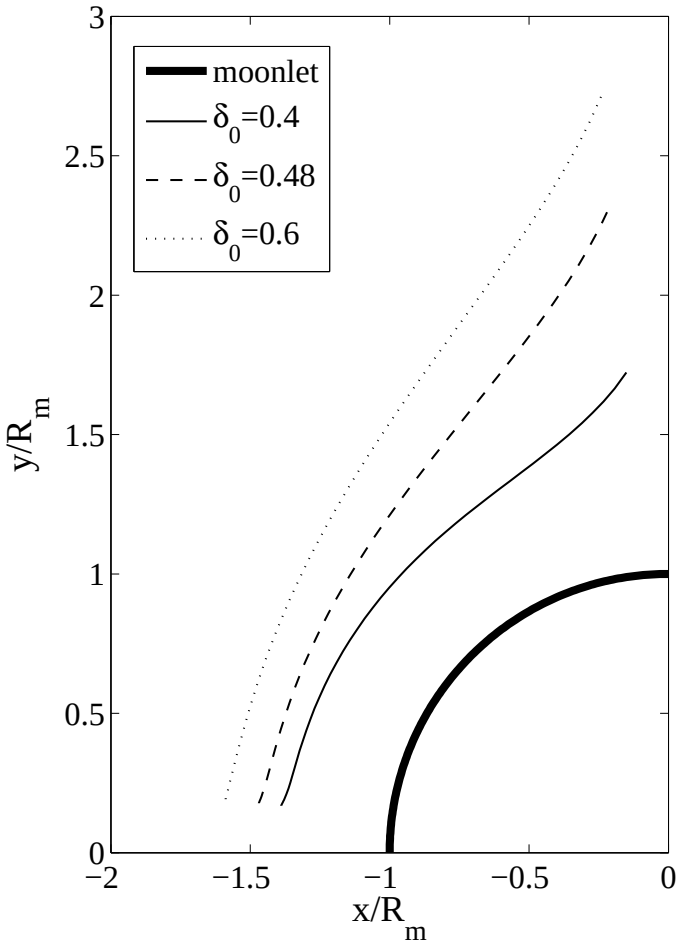

Figure 5.1: Moonlet shock profiles plotted for varied boundary condition δ_o. Incident flow is from the left. Global area fraction is 0.5 and $e = 0.3$

of several particle diameters– not 10 as shown in Figure 5.1. Thus, while the solution of the differential equations appears to capture the basic nature of the bow shock about the circular body, it lacks the ability to obtain solutions given fitting parameters based on the simulation.

In Figures 5.2 and 5.3 we plot the profiles of depth–averaged speed u^* and pressure p^*, respectively. The profiles are plotted against the radial position, expressed in degrees. Although not plotted in the figures, we note that the profile does not apparently change when the value u_o is varied over several orders of magnitude ($u^* = 10^{-3} \rightarrow 10^{-8}$), indicating that solutions are not sensitive to this boundary condition. Similarly the pressure profile does not change appreciably with u_o.

5.4 Conclusions

In this chapter we applied the depth–averaged equations governing shocked flow to the specific case of a moonlet subject to incident Keplerian flow. It was found that solutions produced reasonable qualitative agreement with shock formations shown in discrete element simulations, but the applicability of the model is limited. The failure of the model to produce real numerical solutions for shock thicknesses comparable to simulations suggests that the simplifications employed may not be capturing the relevant physics. This may be related to the assumption of constant post–shock density and the subsequent use of only continuity and momentum relations for the highly dissipative system. In the flow of perfectly elastic flows over wedge geometries the neglect of the energy relation was shown to be reasonable based upon the relative agreement between simulations and the solutions to our system of equations. It may become necessary to remove the assumption of constant density and explicitly include the energy equation, perhaps in a simplified form. Further study should investigate the importance of the energy relation for

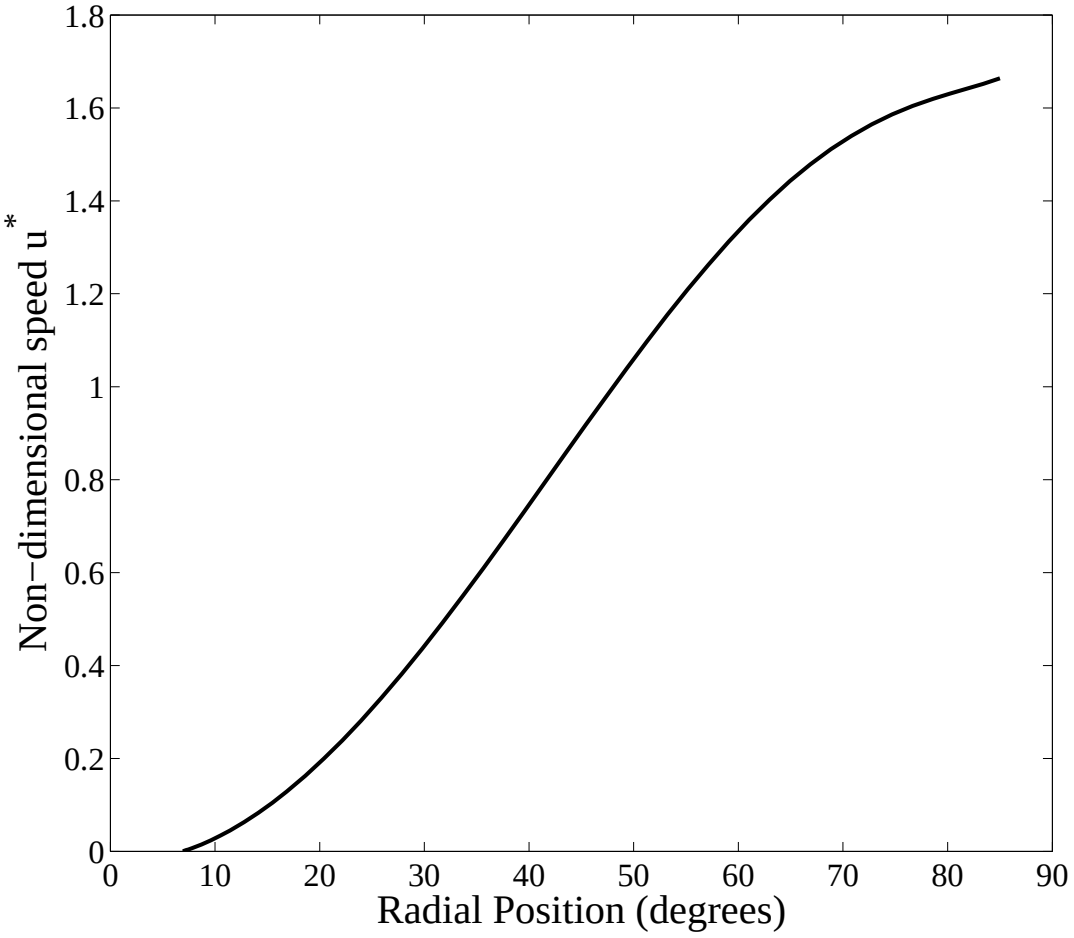

Figure 5.2: Profile of depth–averaged, non–dimensional speed u^*

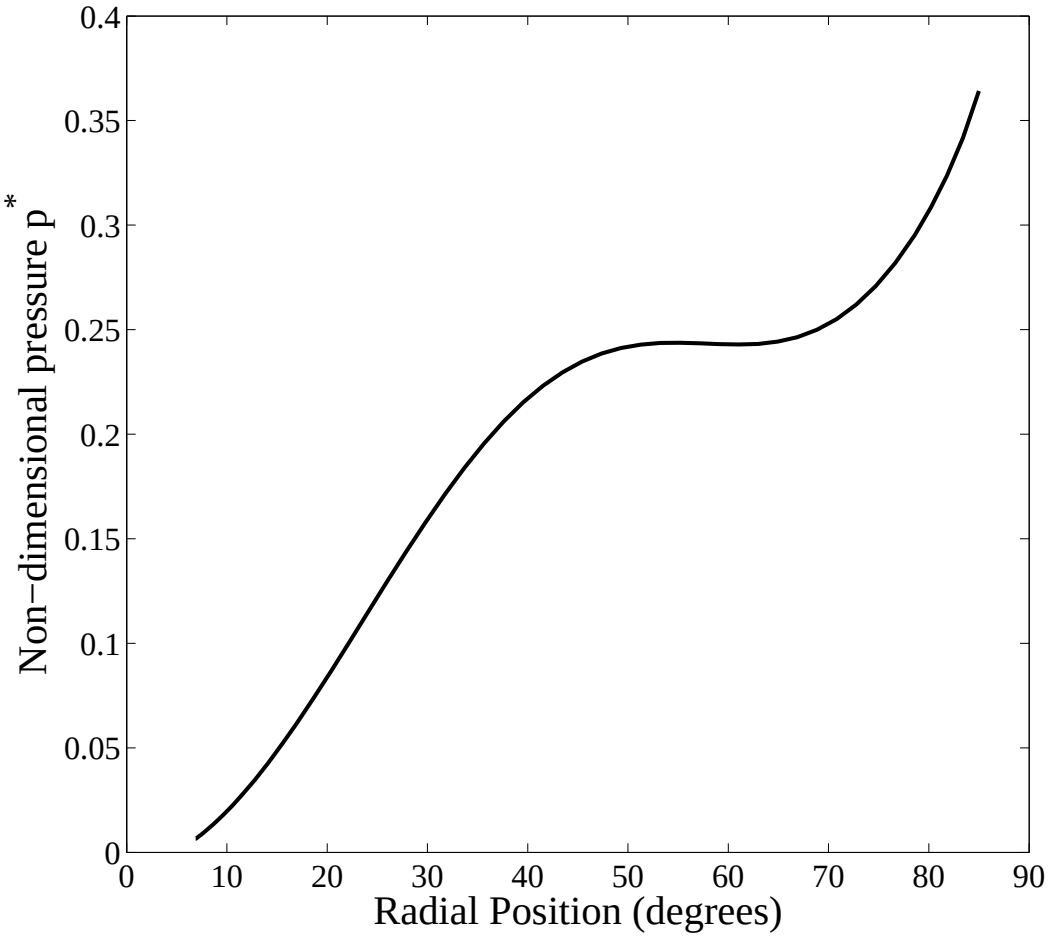

Figure 5.3: Profile of depth–averaged, non–dimensional pressure p^*

inelastic systems. For simplicity it would be of interest to reexamine the canonical wedge geometry subject to uniform flow.

BIBLIOGRAPHY

[1] J.D. Anderson. *Hypersonic and High Temperature Gas Dynamics*. AIAA, 2000.

[2] J.D. Anderson. *Modern Compressible Flow: with Historical Perspective*. McGraw-Hill Professional, 2003.

[3] R.P. Behringer. The dynamics of flowing sand. *Nonlinear Science Today*, 3, 1993.

[4] V. Buchholtz and T. Poschel. Interaction of a granular stream with an obstacle. 1998.

[5] R. Courant and K.O. Friedrichs. *Supersonic Flow and Shock Waves*. Interscience Publishers, Inc., 1948.

[6] J. Duran and A. Reisinger. *Sands, Powders, and Grains: An Introduction to the Physics of Granular Materials*. Springer-Verlag New York, Inc., 1999.

[7] C.H. Edwards and D.E. Penney. *Elementary Differential Equations*. Prentice Hall, 6th edition, 2007.

[8] I. Goldhirsch. Introduction to granular temperature. *Powder Technology*, 182:130–136, 2008.

[9] I. Goldhirsch and G. Zanetti. Clustering instability in dissipative gases. *Phys. Rev. Lett.*, 70, 1993.

[10] J.M.N.T. Gray and X. Cui. Weak, strong and detached oblique shocks in gravity–driven granular free–surface flows. *J. Fluid Mech.*, 579:113–136, 2007.

[11] J.M.N.T. Gray, Y.C. Tai, and S. Noelle. Shock waves, dead zones and particle-free regions in rapid granular free-surface flows. *J. Fluid Mech.*, 491:161–181, 2003.

[12] P.K. Haff. Grain flow as a fluid–mechanical phenomenon. *J. Fluid Mech.*, 134:401–430, 1983.

[13] E. Hascoet, H.J. Herrmann, and V. Loreto. Shock propagation in a granular chain. *Phys. Rev. E.*, 59:3202–3206, 1999.

[14] P. Heil, E.C. Rericha, D.I. Goldman, and H. Swinney. Mach cone in a shallow granular fluid. *Phys. Rev. E.*, 70:060301, 2004.

[15] M.A. Hopkins and M.Y. Louge. Inelastic microstructure in rapid granular flows of smooth disks. *Physics of Fluids A*, 3:47–57, 1991.

[16] H.M. Jaeger and S.R. Nagel. Physics of the granular state. *Science*, 255, 1992.

[17] J.T. Jenkins. Dense shearing flows of inelastic disks. *Phys. Fluids*, 18:103307, 2006.

[18] J.T. Jenkins and M.W. Richman. Kinetic theory for plane flows of a dense gas of identical, rough, inelastic, circular disks. *Phys. Fluids*, 28:3485–3494, 1985.

[19] J.T. Jenkins and M.W. Richman. Plane simple shear of smooth inelastic circular disks: the anisotropy of the second moment in the dilute and dense limits. *J. Fluid Mech.*, 192:313–328, 1988.

[20] A.W. Lees and S.F. Edwards. The computer study of transport processes under extreme conditions. *Journal of Physics C*, 5, 1972.

[21] M.C. Lewis and G.R. Stewart. Features around embedded moonlets in saturn's rings: The role of self–gravity and particle size distributions. *Icarus*, 199:387–412, 2009.

[22] T.S. Majmudar, M. Sperl, S. Luding, and R.P. Behringer. Jamming transition in granular systems. *Phys. Rev. Lett.*, 98, 2007.

[23] O. Mouraille and S. Luding. Sound wave propagation in weakly polydisperse granular materials. *Ultrasonics*, 48, 2008.

[24] F. Reif. *Fundamentals of statistical and thermal physics.* McGraw-Hill, 1965.

[25] E.C. Rericha, C. Bizon, M. Shattuck, and H. Swinney. Shocks in supersonic sand. *Phys. Rev. Lett.*, 88:014302, 2002.

[26] S.B. Savage. Streaming motions in a bed of vibrationally fluidized dry granular material. *J. Fluid Mech.*, 194:457–478, 1988.

[27] L.M. Schwartz, D.L. Johnson, and S. Feng. Vibrational modes in granular materials. *Phys. Rev. Lett.*, 52, 1984.

[28] M. Seiß, F. Spahn, M. Sremčević, and H. Salo. Structures induced by small moonlets in saturn's rings: Implications for the cassini mission. *Geophysical Research Letters*, 32, 2005.

[29] S. Sen and R.S. Sinkovits. Sound propagation in impure granular columns. *Phys. Rev. E.*, 54:6857–6865, 1996.

[30] F. Spahn and M. Sremčević. Density patterns induced by small moonlets in saturn's rings? *Astron. Astrophys.*, 358:368–372, 2000.

[31] M. Sremčević, J. Schmidt, H. Salo, M. Seiß, F. Spahn, and N. Albers. A belt of moonlets in saturn's a ring. *Nature*, 449, 2007.

[32] M. Sremčević, F. Spahn, and W.J. Duschl. Density structures in perturbed thin cold discs. *Mon. Not. R. Astron. Soc.*, 337:1139–1152, 2002.

[33] P.A. Thompson and G.S. Grest. Granular flow: friction and the dilatancy transition. *Phys. Rev. Lett.*, 67, 1991.

[34] M.S. Tiscareno, J.A. Burns, M.M. Hedman, and C.C. Porco. The population of propellers in saturn's a ring. *The Astronomical Journal*, 135:1083–1091, 2008.

[35] S. Ulrich, M. Schroter, and H. Swinney. Influence of friction on granular segregation. *Phys. Rev. E.*, 76, 2007.

[36] L. Verlet and D. Levesque. Integral equations for classical fluids iii. the hard discs system. *Molecular Physics*, 46:969–980, 1982.

[37] C. Wensrich. Dissipation, dispersion, and shocks in granular material. *Powder Technology*, 126:1–12, 2002.

[38] J. Wisdom and S. Tremaine. Local simulations of planetary rings. *The Astronomical Journal*, 995:925–940, 1988.

[39] H.A. Zebker, E.A. Marouf, and G.L. Tyler. Saturn's rings: Particle size distributions for thin layer models. *Icarus*, 64, 1985.